

POLITECNICO DI MILANO

SCUOLA INTERPOLITECNICA DI DOTTORATO

Doctoral Program in Bioengineering

Final Dissertation

Multi-layer microdevices for advanced cell culture applications



Giovanni Stefano Ugolini

Tutor
prof. Monica Soncini
Ing. Marco Rasponi

Co-ordinator of the Research Doctorate Course
prof. Andrea Aliverti

April 4th 2016

Abstract

The latest advancements in microfabrication techniques have led to the development of advanced cell culture platforms aimed at not only reducing the amounts of cells and reagents used but also at an in vitro mimicking of in vivo cellular-scale physico-chemical stimuli and conditions. The present PhD thesis was aimed at designing, developing and employing multi-layer, micron-scale devices for advanced cell culture applications. By employing standard techniques for polydimethylsiloxane (PDMS) microstructuring, microdevices were developed and employed aimed at i) applying finely controlled cyclic strain to human cardiac cells and investigating mechanisms of cardiac fibrosis disease; ii) characterizing an oxygen-control strategy to enable multi-stimulus experiments on cardiac fibroblasts subject to both mechanical strain and oxygen dynamics; iii) modeling the blood-brain barrier, with electric resistance monitoring of an endothelial layer and capability of transport studies. The present PhD thesis achieved both technical and biological novelties. With regards to technological advancements, the microdevices here described present improvements in terms of ease of use, throughput and combination of multiple stimuli. By employing these newly developed microdevices, biological insights were provided describing novel cellular responses under the application of one or multiple physiologically relevant stimuli.

Table of Contents

Chapter 1 – Introduction: standard and microfabricated culture platforms

1.1 In vitro culture platforms: from standard to advanced biological environments.....	7
1.2 Micro-engineering as a tool for developing advanced <i>in vitro</i> culture platforms.....	10
1.3 Organs-on-chips and bio-inspired microfluidics.....	13
1.4 Motivation and aim of the thesis.....	16

Chapter 2 – A micro-platform for studying human cardiac fibroblasts under controlled uniaxial cyclic strain

2.1 Introduction.....	22
2.1.1 Cardiac fibroblasts in the dynamic <i>in vivo</i> environment.....	22
2.1.2 Mechanical stimulation platforms for cardiac cell research	23
2.2 Materials and Methods	25
2.2.1 Preliminary numerical simulations and stretching unit design.....	25
2.2.2 Multi-chamber microdevice design	30
2.2.3 Master molds fabrication.....	30
2.2.4 Microdevice fabrication.....	31
2.2.5 Microdevice characterization.....	32
2.2.6 Cell isolation and culture	33
2.2.7 Immunofluorescence	34
2.2.8 EdU incorporation assay	34
2.2.9 Image acquisition and processing	35
2.2.10 Statistical analysis.....	36
2.3 Results.....	36
2.3.1 Microdevice characterization.....	36
2.3.2 Cell morphology and cell orientation.....	39
2.3.3 Cell-cycle markers expression	41
2.3.4 YAP localization.....	44
2.4 Discussion.....	45
2.5 Conclusions.....	50

Chapter 3 - Combining oxygen control and mechanical strain in a multi-stimulus microplatform for studying cardiac fibroblasts in ischemic conditions

3.1 Introduction.....	54
3.1.1 Myocardial remodeling after ischemic insult: the role of cardiac fibroblasts	54
3.1.2 <i>In vitro</i> platforms and models of cardiac ischemia	55
3.2 Materials and Methods	57
3.2.1 Microdevice outline	57
3.2.2 Microdevice characterization.....	59
3.2.3 Numerical model	59
3.2.4 Stimulation system and parameters	65
3.2.5 Cell culture	68
3.2.6 Immunofluorescence	68
3.2.7 Image processing and analysis.....	69
3.2.8 Statistical analyses	69
3.3 Results.....	70
3.3.1 Numerical simulations	70
3.3.2 Microdevice characterization.....	73
3.3.3 CFs proliferation under combined stimulation	75
3.3.4 Intracellular collagen I production under combined stimulation.....	77
3.4 Discussion.....	79
3.5 Conclusions.....	83

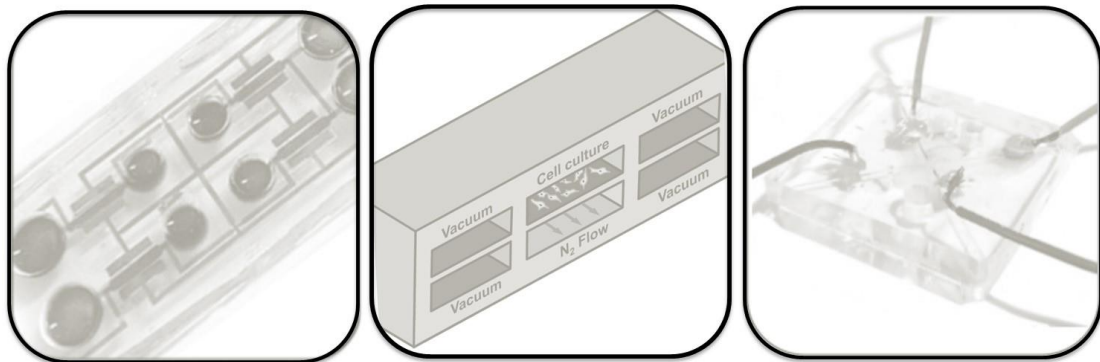
Chapter 4 - A micron-scale model of transport through the blood-brain barrier

4.1 Introduction.....	87
4.1.1 The Blood-Brain Barrier.....	87
4.1.2 Current Central Nervous System diseases and treatments	89
4.1.3 <i>In vitro</i> modeling of the Blood-Brain Barrier.....	90
4.2 Materials and Methods	92
4.2.1 Design requirements.....	92
4.2.2 Microdevice design	93
4.2.3 Master molds fabrication.....	96
4.2.4 PDMS layers fabrication.....	97
4.2.5 Electrodes fabrication	97
4.2.6 Microdevice assembly	98
4.2.7 Cell culture	99
4.2.8 Dextran permeability assay	99
4.2.9 Immunofluorescence	100
4.3 Results and Discussion	100
4.3.1 Microfabrication	100

4.3.2 Permeability assay	101
4.3.3 TEER recordings	102
4.3.4 Immunofluorescence	103
4.4 Conclusions.....	104
General conclusions and achievements of the thesis	106
References.....	110

1.

Introduction: standard and microfabricated culture platforms



1.1 *In vitro* culture platforms: from standard to advanced biological environments

The use of *in vitro* culture systems for cells and tissues is an established technique in the field of biomedical research, biology and biotechnology. In contrast with *in vivo* experiments, where the investigation is conducted inside the living organism, *ex vivo* culturing of cells and tissue enables less invasive experimentation protocols, performed by extracting the biological material and maintaining its living conditions outside of the organism into *in vitro* culture platforms under certain controlled conditions. A great deal of ethical, technical and economic issues, existing when conducting *in vivo* research, are overcome by carrying out experiments *ex vivo* in specific culture systems¹. Indeed, the increasing exploitation of such culturing techniques (commonly referred to as “standard cell or tissue culture”) led to substantial advancements in our knowledge of tissues and organs at several scales: from the elucidation of cells molecular signaling pathways to insights into pathophysiology of entire organ functioning. In addition, resorting to cheaper and less invasive *ex vivo* culture systems has brought to a remarkable increase in experimental throughputs and screening times, ultimately reducing the costs of research and development of drug therapies targeted at relieving or healing patients affected by various pathologies.

With regards to *in vitro* cell cultures, the standard procedures established in the past decades involve the use of bidimensional (2D) flat vessels made of polystyrene (Petri dishes). In such culture systems, cells adhere to the substrate and receive nutrients from the liquid medium poured in the vessels (culture medium). The vessels are typically circular containers of different sizes with a lid that maintains an internal sterile environment while allowing gas transport. To date, these strategies represent the most popular culturing condition, widely used in laboratories around the world to perform research in cell biology and drug development.

Together with the establishment of “polystyrene-based” cell culture as the golden standard in cell research, a parallel research trend has risen in the last decade addressing further improvements of cell culture conditions to a higher degree of similarity with *in vivo* environments. Currently, the notion that differences between standard cell culture conditions and native environments may introduce several experimental biases and limitations is widely accepted. Indeed, while definitely providing a relatively cheap and versatile tool for conducting *ex vivo* cell culture and research, standard culture platforms suffer from unquestionable differences from the native environment in terms of structural, chemical, and physical conditions. Current efforts in the field of bioengineering are therefore focused on the development and evaluation of cell culture platforms aimed at mimicking the main aspects of the native cellular environments of living organisms ². This ambitious task currently represents the scope of many laboratories and researchers worldwide and requires expertise, skills and interactions from multiple fields such as bioengineering, materials science, biology, electronics, chemistry and medicine.

Some of the major environmental factors that contribute to the weak similarity between standard culture platforms and the *in vivo* environment are here listed, together with examples of strategies implemented in advanced culture systems:

- Dimensionality: Cells are physiologically embedded in a three-dimensional protein-based extra-cellular matrix (ECM) whereas standard cell cultures are performed on 2D flat substrates. Hydrogels have been developed and are increasingly employed that allow embedding and culturing of cells in 3D matrixes based on ECM proteins such as collagen or fibrin ^{3,4}.
- Substrate stiffness: Standard polystyrene substrates are typically orders of magnitude stiffer (GPa) than the physiological matrix cells are attached to (kPa-

MPa for most tissues). The use of biocompatible gels has been described as a means of obtaining 2D or even 3D substrates with tunable stiffness^{5,6}.

- Chemical environment: The culture medium volumes supplied to cultured cells are typically unproportioned if compared to the single cells volumes. Indeed, tissues *in vivo* exhibit limited extra-cellular volumes. As a consequence, diffusion-based cell-cell chemical communication is impaired. In general, the composition of culture media typically features basic amino-acids and some known growth factors and is rarely able to model the complexity of chemicals and signaling molecules in the physiological extra-cellular compartments. Oxygen partial pressures also show several differences between tissues and with the standard culture conditions at ambient air (156 mmHg; 21% O₂). These issues have been addressed with several strategies such as: development of micron-scale culture platforms with characteristic dimensions closer to the native environment⁷; use of gradients-generators and multiplexer to increase the throughput of chemicals and growth factors screenings⁸; use of oxygen-controlled incubators where the partial pressure of oxygen is monitored and set at a desired value.

- Physical cues: Most organs and tissues are subject to physical stimulation of various nature and intensity (eg. hydrodynamic shear stress in vessel-lining cells; cyclic mechanical strain and electrical signals in cardiac cells)⁹⁻¹¹. The development of bioengineered platforms typically referred to as “bioreactors” represents the main effort in trying to mimic physical stimuli applied to cell cultures or tissue cultures, often with the ultimate goal of regenerating damaged tissues. Bioreactors for advanced cell and tissue culture have been developed

targeted at different tissues and native environments such as bone, heart and vessels¹²⁻¹⁶

The *in vivo* environment where living cells and tissues reside is therefore an orchestrated, multi-faceted complexity of biological structures and spatio-temporal patterns of physico-chemical cues, intertwined together to control major events such as tissue or organ functioning, growth, remodeling or pathology. This intricate pattern of environmental factors is dramatically different depending on the target tissue or cell type, thus generating the need for advanced *in vitro* culturing platforms and strategies. These engineered solutions must meet tissue-specific requirements and deliver environmental factors in a highly-controlled manner in order to precisely model pathology and physiology of biological systems.

1.2 Micro-engineering as a tool for developing advanced *in vitro* culture platforms

The introduction of soft-lithography technique in the late 1990s represented a major breakthrough in materials science and micro-engineering¹⁷. By enabling controlled structuring of polymeric materials to dimensions of the order of microns, soft-lithography quickly generated a spur of innovation in the field of micron-scale engineering and fabrication. Indeed, a novel branch of engineered devices with possibilities and prospect applications broad enough to impact research fields such as materials science, biology and chemistry, first saw the light during the last decade: the microfluidic devices

Microfluidics has been recently termed as “the science and technology of systems that process or manipulate small (10^{-9} to 10^{-18} litres) amounts of fluids, using channels with dimensions of tens to hundreds of micrometres”¹⁸. Microfluidic devices are the

arrangement of micro-channels employed to control fluid and particle flow and are typically fabricated by using micro-structured molds. Soft-lithography refers to the technique of fabricating these molds: the deposition of precise polymer micro-geometries onto silicon wafers is achieved by spin-coating a precise height of photosensitive pre-polymer on the wafers; geometric features (typically rectangular) are then patterned by selectively photopolymerizing the deposited layer through a photo-mask. These features then serve as molds for replica molding of the final polymer the device are made of: polydimethylsiloxane (PDMS)¹⁹. PDMS is an elastomer particularly appealing for the production of microdevices: due to its glass-transition temperature PDMS is liquid at room temperature and easy to pour on micro-structured molds; upon mild temperature curing PDMS turns into an elastic solid that replicates features with sub-micron resolution. In order to create closed channels, these replicas are typically bonded on glass slides (single layer device) or to other layers of structured PDMS to create complex arrangements of channels (multi-layer devices). Furthermore, PDMS has interesting properties for biological applications: it is chemically inert and highly biocompatible, making it a suitable substrate for cell culturing; due to its high gas permeability it allows gas transport, enabling rapid equilibration of the micro-structured channels atmosphere with the incubation atmosphere; it is optically transparent (range of wavelength: 240nm to 1100nm) making it a perfect candidate for imaging of cells and biological samples inside the channels²⁰.

The ability to easily microstructure channels with such a precision and low expense quickly generated novel inspiring engineered solutions: pneumatic microfluidic valves were obtained by overlapping two channels, thus paving the way to a higher control on fluid flow in microdevices²¹; defined arrangements of channels based on resistive flow allowed fluid mixing and generation of controlled gradients of

diluted species, dramatically improving assay times and throughput of analyses⁸; mixing PDMS with functional doping materials enabled the integration of electrical or magnetic components into microdevices, thus further broadening the possibilities and technological applications of microfluidics^{22,23}.

This brand-new competences readily found use in the control of chemical reactions, biochemical analyses or molecular diagnostics. Major advantages are present when employing miniaturized devices: the use of small volumes reduces the amounts of reagents and chemicals to use while maintaining high sensitivity and resolution in detection or reaction analyses; in some cases reaction times are also dramatically reduced due to smaller volumes or higher surface-to-volume ratios; small sizes increase the chances of parallelization and set up of multiple replicates at a time. All these factors contribute to a reduction of costs and time together with an increase in throughput of experimental research¹⁸.

The present PhD thesis is focused on the use of microfabrication technology to develop and employ microdevices for advanced cell culture applications. Indeed, the fields of cell and molecular biology were also highly impacted by the rise of microfabrication. What has been described in the previous paragraph as an enormous technical gap between standard *in vitro* cell culture systems and the *in vivo* environments appeared to have found a helping hand in the new-found abilities of microfluidic technologies. The abilities of scaling down culture systems to characteristic dimensions of the same order as the ones of cells not only reduced the total amounts of reagents and cells required for assays, but also allowed the manipulation of single cells, hundreds of cells or entire cultures (more than a thousand cells) with greater control. Novel technical solutions allowed the application of physico-chemical stimuli in these micro-environments (flow-induced shear stress,

deformable substrates, injection of hydrogels for 3D cell cultures, etc.). The rise of microfluidics therefore established as one of the candidate technologies that may boost the current value and significance of standard cell cultures and lift up *in vitro* models to a newer level that sits in-between current models and *in vivo* experimentation.

1.3 Organs-on-chips and bio-inspired microfluidics

Organs-on-chips represent a recent research trend that involves the development of microfluidic devices able to host cell cultures in a controlled environment that features physiologically relevant stimuli, functions or structures in order to model *in vivo* cellular environments. Despite the reference to entire organs, organs-on-chip are rather focused on recreating minimal functional elements of specific tissues by tuning the arrangement of cells and the external factors they are subject to ²⁴.

Single-layer devices are made of a single PDMS layer of microstructured channels bonded on a glass coverslip or another flat PDMS layer. Despite the simple manufacturing protocol, this sub-type of devices produced a number of relevant physiological models: an artificial liver sinusoid was developed for drug hepatotoxicity studies ²⁵; low-attachment chambers were employed to generate on-chip 3D aggregates of chondrogenic cells subject to a gradient of chemical factors to investigate cartilage formation mechanisms ²⁶; a system for injecting 3D hydrogels into a channel confined by spaced posts enabled the formation of 3D capillary microvascular networks with the option of perfusing capillaries with cancer cells to study cancer metastasis in different tissues ²⁷; axonal growth was induced in microfluidic devices to model neuronal injury and regeneration ²⁸.

Multi-layer devices however retain greater possibilities in terms of recreating complex structures and stimuli. Indeed, the majority of organs-on-chips exploits

arrangements of multiple microstructured layers. In particular, technical solutions that can be achieved only by stacking different layers of microstructured PDMS involve:

- Possibility of modeling cellular transport: the inclusion of porous membranes within two fluidic layers allows the culturing of cells on top of the membrane and the collection of molecules transported through cells and membrane pores in the lower layer. Cellular transport is a key biological mechanism underlying important tissue structures such as the blood-brain barrier or the intestinal villi.
- Mechanical stimulation: thin deformable membranes, included into microdevices have the potential of serving as actuators or substrates for mechanical stretch application.
- Pneumatic control layers: controlling fluid flow in a microchannel by means of micro-valves require the addition of a control layer (either above or below the flow channel) that pneumatically blocks or allows fluid flow.

High-impact biological models were built basing on multi-layer microdevices. A pivotal study was published in *Science* (2010) describing a multi-layer microdevice (lung-on-a-chip) recapitulating the alveolar interface: a porous membrane is seeded with one cell type on each side (lung epithelium and endothelium) and two side chambers provide a breathing mechanisms based on mechanical strain of the membrane²⁹. This model provided novel insights into mechanisms and interplays that regulate physiology and pathology of the alveolar interface. A similar concept was employed to model intestinal transport mechanisms (gut-on-a-chip)³⁰. The use of porous membranes included in microdevices found numerous applications in modeling the blood-brain barrier with the aim of finding drug carriers formulations able to cross the barrier and reach the brain³¹. In this case, the porous membrane is seeded with a tight monolayer of endothelial cells that hinders transport from a top to a lower layer.

Studying the transport of drug and carriers candidates in such microdevices results particularly appealing because of the small volume of costly drug and carrier molecules required.

The prospect of generating or studying cardiac tissue in specifically tailored heart-on-chips has also been addressed. Arrays of thin PDMS films were fabricated and seeded with cardiac myocytes in a specific microplatforms³². When one side of the film is free to deform, paced or spontaneous contraction of the cardiac myocytes induce a force-dependent displacement of the films, useful for drug screening and contraction studies. A multi-layer and multi-stimulus microplatform was developed to reproduce the cardiac environment by applying cyclic strain to mesenchymal stem cells cultured on a deformable thin membrane and simultaneously applying cyclic electric fields from two lateral embedded and deformable electrodes³³. A beating 3D heart-on-a-chip was developed by combining on-chip 3D cell-laden hydrogel injections with 3D mechanical stimulation and the importance of mechanical stimulation in the outcome of cardiac micro-tissues maturation was then elucidated³⁴.

In summary, a thriving research trend has initiated when easy, reliable and relatively cheap techniques for micro-structuring channels in a biocompatible polymer were made available. Microfabrication and microfluidic devices have proved able of not only providing *in vitro* models and platform but, most importantly, to generate a thrust towards models that are increasingly similar to the *in vivo* condition. With a proof of concept obtained in the past decade after the development of complex organs-on-chips that enabled progress and advancements in the respective fields of biological research, microfluidic devices currently seem to be halfway through their road to success: indeed, the ultimate goal of organs-on-chips would be to provide a robust, commercial and widely approved step in-between standard culture systems and *in vivo*

experimentation not only in basic research but also in the expensive processes of drug screening and validation.

1.4 Motivation and aim of the thesis

Current research trends in microfluidics depict a promising scenario for the application of microdevices in cell culture and cell biology. Indeed, the ability of tailoring the culturing system and the stimuli applied to the specific biological context, while constantly maintaining culture biocompatibility and small sizes is an appealing solution for bioengineers and biologists. The wide range of biological open questions leaves a broad variety of aspects still in need of testing and modeling by means of microfabricated devices. At the same time, improvements in terms of ease of fabrication, ease of use by non-specialized operators, reliability and throughput are required in order to provide microfluidic devices with the robustness and consistency needed to become a widespread and accepted technology.

With heart disease being the leading cause of morbidity and mortality in western countries, cardiac cell research is a major trend of investigation worldwide. *In vivo* and *in vitro* experimentations are carried out to increase basic knowledge of heart functioning at multiple scales, to understand pathological conditions and to tailor specific therapies and regenerative strategies. To this aim, developing and employing technical solutions to recreate cardiac environments in *in vitro* platforms is an essential task of bioengineering. Similarly, pathologies related to the Central Nervous System represent a challenging clinical issue due to the lack of therapeutic strategies. With the blood-brain barrier representing the main obstacle to the development of effective treatments for brain disorders, the need for *in vitro* culture platforms that assist the process of drug development and optimization is increasing.

The present thesis is aimed at developing and employing microdevices specifically tailored to physiologically relevant advanced cell culture applications. The microdevices are conceived as multi-layer devices, in order to better approach and mimic the specific biological contexts. The thesis is organized into chapter each describing a specific technical and biological work aimed at modeling a different biological environment. Each work comprises a development phase where the design and microfabrication steps required to produce the devices are described; a characterization phase where the device structure or the stimuli applied are experimentally characterized; an application phase where the platform is actually tested with specific cell types and used to investigate biological open aspects.

Chapter 2 describes the design and development of a microplatform for mechanical stretch of cardiac cells. Building on an existing technical solution, a novel design with improvements in terms of throughput and ease of use is described. With a novel platform that poses lesser operational complexities, a biological context is fully explored and characterized in-depth. The response of cardiac fibroblasts to different strain intensities is investigated and novel results demonstrate the existence of a cellular control of proliferation acting according to the intensity of the strain applied. The newly developed microdevice enabled the description of this mechanism, not addressable otherwise, and demonstrated the relevance of employing advanced culture platforms.

Chapter 3 describes the development of a multi-stimulus platform that applies both mechanical strain and dynamic oxygen concentrations to cultured cells. Making use of the platform described in Chapter 2, a characterization of a microchannel-based system for culture chamber oxygen conditioning is presented. An innovative multi-stimulus configuration of the microdevice represents a versatile tool to mimic both physiology and pathology of cardiac environments, with particular specificity to

ischemia and oxygen-deprivation of the heart. This infarct-on-a-chip device is then used to investigate the activation of cardiac fibroblasts when subject to different combinations of mechanical strain and oxygen dynamics. This improvement enabled multi-stimulus experiments, an approach of investigation still missing from current literature, and provided a novel perspective on studying cardiac fibroblasts activation upon physical and chemical stimulation.

Chapter 4 describes the development of a microdevice for blood-brain barrier transport studies. The implementation of an electric-resistance based monitoring system to estimate barrier formation is described together with the inclusion of a porous membrane for transport studies. The microdevice is then preliminarily validated with brain endothelial cells to describe the formation of an on-chip endothelial barrier and its potential prospect applications.

The scientific outcome of the present thesis therefore mainly involves an innovative approach for a microdevice-based modeling of the cardiac environment in physiology and pathology together with biological insights gained thanks to this approach and regarding proliferative, ECM-remodeling and mechano-transductory aspects of cardiac fibroblasts in health and disease. In addition, a similar multi-layer microdevice-based approach is translated into a completely different field: the requirements of blood-brain barrier models are integrated into a preliminarily validated, multi-layer microdevice.

2.

A microplatform for studying human cardiac fibroblasts under controlled uniaxial cyclic mechanical strain

The technical work described in this chapter was partially carried out at *Mechanobiology Laboratory*, Massachusetts Institute of Technology, Cambridge (USA) and at *Biosystems and Micromechanics IRG (BioSyM)*, Singapore-MIT Alliance for Research and Technology, Singapore (SINGAPORE) for silicon masters fabrication and preliminary device development.

Biological experiments and image acquisition were carried out at *Unità di Ingegneria Tissutale Cardiovascolare*, Centro Cardiologico Monzino, Milan (ITALY).

This chapter partially refers to:

Ugolini GS, Rasponi M, Pavesi A, Santoro R, Kamm R, Fiore GB, Pesce M, Soncini M. 2015. On-chip assessment of human primary cardiac fibroblasts proliferative responses to uniaxial cyclic mechanical strain. *Biotechnol. Bioeng.* <http://dx.doi.org/10.1002/bit.25847>.



Rationale

The following chapter describes the design, development, characterization and extensive employment of a novel multi-layer microdevice for application of mechanical strain to cell monolayers. Despite being a fundamental environmental stimulus in the in vivo cardiac tissue, a limited number of microplatforms devoted at examining cardiac cell cultures under cyclic mechanical strain is reported in literature. Inspired to a previously described device layout, the platform here presented shows technical modifications for increasing ease of use by end-users and experimental throughput. With respect to standard cell stretching devices, the described microplatforms allows for precise control of the strain field applied, allowing biological investigations under slightly different mechanical strain intensities.

The microdevice was then extensively used to characterize the effect of cyclic mechanical strain on human primary cardiac fibroblasts. Cardiac fibroblasts are major regulators of cardiac homeostasis in health and disease and represent a particularly dynamic cell type: upon certain physical or chemical tissue conditions (mechanical overload or ischemia) cardiac fibroblasts trans-differentiate from a quiescent state to an active and proliferative state, capable of invading, remodeling and healing tissue damage.

The investigation of cardiac fibroblasts responses to relevant stimuli such as cyclic strain is therefore of great interest to the biological and clinical audience and the absence of controlled platform to apply well-defined and uniform strain fields to cell cultures creates a gap that has been effectively targeted by the technical and biological work described in this chapter. With the newly developed microplatform, it was possible to seed human cardiac fibroblasts freshly isolated from cardiac biopsies and analyze their response under finely controlled uniaxial strain intensities. The results obtained

in this study were recently published in the international journal Biotechnology and Bioengineering and include the finding that human cardiac fibroblasts critically regulate their proliferation according to the intensity of mechanical strain sensed during the culture.

2.1 Introduction

2.1.1 Cardiac fibroblasts in the dynamic *in vivo* environment

Owing to cardiac contractility, the myocardium represents a highly dynamic mechanical microenvironment for cardiac cells. During each heartbeat, cardiac myofibers relax and contract synergistically to generate blood flow through the vascular system. At the sub-millimeter scale, this contraction produces a spatiotemporal pattern of stress and strain affecting all cardiac cellular and non-cellular elements. The balance between external loads and internal cell biomechanics is a determinant of cell and tissue homeostasis. Specific cardiac cell functions are either activated or repressed, depending on the magnitude of mechanical load sensed by the intracellular signal transduction machinery, with consequences for physiological or pathological tissue evolution^{35–39}.

The most abundant cell type by number in the human heart is the cardiac fibroblast, accounting for more than half of the total number of cardiac cells and responsible for a variety of functions: synthesizing cardiac ECM components, participating in cardiac pacing and secreting cytokines necessary for cardiac homeostasis^{40–42}. Cardiac fibroblasts (CFs) are the main actors in cardiac tissue remodeling: upon pathological tissue conditions such as ischemia^{43,44} or mechanical overload⁴⁵, CFs altered behavior leads to unbalanced synthesis and degradation of ECM resulting in myocardial stiffening, fibrosis and reduced contractility^{46,47}. The hallmark of this pathological CFs behavior is the differentiation of resident CFs into myofibroblasts, a contractile and matrix-producing cell type that expresses smooth muscle cells markers. This phenotypic switch has been well characterized by *in vitro* studies and has been linked to mechanical cues^{48,49}, suggesting the mechanical microenvironment as a factor in the onset or progression of fibrotic cardiac disease. However, CFs proliferation dynamics seem also to play a role in the evolution of

cardiac fibrosis, as demonstrated by *in vivo* studies that report an increased number of resident CFs in pathological myocardial conditions ^{50,51}. Whether this increased proliferation precedes or follows the CF phenotypic switch is not clear and, in general, this proliferative response is not well-characterized by *in vitro* studies at the cellular level nor it has been clearly correlated to mechanical stimuli.

Indeed, *in vitro* studies have directly correlated mechanical load with increased production of ECM proteins by human ^{52,53} and rat ⁵⁴⁻⁶¹ CFs with strain-dependent effects ⁵⁴. However, a direct relationship between mechanical load and CFs proliferation control remains elusive and described only by a limited number of studies on rat CFs reporting both decreased ⁶¹⁻⁶³ and increased ⁶⁴ proliferation.

2.1.2 Mechanical stimulation platforms for cardiac cell research

The nature of the mechanical stimulus experienced by cardiac cells *in vivo* is extremely complex: the strain field is three-dimensional, multi-directional and highly variable throughout the organ ^{65,66}. *In vitro*, this complexity is often modeled and simplified by systems that allow for cell cultures on cyclically strained 2D substrates. In order to precisely identify characteristic behaviors of cardiac cells subject to cyclic strain, the ability to apply finely controllable, highly uniform strain fields *in vitro* is of paramount importance. Custom-made or commercially available systems for cell culture under cyclic strain are based on pneumatic or motorized actuation. Using pneumatic actuation, a deformable membrane included in a well is usually stretched multi-axially by application of vacuum in an adjacent chamber ^{67,68}. With particular respect to the commercial platform FlexCell (FlexCell International Corp., Hillsborough, NC) it has been demonstrated that it suffers from limitations in terms of strain field non-uniformities, calibration issues, operational complexities and low-

throughput^{69,70}. Motor-driven stretching platforms typically apply uniaxial strain fields to suspended deformable membranes attached to a linear moving motor. When the membrane sides are free to deform the resulting strain field has a longitudinal component, along the direction of motion of the motor, but also a transverse, non-negligible, component⁷¹⁻⁷⁴. In summary, available culture platforms often apply different strain fields to 2D cell cultures in terms of directionality (biaxial, uniaxial, equi-biaxial) and the level of control on the strain field uniformity is often insufficient to conduct systematic and comparable biological studies. In order to address this issue, a sound experimental criterion to systematically explore cell behaviors under mechanical strain is to improve the control and uniformity of the stimulus applied.

In this work, we investigated the response of human adult heart-derived CFs to different cyclic strain intensities by employing a custom designed microdevice. Typical advantages of microfluidic devices include the requirement of small amounts of cells and reagents. However, the small amounts of biological materials cultured are often not compatible with some biological assays such as gene (qPCR) or protein (Western Blot) expression analyses. Micro-scale stretching systems include pressure or piezo-electrically strained thin membranes⁷⁵⁻⁷⁷ and systems where a thin membrane is deformed by application of vacuum into side chambers^{29,78-80}. Building on a previous concept²⁹, we developed a multi-chamber cell straining microdevice that allows for cell culture under finely controlled uniaxial and uniform mechanical strain. We adopted engineering tools during device development to design and characterize the strain field and we included the possibility of conducting four parallel and independent cell cultures in the same microdevice to increase throughput. The ability of applying finely controlled strain fields in a high-throughput fashion and the small amounts of cells required enabled us to perform controlled cyclic strain experiments on freshly isolated

human primary CFs subject to different strain intensities. We subjected cells to strain intensities representative of physiological myocardial contraction (8% strain) and reduced myocardial contraction (2% strain) and we investigated human CFs responses in terms of cell morphology, proliferation rate and mechano-transduction. We identified a time- and a strain-dependent relationship between cell straining and control of CF mitosis and proliferation. We reported the possible involvement of a mechano-sensing-associated transcription factor (YAP) in the control and modulation of the proliferative responses we observed. The YAP transcription factor is one of the master components of the Hippo pathway, involved in heart development and growth^{81,82}, in reactivation of cardiac myocytes proliferation⁸³, in myocardial damage sensing by cardiac progenitors⁸⁴, and recently implicated in mechano-sensing and geometry-associated mitotic checkpoints^{85,86}.

2.2 Materials and Methods

2.2.1 Preliminary numerical simulations and stretching unit design

The microdevice is fabricated in polydimethylsiloxane (PDMS, Sylgard 184, Dow Corning) and consists of four separate stretching units each featuring a thin deformable PDMS membrane sandwiched between two PDMS layers (Figure 2.1A). Each of the top and bottom layers contains two flanking actuation chambers (Fig. 2.1A, red) that, upon application of controlled negative pressure, uniformly stretch the central thin membrane. The chamber located above the thin membrane contains the cell culture (Fig 2.1A, blue) whereas the fluid chamber below the membrane allows for environmental conditioning of the upper culture chamber through gas or small-molecules exchange (Fig. 2.1A, green).

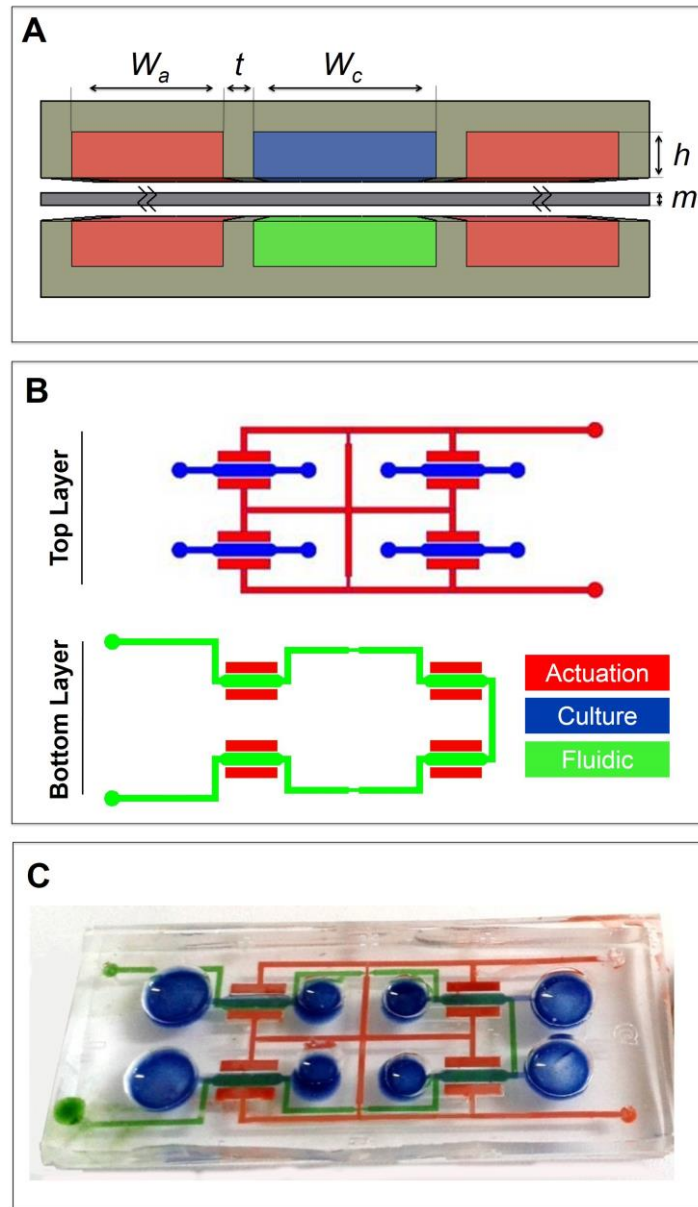


Figure 2.1 – A) Annotated cross section of a stretching unit: geometric parameters are highlighted (W_a : side chamber width, W_c : culture chamber width, h : culture chamber height, m : membrane thickness, t : wall thickness). Cell culture chamber is represented in blue, side actuation chambers are represented in red and lower fluidic circuit is represented in green. B) Top view of microdevice layers layout: top layer features culture chambers (blue), actuation circuit and chambers (red), bottom layer features common lower fluidic circuit (green) and lower halves of the side actuation chambers (red). C) A fabricated microdevice filled with colored dyes. Same color code as Panels A and B.

The design of the microdevice stretching unit was performed by pursuing two main design specifics: generate uniform membrane strain of around 8% and provide a cell culture region of more than 5mm^2 . The geometric parameters involved into this design procedure were: membrane thickness (m), wall thickness (t), width of the culture

(Wc) and actuation (Wa) chambers, length of the chambers (Lc) and chamber height (h). Width (Wc) and length (Lc) of the culture chambers were set respectively to 1.2mm and 5mm. The chamber height (h) was set to 300 μ m. A membrane thickness of 80 μ m was chosen to avoid membrane sagging and non-uniformities in membrane planarity. Width of the actuation chambers (Wa) was set to 1mm to allow for complete wall displacement. Given this geometry, the effect of wall thickness on membrane strain was evaluated by numerical simulation of the 2D cross-sectional geometry of the stretching unit. Three 2D models of the cross-section of the device were designed with the Solid Mechanics module of *Comsol Multiphysics 4.3* (Comsol, Inc., Burlington, MA). Each model comprised the culture chamber, the lower fluidic chamber and the side actuation chambers and featured a different wall thickness (namely $t_1=100\mu\text{m}$, $t_2=200\mu\text{m}$, $t_3=300\mu\text{m}$). The model geometries were discretized with a mesh scheme consisting of triangular elements. A mesh sensitivity analysis was performed to determine the optimal number of elements and element size. To this aim, the displacement of two representative points on the culture membrane upon constant negative pressure applied to the side actuation chambers (-600mmHg) was evaluated for increasingly fine mesh schemes. This parameter was found to reach an asymptotic value for a mesh scheme consisting of about 31000 elements featuring a maximum characteristic size of 15 μ m. These mesh properties were employed for all three models. The material properties of Sylgard 184 PDMS were assigned to the models (specifically Young's modulus = 1.5MPa and Poisson's module = 0.499). Encastre boundary conditions were applied to the outer faces of the device cross-section. A uniform load resulting from a negative pressure of -600 mmHg was applied to both side chambers and a stationary study was solved.

Figure 2.2 shows the resulting deformed configuration and strain field intensity throughout the cross-sections in all three geometries. In all cases, the membrane strain resulted uniform along its width, while the strain intensity was inversely proportional to the wall thickness. Although the wall thickness of $t_1=100\mu\text{m}$ yielded maximum membrane strain (around 14%), actual fabricated devices showed occasional leakage of culture medium from culture chambers to side actuation chambers upon application of negative pressure. We believed that leakage could be mainly due to the small surface available for the adhesion, and this geometry was therefore discarded. The geometry with wall thickness $t_2=200\mu\text{m}$ was then chosen as final geometry because of functional robustness and maximum strain field of 8%. Final geometry parameters are shown in Table 2.1.

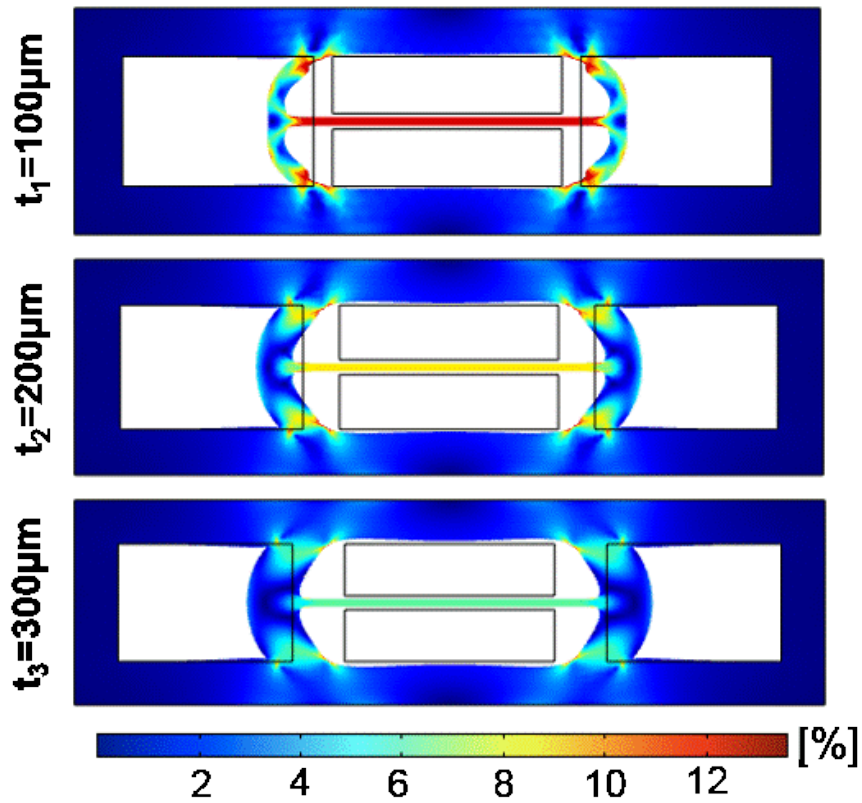


Figure 2.2 – Resulting deformed configurations and strain field intensities throughout three different cross-sectional geometries. Wall thickness of $t_1=100\mu\text{m}$ results in membrane strain field of around 14%, wall thickness of $t_2=200\mu\text{m}$ results in strain field of around 8% whereas wall thickness of $t_3=300\mu\text{m}$ results in a strain field of around 6%

Microdevice geometric parameters

<i>Geometric parameter</i>	<i>Value (μm)</i>
<i>Chamber height (h)</i>	300
<i>Culture chamber width (W_c)</i>	1200
<i>Chamber length (L_c)</i>	5000
<i>Side actuation chamber width (W_a)</i>	1000
<i>Wall thickness (t)</i>	200
<i>Membrane thickness (m)</i>	80

Table 2.1 - Details of microdevice geometry. The parameters are outlined in Figure 1 (main paper) and have been optimized to obtain a uniform strain of 8% on a culture membrane larger than 5mm^2 .

2.2.2 Multi-chamber microdevice design

Four stretching units were incorporated into a single device, each actuated by a common pneumatic circuit and featuring a single, common lower fluidic circuit. The culture chambers, however, are completely independent and each is accessible from two wells. As shown in Figure 2.1B, the device is comprised of a top layer that includes culture chambers (blue), upper halves of the side actuation chambers (red), and pneumatic actuation circuit (red) and a bottom layer that includes a lower fluidic circuit connecting the fluidic chambers (green) and the lower halves of the side actuation chambers (red). These layouts were drawn through CAD software (AutoCAD, AutoDeskInc). Transparency masks were printed at high-resolution (32,000 dpi) and used as photomasks in the subsequent photolithography steps.

2.2.3 Master molds fabrication

Devices were realized through PDMS replica molding using microstructured silicon wafers as molds. Wafer preparation utilized deep reactive-ion etching (DRIE) technique to obtain structures featuring highly vertical-walled trenches and high aspect ratios. Briefly, 10” silicon wafers were first cleaned in a wet bench with piranha solution (3:1 v/v sulfuric acid and hydrogen peroxide) at 120°C, rinsed with DI water and dried with nitrogen gas. To enhance adhesion, hexamethyldisilazane (HMDS) was spin-coated on wafers and allowed to dry at 100°C. Positive photoresist (AZ9260) was then spin-coated on the wafers at 1200 rpm for 30s to reach a target thickness of 22µm and baked on a hotplate at 114°C for 240s. Layouts were transferred to the coated wafers by filtering UV light exposure (energy: 2,100 mJ/cm², hard contact mode: gap 25µm) through corresponding photomasks. The physical masks were finally obtained by developing the wafers in AZ4100k and DI water solution (1:2, v/v) for about 90s,

rinsing with DI water and drying with nitrogen gas. The unmasked silicon surface was finally etched at a rate of 1 $\mu\text{m}/\text{min}$. The positive tone photoresist was removed from the wafers through lift-off, prior to subsequent use as master molds.

2.2.4 Microdevice fabrication

All components of the microdevice were fabricated in PDMS, used at a 10:1 (w/w) pre-polymer to curing agent ratio. In particular, both layers were obtained by casting PDMS directly on the corresponding molds. The thin membrane was fabricated by spin-coating liquid PDMS at 900rpm for 30s on a clean silicon wafer, resulting in a thickness of 80 μm . Before assembling membrane and upper layer, through-holes were punched in the upper layer to create wells for the culture chambers (5mm and 6mm diameters), and inlets for the pneumatic actuation circuit (1mm diameter) and for the lower fluidic circuit (1mm diameter). Upper layer and membrane were plasma bonded (Plasma Cleaner, Harrick Plasma, 60s, 10W) and then cut and lifted off the silicon wafer. At this stage, small holes were made on the thin membrane matching the side actuation chambers by using sharp fine-tip tweezers. This step resulted critical for successfully delivering negative pressure actuation to both upper halves and lower halves of the side actuation chambers. Finally, the upper layer and membrane complex was bonded to the lower layer after plasma activation and careful alignment under a stereomicroscope. The microdevices were finally sterilized by autoclaving (121 $^{\circ}\text{C}$, 20min, wet cycle), dried at 80 $^{\circ}\text{C}$ overnight and stored until use. An image of a fabricated microdevice is shown in Figure 2.1C, with red channels representing the pneumatic actuation circuit and chambers, blue channels representing culture chambers and green channel representing lower fluidic circuit and chambers.

2.2.5 Microdevice characterization

The membrane strain field was characterized by mixing graphite powder (diameter smaller than 20 μ m, Sigma, Italy) with liquid PDMS (1:1000, w/w) before membrane fabrication. The graphite particles allowed the strain field to be quantified at different negative pressures applied in the side chambers. In total, a number of 10 culture chambers from a pool of 5 devices were analyzed: images were taken at 1X magnification with a stereomicroscope. For each chamber, 7 images were taken at pressure values ranging from 0mmHg to -600mmHg with a step of 100mmHg. ImageJ software (v. 1.47f-software for Java, National Institutes of Health, USA) was employed to measure displacements (minimum 5 measures per image) and estimate average strain. These data were used to draw strain-pressure relations. In addition, a Digital Image Correlation algorithm (Improved Digital Image Correlation, MATLAB) was employed to estimate full-field displacements and strains on the membranes. This calculation was carried out for 3 microdevices at an applied pressure of -500mmHg and yielded 2D strain field maps for each considered culture membrane. In order to evaluate strain field uniformity and uniaxiality, ϵ_{yy} and ϵ_{xx} strain components were computed, where x is the channel main axis. Local strain values were extracted from 2D strain field maps to quantify regional strain variations. To this purpose, nine regions were analyzed along the length (main axis) of the culture channel and from each region three sub-regions were considered along the width of the channel: central membrane region and top and bottom regions, closer to the channel walls. This allowed the evaluation of possible strain field variations throughout the entire culture membrane and the definition of the region where the strain field is highly uniform and uniaxial.

2.2.6 Cell isolation and culture

Samples from patient atria were obtained under informed consent. Human cardiac fibroblasts were isolated and expanded according to previously described protocols⁸⁷⁻⁹⁰. The atrial fragments were cut into about 1 mm³ pieces and incubated four times for 30min at 37°C with 3mg/ml collagenase NB4 (Serva, Germany). After digestion, the solution was filtered using 70µm mesh nylon filters and the resulting cells solution was plated onto uncoated Petri dishes. Culture medium was Ham's F12 medium (Lonza, Milan, Italy) containing 10% FBS (Hyclone, USA), 2mM L-Glutathione (Sigma, Italy), 0.05% Human Erythropoietin (Sigma, Italy), 10ng/ml bFGF (Peprotech, UK) and antibiotics. Cell cultures were incubated at 37°C and 5% CO₂ at all stages. Cells were amplified and then seeded for mechanical strain experiments at a passage number of 3.

Before cell seeding, devices were plasma treated and coated with human fibronectin (25µg/ml, 30min incubation; Sigma Aldrich, USA). A cell suspension of 100µl was manually injected into each culture chamber and allowed to adhere to the membrane for 16h into an environmental incubator (37°C, 5% CO₂). The cell concentration value was set to 10⁶ cells/ml following preliminary cell adhesion experiments. Subsequently, controlled cyclic strain (either 2% or 8%) was applied to the culture chambers at 1Hz for 24h or 72h. Negative pressure was delivered through a standard laboratory vacuum line, controlled by a high-precision pressure regulator and actuated through an electronically controlled electro-pneumatic valve. Culture medium was changed every 12h. No environmental conditioning was applied in this study and lower fluidic channels were therefore left open to the incubator atmosphere. For each condition tested, static microdevices (without application of cyclic strain) were also cultured as control. For proliferation and mechano-transduction studies, the minimum

number of biological replicates was 4, whereas for morphological studies we performed analyses for a minimum of 6 biological replicates.

2.2.7 Immunofluorescence

Cells were fixed with 4% paraformaldehyde in PBS for 10 minutes. After blocking and permeabilizing for 1h at room temperature with PBS containing 3% bovine serum albumin and 0.1% Triton-X, cells were incubated for 2h at room temperature with the following primary antibodies: anti-Ki67 (rabbit, AbCam, UK), for proliferating cells (cell cycle phases: G1 through M); anti-phospho-Histone-H3 (Ser10, rabbit, Santa-Cruz, US), for mitotic cells; anti-YAP (rabbit, Santa-Cruz, US), to identify nuclear or cytoplasmic localization of the YAP/TAZ protein complex. Cells were then probed for 1h at room temperature with Alexa Fluor 488-conjugated secondary antibodies (Invitrogen). Nuclear staining was performed by incubating cells with DAPI whereas actin staining was performed with rhodamine-conjugated Phalloidin. Negative controls were present for all immunofluorescence stainings.

2.2.8 EdU incorporation assay

Cells undergoing active DNA synthesis during S-phase were evaluated with Click-It EdU Alexa Fluor 488 Imaging Kit (Invitrogen). The cell culture medium was switched to medium including 10 μ M EdU. After 2h incubation at 37°C, cells were fixed with 4% paraformaldehyde and probed with the Alexa Fluor 488 azide in the standard concentration and buffer provided by the kit.

2.2.9 Image acquisition and processing

Images were acquired with a Zeiss Apotome/LSM 710 confocal microscope. Three images per culture chamber were taken at 10X magnification, thus sampling roughly half of the total area of the culture region. Acquisition parameters were not changed throughout the imaging of each experiment. ImageJ software (v. 1.47f- software for Java, National Institutes of Health, USA) was employed for all image processing. Cell morphology was evaluated by calculating nuclear shape index, cell shape index and cell spread area. The shape index is calculated as $4\pi \cdot \text{area}/(\text{perimeter})^2$ and ranges between one (circular shape) and zero (linear shape). This relationship was used to calculate both nuclear shape index and cell shape index. Nuclear shape index was automatically calculated by fitting ellipses to projected nuclei in binarized DAPI images and using perimeter and area values of the fit ellipses. About 500 cells per replicate were sampled for this analysis. Cell shape index was manually calculated by drawing cell outlines in Phalloidin images for a minimum of 20 cells per replicate. This operation also yielded cell area values. Only cells with clear, non-overlapping outlines were considered for this analysis. One blinded individual performed cell outlines drawing. Cell orientation was calculated as the angle formed by the main axis of the ellipse that fits a nucleus and the direction perpendicular to the strain, i.e. the channel main axis. For this specific parameter, statistical analyses were performed by comparing the fraction of aligned cells, where an aligned cell is a cell with a nuclear angle of $0^\circ \pm 10^\circ$ with the channel main axis.

Cell proliferation analyses were performed by estimating the nuclear expression of different cell proliferation markers. Nuclei positive for a given marker were manually counted and divided by the total number of nuclei (automatically counted) to estimate the level of expression. About 500 cells per replicate were screened for

proliferation analyses. YAP translocation analyses were performed by manually counting YAP-positive nuclei. In addition, calculations of nuclear fluorescence intensity were also performed in order to corroborate the manual counts. Nuclear fluorescence intensity was calculated by using the DAPI channel of images as a mask in the YAP channels to limit the calculation to nuclei only. Subsequently, the integrated signal density was extracted, corrected for background, normalized for nucleus area and used as final intensity value. For YAP localization analyses, about 500 cells per replicate were sampled with manual counts and at least 45 nuclei per replicate were analyzed with fluorescence intensity calculations.

2.2.10 Statistical analysis

All data are presented as mean \pm SD. Statistical comparisons were performed using GraphPad 5 (Prism) software. All data were initially analyzed for normality using Kolmogorov-Smirnov tests and then compared using parametric t-tests, one-way ANOVA or non-parametric Mann-Whitney or Kruskal-Wallis tests, where appropriate. A *p* value less than 0.05 was assumed as statistically significant.

2.3 Results

2.3.1 Microdevice characterization

Tracking displacements and calculating membrane full-field strains allowed for an in-depth characterization of the strain field experienced by cells in the culture chamber. A linear correlation was observed between average strain intensity and increasing negative pressures (Fig. 2.3A). Strain intensity reached about 8% at -600 mmHg, which is in good agreement with the strain values predicted by numerical simulations (Figure 2.2). Figure 2.3B shows 2D strain field maps for a representative

microdevice. The quantification of regional strain variations demonstrated the strain field uniformity (Fig. 2.3B): with an average applied strain of 5.7%, the average standard deviation of ϵ_{yy} values along both width and length of the channel resulted to be 0.3%. The strain field also resulted highly uniaxial with an average ϵ_{xx} value as low as 0.4%. No significant variation was observed in ϵ_{xx} values throughout most of the culture membrane. Only the lateral regions close to the chamber ends exhibited significantly different ϵ_{xx} values compared to all other regions (One-way ANOVA followed by Bonferroni post-hoc test, $p < 0.05$). For this reason, we defined a controlled strain field area of the culture membrane that extends for 4.5mm along channel length, where the total culture channel length is 5mm. This area is shown in Figure 2.3C and is the effective observation area sampled during subsequent cell culture experiments.

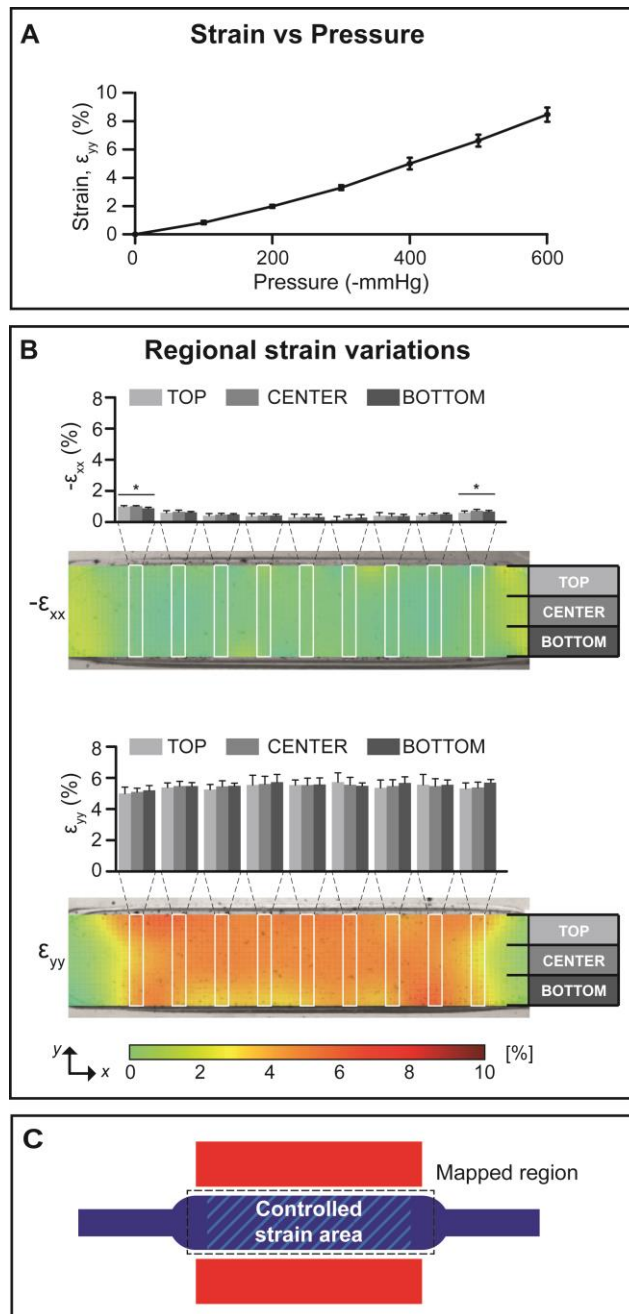


Figure 2.3 – A) Average strain intensity as a function of vacuum pressures. The relationship is nearly linear with a peak strain intensity of 8% at -600 mmHg, $n=10$. B) Strain field spatial characterization carried out by tracking graphite particles displacements. Color maps represent the strain field computed in the xx and yy directions by Digital Image Correlation algorithms applied to two representative images taken at -500 mmHg. The strain field results uniform and uniaxial. Histograms represent mean values of xx and yy strain component obtained from computed 2D maps ($n=3$ microdevices). Values were extracted from 9 regions along channel length (x -axis) and 3 regions (top, center, bottom) along channel width (y -axis). One-way ANOVA with Bonferroni post-hoc tests were performed to identify regions with variations on the strain field ($*=p<0.05$) C) Top-view of a culture chamber showing the region mapped for 2D strain maps generation (dashed black line) and the effective area of controlled strain, not taking into account lateral regions with excursions in xx strain component (white hatch pattern).

2.3.2 Cell morphology and cell orientation

Figure 2.4 shows representative images of CFs cultured under control, 2% cyclic strain and 8% cyclic strain conditions at 24h (Fig. 2.4A) and 72h (Fig. 2.4B) and their orientation, expressed as relative frequency distributions of angles between nuclear main axis and the longitudinal axis. Cell area (Fig. 2.4C) increased two-fold between 24h and 72h culture time only in control condition, whereas no significant change in cell area took place when cells were subjected to either 2% or 8% cyclic strain. Cell shape index decreased with the application of strain (Fig. 2.4D): cells cultured under 2% cyclic strain showed a slight significant decrease of their shape index after 24h and 72h, whereas a two-fold decrease is reported for cells subjected to 8% cyclic strain at both 24h and 72h. No significant change occurred in nuclear shape index (Fig. 2.4E) except for cells cultured for 72h under 8% cyclic strain that exhibited a slight significant reduction of the nuclear shape index. These results indicate cyclic strain as a general regulator of CFs elongation and size growth arrest. In addition, large strains (8%) trigger nuclear elongation, a phenomenon not induced by smaller strain fields (2%).

Cell orientation analyses were also performed after 24h and 72h at both 2% and 8% cyclic strain. The major effect we observed is a collective alignment of the cells main axis orthogonally to the strain field. This is a known cell behavior under cyclic strain⁹¹. We quantified this phenomenon with respect to time and intensity of the strain field. Statistical analyses of the number of aligned cells per condition (Fig. 2.4F) show that a significant increase of aligned cells only occurs with 8% cyclic strain and is more pronounced after 72h of 8% cyclic strain stimulus. Cells cultured under 2% cyclic strain showed no significant difference from control cells in terms of orientation. Accordingly, representative frequency distributions (Fig. 2.4A,B) of nuclear angles show a uniformly scattered distribution of angles in cells cultured in control condition

or under 2% cyclic strain whereas a preferential orientation towards the longitudinal direction is reported for cells subject to 8% cyclic strain.

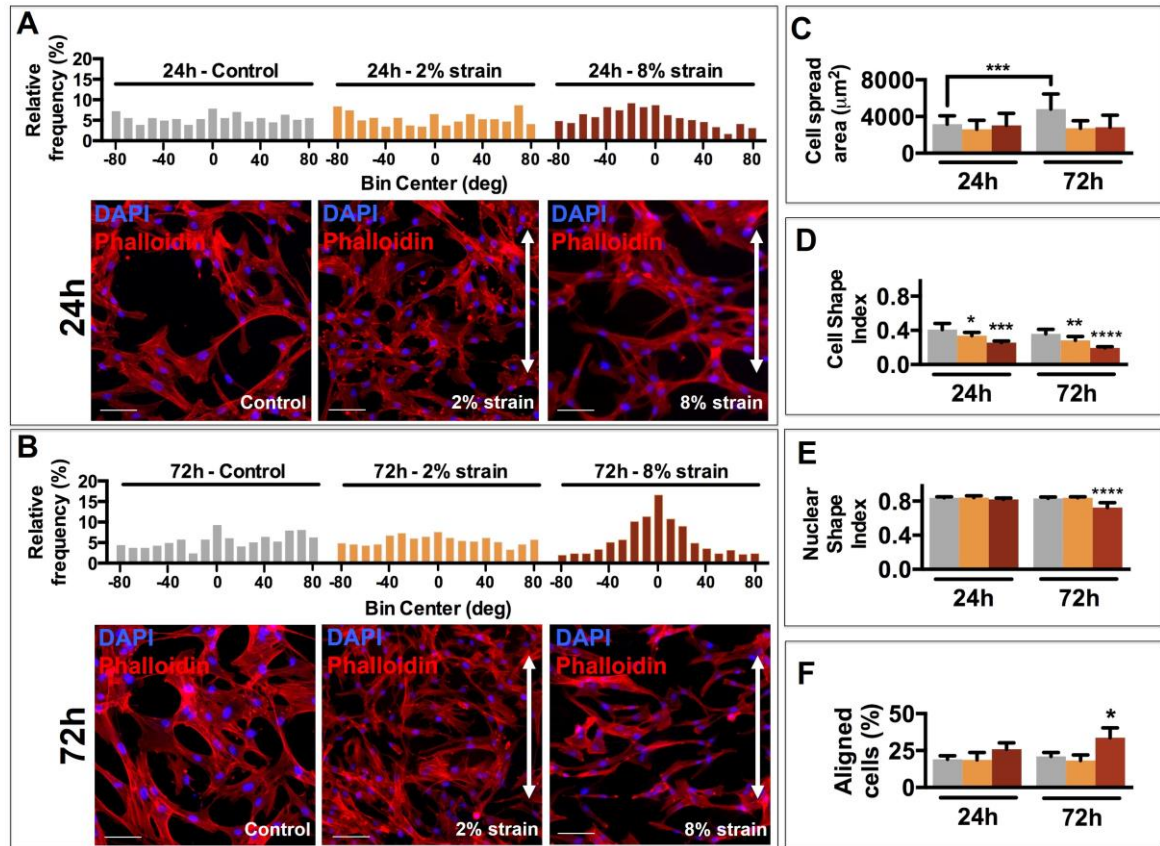


Figure 2.4 – Analysis of cell morphology. Representative images of human CFs stained for DAPI (blue) and Phalloidin (red) after 24h (A) and 72h (B) of control, 2% strain and 8% strain culture condition. Strain direction is indicated with white arrows. Bar graphs in panels A and B show frequency distributions of nuclear angles (bin width=20°) of corresponding representative images. Panel C shows calculations of cell area. Cells significantly increase their size only in control conditions. No increase in size is reported for either 2% or 8% strain conditions. Panel D shows cell shape index. Cell shape becomes elongated, increasingly with increasing strain intensity. Panel E shows nuclear shape index. A significant elongation of nuclear shape is reported only after 72h of 8% strain. Panel F shows the fraction of aligned cells per condition. Cells considered aligned are the ones showing an angle of $0^{\circ} \pm 10^{\circ}$ with the horizontal axis. Significant alignment along the horizontal axis occurs only after 72 hours of 8% cyclic strain. Scale bars=75µm. All conditions n=6 minimum. All comparisons analyzed with Kruskal-Wallis statistical tests except Cell and Nuclear Shape index analyses performed with one-way ANOVA tests with Dunnet's post-hoc comparisons. *=p<0.05, **=p<0.01, ***=p<0.001, ****=p<0.0001. Bar graphs color code: grey bars indicate control, orange bars indicate 2% strain and red bars indicate 8% strain.

2.3.3 Cell-cycle markers expression

To assess the effects of mechanical strain on CFs ability to proliferate, we performed immunofluorescence analyses to detect cellular antigens expressed in actively proliferating cells (Ki67), in mitotic cells (phospho-Histone-H3; PHH3) and by assessing the ability to synthesize DNA (labeling with EdU) indicative of cells in S phase. Figure 4 shows the results of these experiments and in particular the fraction of cells positive to the above markers with respect to time (24h and 72h) and strain intensity (2% and 8%) along with representative images.

No significant changes were found in the levels of Ki67 expressing cells (Fig. 2.5A,B). Figures 2.5C and 2.5D shows the fraction of cells that incorporated EdU: after 72h of stimulus, a two-fold significant increase in EdU incorporation was found in cells subject to 2% cyclic strain, whereas no variation occurred in cells subject to 8% cyclic strain. The statistical significance of this result was corroborated by additional analyses that took into account the influence of cell density on EdU incorporation: Figure 2.6 shows the EdU incorporation values plotted against the cell density in which they were observed. We tested whether slopes and intercepts of the linear fits were statistically different (analysis of covariance test, ANCOVA). We found that slopes did not differ significantly between all three conditions, whereas intercept of 2% strain linear fit is significantly higher than control and 8% strain linear fits ($p=0.0063$). Intercepts of 8% strain linear fit *vs.* control condition linear fit did not differ significantly. We can conclude that EdU incorporation values are significantly higher in 2% strained cells compared to control and 8% strain conditions.

Interestingly, cyclic strain induced an up-regulation of PHH3 labeling (Fig. 2.5E,F,G) as well. In particular, in control cultures ~0.5% were mitotic cells after both 24h and 72h. Cells cultured under 2% cyclic strain showed a four-fold increase in the

expression of PHH3 (2% of mitotic cells), a result that is stable in time from 24h to 72h. Cells cultured under 8% cyclic strain showed a similar increase in mitotic cells only at 24h, with values of PHH3 expression decreasing to the same level as controls after 72h of stimulus. Finally, by performing standard nuclei counts to evaluate the number of cells in each culture condition, we observed that cells subjected to 2% cyclic strain significantly increased in number compared to both control and 8% strain conditions (Fig. 2.5H).

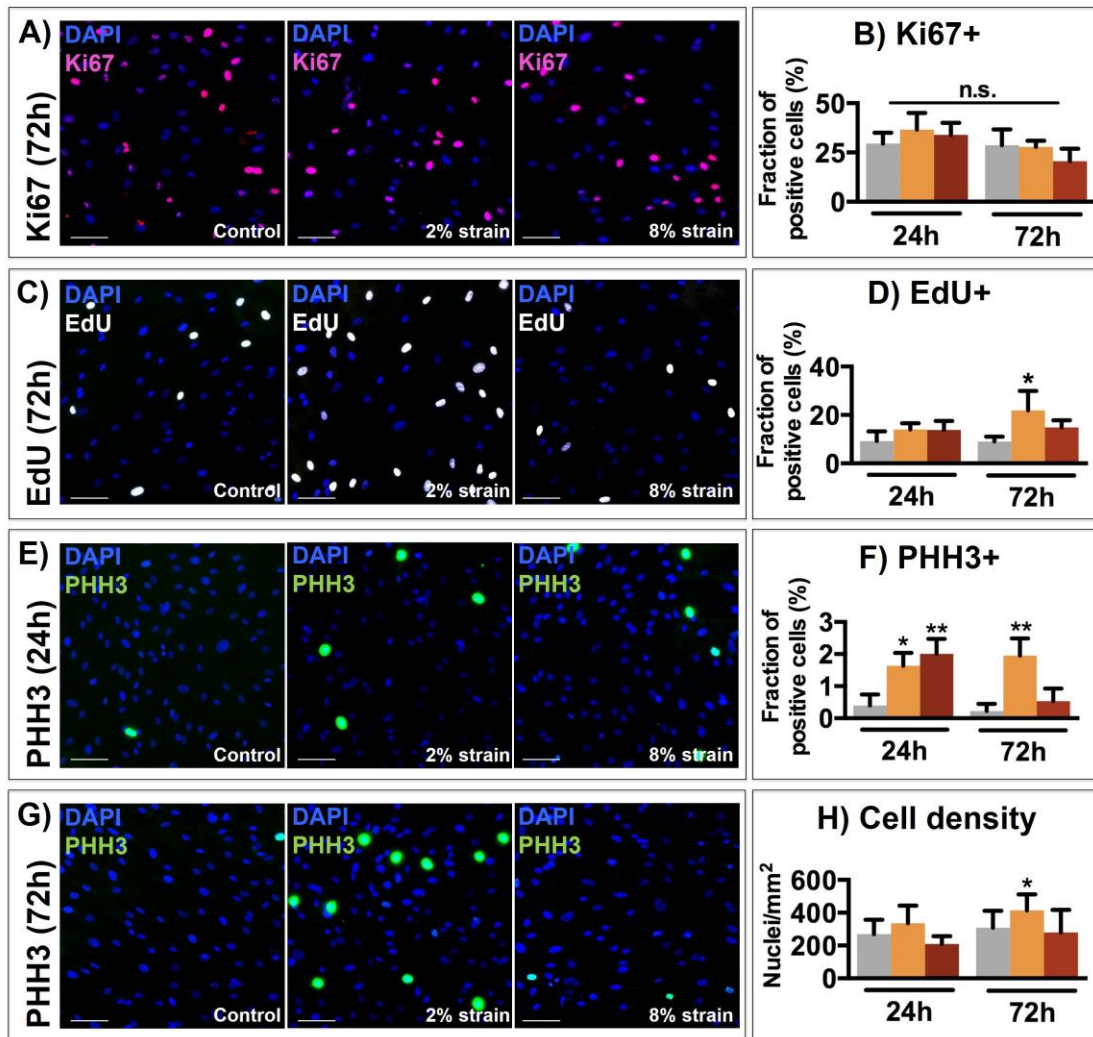


Figure 2.5 – Cell proliferation analyses. A) Images of human CFs fixed after 72h of control, 2% strain or 8% strain conditions and stained for DAPI (nuclei, blue) and Ki67 (whole cell cycle, pink). B) Expression of Ki67 in all conditions. No significant change is reported. C) Images of DAPI (blue) and EdU (S-phase, white) incorporation stainings after 72h. D) Expression of EdU in all conditions. Increased DNA synthesis is reported for 2% strain after 72h. E,G) Images of DAPI and PHH3 (mitotic phase, green) stainings after 24h (E) and 72h (G). F) Expression of PHH3 in all conditions. A significant increase in cell mitosis is reported for 2% strain at all time-points and for 8% strain only after 24h. H) Cell density calculated from nuclei counts. Cells significantly increase their density after 72h of 2% strain. All conditions $n=4$ minimum. Scale bars=75 μ m. All comparisons analyzed with Kruskal-Wallis tests except Cell Density data analyzed with One-way ANOVA with Dunnet's post-hoc comparisons. $*=p>0.05$, $**=p<0.01$. Bar graphs color code: grey bars indicate control, orange bars indicate 2% strain and red bars indicate 8% strain.

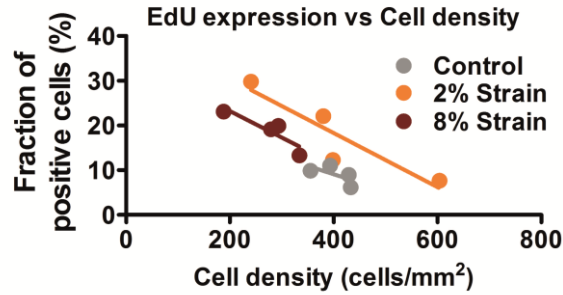


Figure 2.6 – Expression of EdU with respect to cell density values. Linear fits were calculated for control ($R^2=0.49$), 2% strain ($R^2=0.73$) and 8% strain ($R^2=0.49$) conditions and analysis of covariance tests were performed to determine if slopes and intercepts were significantly different between conditions. The intercept of linear fit of 2% strain values is significantly higher than intercepts of the other two conditions. This further demonstrates the increased proliferative effect of 2% strain condition.

2.3.4 YAP localization

The nuclear translocation of YAP has been directly involved in the control of mitotic checkpoints associated to differential cytoskeletal tension^{85,86} as well as in a cyclic strain-induced proliferation of epithelial cell lines⁹². Since the cytoskeleton was differentially affected by 2% and 8% strain conditions, and in light of the proliferative responses of CFs under different strain conditions, we investigated whether the effect of on-chip cyclic strain stimulation was associated with modifications in the subcellular distribution of the YAP protein. We manually quantified the localization of YAP as nuclear or cytoplasmic by visual discrimination. Given the subjective nature of this count, this data were corroborated with calculations of nuclear fluorescence intensity. Both strain conditions caused a significant nuclear translocation of the YAP protein after 72h of strain (Fig. 2.7).

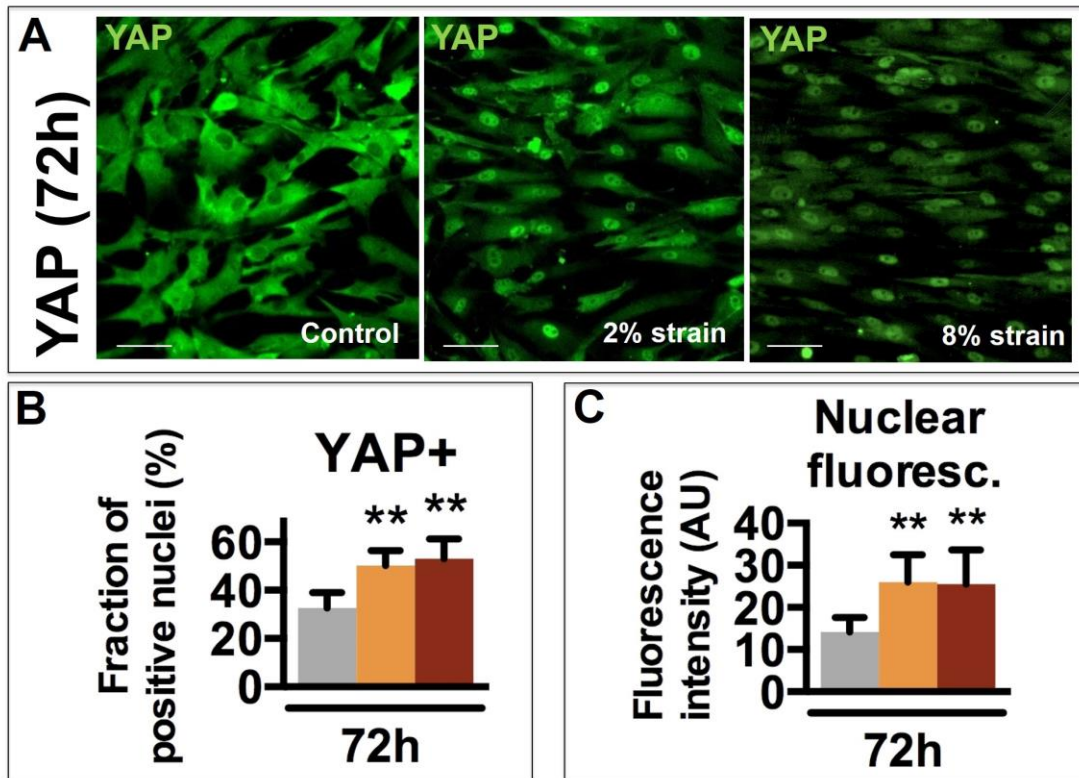


Figure 2.7 – YAP localization analyses. A) Images of human CFs fixed after 72h of control, 2% strain or 8% strain conditions and stained for YAP (green). Scale bars = 50 μ m. Bar graphs show the manual count of YAP positive nuclei (B) and the quantitative nuclear fluorescence intensity calculations (C). 2% and 8% strain similarly increase nuclear localization of YAP. All conditions n=4 minimum, Kruskal-Wallis test, **= $p < 0.01$. Grey bars indicate control, orange bars indicate 2% strain and red bars indicate 8% strain.

2.4 Discussion

Activation, proliferation and differentiation of CFs into pro-inflammatory and matrix stiffening cells is a critical step in the development of pressure overload- or ischemia-related myocardial fibrosis. It is unclear, however, if mechanical load is involved in this phenomenon *in vivo* and, at present, literature is lacking robust *in vitro* data focused on human CFs proliferation control under mechanical cues such as cyclic strain. Elucidation of these effects requires the investigation of detailed cellular behaviors such as modulation of growth and proliferation in cells subjected to highly uniform, controlled and truly uniaxial strain fields.

In this work we designed, fabricated and characterized a microdevice for cyclic uniaxial strain of cell monolayers with rigorous quantification of the real mechanical stimulus applied. Inspired to a previous design, the lung-on-a-chip²⁹, we developed a platform that was compatible with standard biological laboratory requirements in terms of throughput and ease of use. We successfully produced uniform 8% membrane strain by applying vacuum to both upper and lower halves of the side actuation chambers, achieving this by simple manual cuts of the thin membrane, without employing chemicals for PDMS etching as in previously described microdevices. The produced strain resulted extremely uniform and uniaxial (no significant excursions of ϵ_{yy} values throughout the membrane and ϵ_{xx} strain values closely approaching zero), a feature present with a significantly lower level of control in other stretching devices. In addition, we included four test sites per device, in order to enable quick screenings and higher throughputs. Although not exploited in the present study, the microfluidic platform was also provided with an embedded lower fluidic system for the environmental conditioning of cultured cells in all four culture chambers. The main limitations of the platform, related to the small volume of the culture chambers, are the small number of cells to perform gene and protein expression analyses and the frequent medium changing requirements.

We employed this microdevice to screen human heart-derived adult CFs responses to different cyclic strain intensities. Due to the small dimensions of typical heart biopsies, the supply of human heart-derived CFs is limited. Previous cyclic strain studies of human CFs were indeed performed on purchased cells, rather than on CFs freshly isolated from tissue samples⁵². By employing our custom-designed microdevice, we managed to perform experiments on cells freshly isolated directly from atrial tissue. Typical amplification steps were required, that may cause alterations

in cellular behavior with respect to the in vivo condition. However, the small number of cells needed to load each culture chamber of the microdevice enabled us to conduct experiments after only two amplification passages before functional analyses, thus maximizing the reliability and the relevance of the results. We subjected cells to controlled 2% cyclic strain and 8% cyclic strain: although these strain intensities are simplified mechanical conditions representative of a more complex physiological mechanical stimulus, we related the 8% strain condition to the average strain field sensed in the physiological cardiac cycle, whereas we suggest that 2% strain may represent a fibrotic mechanical environment, where the myocardial ability to contract is reduced. We based these approximate values on imaging studies reporting that cardiac strain fields have lower intensities in regions where the onset of cardiac fibrosis caused stiffening and reduced contractile ability of the myocardium ^{93,94}.

We first explored the effects of differential cyclic strain intensities and straining time on CFs morphology. We observed strain-specific effects on cellular alignment along the orthogonal direction to the strain field, that occurred consistently only with a higher 8% strain level and especially after 72h of stimulation. This is consistent with literature on stretched fibroblasts, although shorter time-scales have been reported for skin fibroblasts ⁹⁵. By contrast, no major rearrangement was observed in cells undergoing lower 2% cyclic strain. The modifications in cell elongation show that, although not altering the cellular orientation, 2% cyclic strain was able to consistently engage the CFs cytoskeleton by increasing cell elongation. However, this elongation effect is significantly more pronounced and affects the nuclear shape only when cells are subject to 8% cyclic strain. We also report that cyclic strain hinders cell size growth similarly for 2% and 8% strains.

We then explored the proliferative response of CFs, focusing on different cell proliferation markers: the results clearly show strain- and time-dependent effects of cyclic mechanical load on CFs modulation of proliferation. 2% strain consistently elevated the percentage of cells showing high PHH3 levels at the two stimulation times. This coincided with a significant increase of EdU⁺ cells at 72h and a net increase in cell density at the same time point (Fig 2.5). Conversely, 8% strain led to a similar response only after 24h, followed by a rapid PHH3 drop at 72h. This event was neither accompanied by an increment in EdU uptake nor by a net increase of cells compared to the controls. Contact inhibition of proliferation did not play a role in time-dependent proliferation dynamics as shown by cell density analyses (Fig. 2.5H and Fig. 2.6). In addition, it is worth noting that time-dependent proliferation changes were not considered in previous cyclic strain experiments on rat CFs, in which the applied stimuli lasted from 4h⁶⁴ to a maximum of 24h^{62,63}. Our findings therefore provide novel insights demonstrating a differential response of human CFs to cyclic strain intensity involving stable or transient increase of cell mitosis. The comparison of these findings relative to human-derived cells with previous results on rat CFs proliferation under cyclic strain remains elusive, mainly due to the different stimuli employed by different studies: decreased proliferation occurred when rat CFs were subject to 5% uniaxial strain⁶³ and to equibiaxial strain⁶², no strain intensity reported; Butt and Bishop, 1997, 20% maximum strain); increased proliferation occurred when rat CFs were subject to biaxial strain (Dalla Costa et al., 2010, no strain intensity reported). However, it is worth noting that cardiac remodeling events have been shown to retain distinctive and species-specific features⁹⁶.

It is of interest to compare cell morphologies and proliferation rates exhibited by CFs in the two strain stimulation regimes. Indeed, internal cytoskeletal tension has been

tightly related to cell shape and this, in turn, has been found to modulate cell proliferation. For example, studies on human aortic SMCs ⁹⁷, ECs ⁹⁸ and human umbilical vein endothelial cells ⁹⁹ have shown that inducing cell elongation via micropatterning leads to decreased cell proliferation only when the nuclear shape is affected and the nucleus becomes more elongated. Consistent with this, our data show that the decrease in the percentage of PHH3⁺ cells at 72h (8% strain) coincided with a consistent modification in nuclear and cell shape and with cell alignment. No late inhibition of the proliferative response occurred in 2% cyclic strain conditions, where no significant changes in nuclear morphology or cell alignment were detected. Deeper investigations are required to demonstrate and elucidate the relations between cell-shape, internal cytoskeletal tension, external mechanical forces and the strain-induced control and modulation of human CFs proliferation.

To gain some insight into possible interactions between mechano-sensing and modulation of proliferation, we explored the activation and translocation of YAP. Interestingly, Codelia, *et al.*, showed that applying cyclic strain (20%, 1Hz, 6h duration) to an epithelial cell line resulted in increased cell proliferation mediated by YAP activation and translocation in the nucleus ⁹². Our results show a consistent reallocation of YAP from cytoplasm to the nucleus in both 2% and 8% strain conditions after 72h of stimulus (Fig. 2.7). Interestingly, the levels of nuclear translocation are similar at both strain intensities suggesting a possible saturated activation of the YAP-dependent mechano-sensing pathway. While this nuclear reallocation is in line with the recently highlighted role of YAP in cell mechano-sensing, the time-dependent restrained proliferation of CFs after 72h at 8% strain also suggests that YAP nuclear localization may indeed act independently from proliferation control or may be not sufficient by itself to elicit a continuous and sustained strain-induced proliferation. In summary, the

results here shown pave the way for further studies into the regulation of strain-induced proliferation and highlight the importance of time-dependent effects on mechanosensing and modulation of proliferation.

2.5 Conclusions

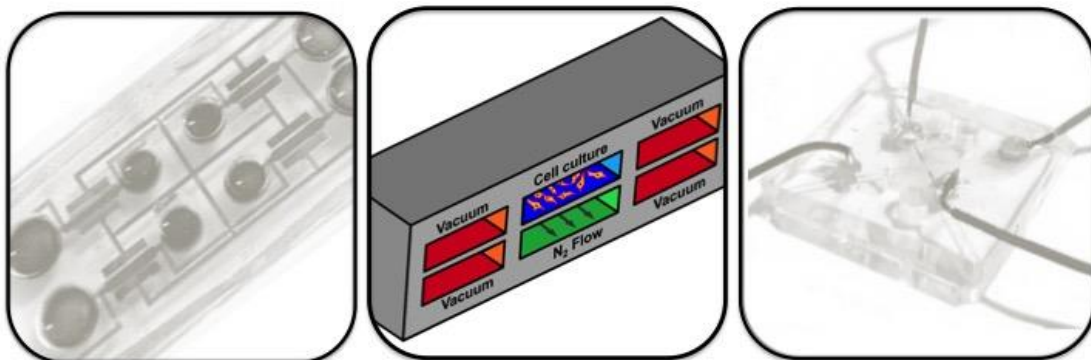
In this work we have designed, developed and employed a microdevice for application of uniform and uniaxial cyclic strain to cell monolayers. We designed this device specifically to minimize the number of cells required and to increase throughput and ease of use. We characterized the strain applied and then employed the microdevice to investigate biological responses of human heart-derived adult CFs to cyclic strain. Mechanical load-dependent effects on CFs proliferation were observed with significant proliferation increase under strain intensities (2%) representative of reduced myocardial contractility, whereas a more moderate, time-dependent proliferative behavior occurred under more physiological strain intensities (8%). These findings suggest the existence of a cellular control of CFs proliferative behavior that acts with a dependency on the amount of the sensed mechanical stimulus and that could be involved in the pathological evolution of cardiac fibrotic disease.

3.

Combining oxygen control and mechanical strain in a multi-stimulus microplatform for studying cardiac fibroblasts in ischemic conditions

Biological experiments and image acquisition described in this chapter were carried out at *Biosystems and Micromechanics IRG (BioSyM)*, Singapore-MIT Alliance for Research and Technology, Singapore (SINGAPORE)

This chapter partially refers to a manuscript in preparation. As such, it contains preliminary data that may be revised for publication.



Rationale

In this chapter an incremental technical improvement of the cell-stretching microplatform presented in Chapter 2 is described. A common lower fluidic channel flowing below all four stretching units of the microdevice is implemented as an oxygen-controlling system to modulate the environment of the cell culture membrane in terms of oxygen concentrations and dynamics. With preliminary numerical simulations, the estimation of oxygen partial pressures on the culture membrane is described upon application of a nitrogen gas mixture in the lower fluidic channel. After careful experimental characterization of oxygen concentrations on the culture membrane, the device is finally employed as a multi-stimulus platform. Indeed, both mechanical strain and oxygen deprivation are fundamental stimuli of the cellular environment in cardiac pathology: upon myocardial infarction, rapid decrease of blood supply to the cardiac tissue causes cardiac cells to sense near-zero oxygen levels. While contractile cardiac myocytes do not survive in this harsh condition, cardiac fibroblasts are the main responsible of tissue healing and remodeling.

By controlling oxygen concentrations with microchannels, it was possible to apply rapid and controlled oxygen dynamics, a factor that has proved to be increasingly important in recent research showing dramatically different cellular responses depending on particular oxygen dynamics (e.g. reperfusion injury or ischemic preconditioning). After subjecting cells to controlled patterns of cyclic strain intensities and oxygen concentrations dynamics, we analysed the response of human cardiac fibroblasts and dissected relative and synergistic contribution of mechanical strain intensities and oxygen levels in the modulation of responses such as proliferation, extra-cellular matrix production, electrical coupling, mechano-transduction and inflammatory molecules secretion. With data analyses currently on-going, the present

chapter contains preliminarily processed data on cell proliferation and collagen I intracellular production. The results of this analysis shows an interesting pattern of cardiac fibroblasts activation of matrix production and proliferative pathways depending on the stimulus applied: oxygen deprivation dramatically increases both proliferation and collagen I production by cardiac fibroblasts; mechanical strain alternatively activates proliferative pathways or collagen I production depending on strain intensity. This outcome firstly describes the combined contributions of relevant physical and chemical stimulations on pathological cardiac developments.

3.1 Introduction

3.1.1 Myocardial remodeling after ischemic insult: the role of cardiac fibroblasts

Sudden loss of blood flow in coronary arteries is the main cause of myocardial infarction, one of the most severe and life-threatening cardiac conditions representing a leading cause of death worldwide. When supply of oxygen and nutrients to the myocardium is critically reduced (ischemia), a complex tissue response takes place: within hours tissue necrosis and death of contractile cardiac myocytes occurs in the infarcted area giving rise to an inflammatory phase that recruits immune cells and activates quiescent cardiac fibroblasts (CFs); within a few days a proliferative phase begins where activated CFs invade the infarcted area, degrade and replace the extracellular matrix with a collagen-based scar; within weeks the maturation of the fibrotic scar is completed^{100,101}. This essential process maintains tissue integrity and avoids critical consequences such as cardiac ruptures or aneurysms, however, adverse and pathological remodeling often occurs when CFs persist in their function and excessively remodel infarcted and non-infarcted areas^{47,102}. This outcome is associated with cardiac dysfunction and increased mortality and current advances in the design of anti-fibrotic drugs require a deeper understanding of molecular and cellular mechanisms underlying fibrosis^{103,104}.

CFs are known to be primarily involved in all phases of cardiac tissue healing and remodeling. In particular, CFs respond to pathological myocardial conditions such as acute ischemia by proliferating and changing their phenotype to myofibroblasts – a differentiated matrix-remodeling cell type expressing smooth muscle markers (α -SMA)^{44,46,47,105}. Previous investigations have linked CFs proliferation and phenotype

changes to several physico-chemical stimuli related to cardiac injury such as biochemical signaling^{106–108}, mechanical stress^{48,49} and low oxygen levels^{109,110}.

Differences in the mechanical stress sensed by CFs play a crucial role in the differentiation into activated myofibroblasts^{52,53,61}. Interestingly, strain intensity-dependent effects have been observed both in terms of proliferation¹¹¹ and matrix deposition¹¹². CFs were also exposed to different oxygen levels and a complex oxygen sensing response has been suggested: CFs are thought to be sensible to O₂ levels variations from physoxia (PX), defined as the physiologic oxygen level in living tissues (about 5% O₂ in the myocardium). Both hypoxia (HX, 1-3% O₂, defined as oxygen levels lower than physoxia) and normoxia (NX, 21% O₂, defined as the standard oxygen levels of ambient air) induce α -SMA expression and a pro-inflammatory and fibrogenic phenotype^{113,114}.

3.1.2 *In vitro* platforms and models of cardiac ischemia

Most *in vitro* studies recreate the ischemic insult by culturing cells in incubators with oxygen control; however, such controlled oxygen incubators pose drawbacks not only in terms of costs but also in terms of ability to accurately control oxygen levels, particularly in fast dynamics conditions. Indeed, featuring equilibration times of hours, oxygen incubators are suitable for steady state experiments¹¹⁵. Time scales and dynamics of oxygen concentrations changes are principal regulators of cellular responses in cardiac injury events: abrupt hypoxic stimuli (with levels of oxygen dropping in seconds or minutes) are known to elicit specific cellular responses after minutes or few hours¹¹⁶; tissue re-oxygenation after a period of ischemia is thought to induce a severe tissue damage known as reperfusion injury^{117,118}; brief cycles of

ischemia/re-oxygenation are known to cause a protective effect on cells exposed to a subsequent prolonged insult (ischemic preconditioning)^{119–121}.

The understanding of such complex cellular responses could provide significant advancements in the design of reparative strategies for healing myocardial injuries. Moreover, coupling standard oxygen control incubators with standard devices for physical stimulation of cells is challenging due to the complex and bulky systems required. Indeed, despite the physiological relevance of both stimuli, to date there is no report on cardiac cells subject to combined oxygen dynamics and mechanical strain.

Advanced *in vitro* models that allow cell culture under physical and chemical stimuli, applied with precise spatio-temporal control, are of significant interest to explore cellular behavior in physiologically relevant conditions. To this aim, organotypic microfluidic models developed during the last decade successfully provided complex patterns of physico-chemical stimuli to cultured cells together with a cost-effective trend towards culture platforms miniaturization²⁴. *In vitro* models of cardiac environments include: thin films for contractility studies¹²², a heart on a chip platform able to apply cyclic strain to 3D cardiac micro-tissues³⁴, a multi-stimulus platform providing electrical and mechanical stimulations to 2D cell monolayers³³. Advanced micron-scale models of ischemic heart injury would help in unraveling the contributions required to the beneficial and detrimental CFs-mediated tissue remodeling and in improving the therapeutic targets. Controlling oxygen concentrations in defined micro-geometries has the advantages of reducing equilibration times and allowing for precise control, with the possibility of reproducing complex dynamics^{116,123}.

In this work we characterized and employed a microdevice for simultaneous application of cyclic mechanical strain and controlled hypoxic stimuli. Building on a

previously described multi-chamber mechanical strain microdevice, we integrated and characterized a conditioning layer for environmental control of oxygen levels in the culture chamber and performed multi-stimulus experiments on CFs exposed to different strain intensities and different oxygen dynamics. In particular, we were able to subject CFs to constant physoxia (PX), to an abrupt reduction of oxygen supply (hypoxia, HX) and to a subsequent re-oxygenation to physoxic levels (reperfusion, REP) while concurrently exposing cells to different cyclic strain intensities. We evaluated separate and combined effects of these stimuli on cell proliferation and intracellular collagen production.

3.2 Materials and Methods

3.2.1 Microdevice outline

The microdevice was fabricated as previously described in Chapter 2¹¹¹. Briefly, four stretching units are arranged in a single device composed of a thin polydimethylsiloxane (PDMS) membrane sandwiched between two microstructured PDMS layers. Figure 3.1 shows a cross-section of a stretching unit of the device. In each stretching unit, a central culture chamber (blue) is flanked by two actuation chambers (red) connected to a single actuation line, meant for vacuum application and straining of the central membrane. A lower fluidic channel (green), common to all units, is designed for environmental conditioning and flows below each central culture chamber. The pneumatic system dedicated to the application of uniform and uniaxial strain was extensively characterized and employed in Chapter 2. In this Chapter, we employed the lower conditioning channel to flow a nitrogen (N₂) gas mixture, thus modulating hypoxic conditions in the culture chambers.

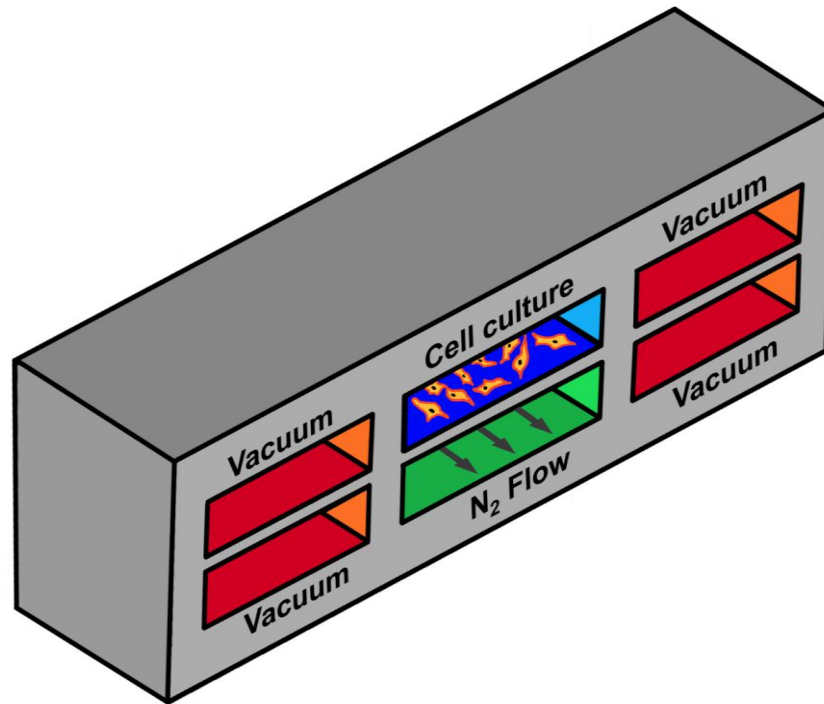


Figure 3.1 – A 3D sketch of the stretching unit cross section. A thin PDMS membrane is sandwiched between a top and a bottom layer forming three functional compartments: an upper culture chamber (blue) hosting cultured cells; two side actuation chambers where applied vacuum pressure generates uniform strain of the culture membrane; a lower fluidic channel where a N_2 gas flowrate conditions oxygen levels on the culture membrane.

In particular, we characterized oxygen concentration changes provided by means of the lower conditioning channel in terms of several technical aspects. We aimed at proving that the lower conditioning channel provides oxygen level alterations that are not influenced by the operating condition of the device (single stimulus or multi-stimulus mode); that are robust and uniform inside the single culture membrane and within the four culture chambers of the microdevice; that can be applied at microdevices incubated at different oxygen levels (e.g., in a myocardium-physoxic environment at 5% O_2 or in a normoxic environment at 21% O_2); that exhibit fast dynamics, suitable to complex changes of oxygen levels. In this scenario, a numerical model aided the investigation by providing information on the uniformity of the oxygen tension inside a single culture chamber and by assessing the results in different operating condition and in different ambient oxygen levels. An experimental setup for

oxygen concentration measurements served to validate the numerical model and to provide experimental data (obtained only in a normoxic environment) on time constants and on O₂ membrane concentration levels in different culture chambers of the same device, upon application of different flowrates.

3.2.2 Microdevice characterization

We experimentally measured oxygen concentrations in the culture chambers upon application of a controlled, deoxygenating gas flowrate in the conditioning channel. A humidified mixture of 95% N₂ 5% CO₂ was flowed in the conditioning channel and oxygen concentrations were recorded in the central region of each culture chamber by means of a needle-based oxygen sensor (PreSens GmbH, Germany). The vertical position of the oxygen-sensing probe was adjusted with a micromanipulator to reach the proximity of the culture membrane. We measured the equilibrium value at different flowrates (namely 5, 15 and 50 ml/min) in all four culture chambers, and repeated the test in four different microdevices. We also estimated the equilibration time-constants of the deoxygenation phase when the gas flowrate was applied and the re-oxygenation time constant when the gas flowrate was stopped. For evaluation of time-constants, oxygen concentration data were acquired every 3 seconds. We performed all experimental measurements in humidified ambient air at 37°C, therefore in a normoxic environment (21% O₂).

3.2.3 Numerical model

The spatial distribution of oxygen tension in the device functional compartments was preliminarily evaluated through a computational model with the aim of estimating

equilibrium values and uniformity of the hypoxic stimulus on the culture membrane when aspects of the microdevice functioning were simulated: operating conditions (strain mode only, hypoxic stimulus only or combined stimuli) and oxygen levels of the ambient surrounding the device (normoxic environment or physoxic environment). A 2D geometrical model of the stretching unit cross-section was implemented with Comsol Multiphysics 4.3 (Comsol, Inc., Burlington, MA), comprising top and bottom PDMS layers, culture chamber, thin membrane, lower fluidic chamber and side actuation chambers. Geometric parameters are identical to the model described in the previous chapter (see Table 2.1), with the exception of the total top and bottom layer heights. Since the total height of the PDMS layers is a key parameter in the exchange of oxygen between the channels and the surrounding environment, the actual PDMS height parameters ($h_{top}= 2.8\text{mm}$ and $h_{bot}= 1.4\text{mm}$) were included in the model. For clarity, the model is shown in Figure 3.2. The model geometry was discretized with a mesh scheme consisting of triangular elements. A mesh sensitivity analysis was performed to determine the optimal number of elements and element size. To this aim, oxygen partial pressures on 4 reference points of the culture chamber were evaluated for increasingly fine mesh schemes upon application of a fixed oxygen partial pressure at the lower conditioning chamber boundaries. These parameters were found to reach an asymptotic value for a mesh scheme consisting of about 5000 elements featuring a maximum characteristic size of $66\ \mu\text{m}$ and a minimum characteristic size of $0.1\ \mu\text{m}$. The material properties relative to oxygen (diffusion coefficient, D ; solubility, S) were assigned as follows:

- PDMS Sylgard 184 ($D_p = 4 \cdot 10^{-9}\ \text{m}^2/\text{s}$; $S_p = 1.25\ \text{mM}/\text{atm}$) was assigned to the bulk structure (Figure 3.2, grey)

- Water ($D_w = 2 \cdot 10^{-9} \text{ m}^2/\text{s}$; $S_w = 0.218 \text{ mM/atm}$) was assigned to the culture chamber (Figure 3.2, blue)

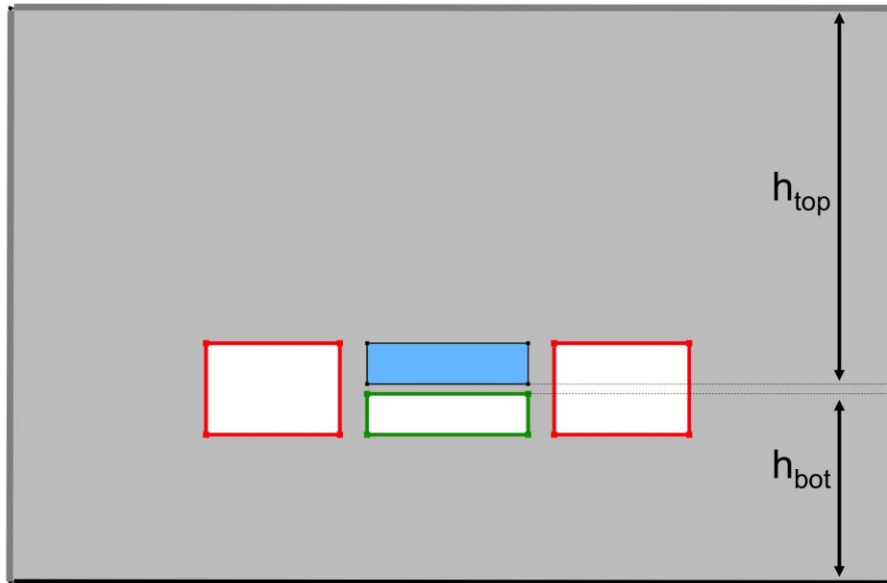


Figure 3.2 – Cross sectional geometry of the model employed in numerical simulations. Geometric parameters are equivalent to the model employed in Chapter 2 (see Table 2.1) with the exception of $h_{top} = 2.8\text{mm}$ and $h_{bot} = 1.4\text{mm}$. Grey surface represents PDMS material and blue surface represents water. Colored bold lines represent the boundaries where appropriate boundary conditions were applied to model operating conditions of the device. Black bold line represents the bottom surface of the device and was always modeled as a ‘no exchange’ boundary condition; thin black lines represent culture chamber boundaries and were always modeled as a ‘free exchange’ condition; grey bold lines represent the outer faces of the devices; red bold lines represent the side chambers boundaries; green bold lines represent lower chamber boundaries. A complete list of partial pressure values used as boundary conditions to model different device operating conditions and ambient oxygen levels is provided in Table 3.1.

Relevant boundary edges are highlighted in Figure 3.2: the lower face of the device (bold black line) was modeled as a ‘no exchange’ boundary condition, being this side mating the gas-impermeable plastic of Petri dishes. The culture chamber boundaries (thin black lines) were modeled as ‘free exchange’ conditions. The boundaries of the conditioning channel (green bold lines), side actuation chamber (red bold lines) and outer faces (grey bold lines) were assigned constant partial pressures, with values depending on the operating condition or ambient oxygen-level to be

modeled. All simulations were performed with the *Transport of Diluted Species* module and by solving a stationary study.

A preliminary validation of this model was carried out by evaluating oxygen tension on the culture membrane when outer faces and side actuation chambers were assigned constant ambient oxygen tension (159 mmHg) and the conditioning channel was assigned oxygen tension of the nitrogen gas mixture (experimentally measured to be 2 mmHg). Oxygen tension average values extracted from the central region of the culture membrane (800 μ m width, avoiding near-walls regions) and within a 20 μ m-thick vertical slice were compared to experimentally measured values performed in comparable conditions (microdevice in ambient air and nitrogen flowrate of 15 ml/min in the conditioning channel. Table 3.1).

	Numerical	Experimental
Membrane		
pO₂	7 \pm 0.5 mmHg (0.9 \pm 0.05%)	9 \pm 1 mmHg (1.2 \pm 0.1%)

Table 3.1 – Membrane values obtained from the numerical modeling of a N₂ gas mixture in the conditioning channel and membrane values recorded experimentally with a flow of N₂ gas mixture in the lower conditioning channel. The model predicts experimental values with good accuracy.

Despite not taking into account convective transport due to the flow of nitrogen gas, the model is able to predict experimental values in a standard condition. The model was subsequently employed to evaluate the spatial 2D distribution of oxygen partial pressures in the microdevice cross-section simulating two relevant aspects:

- **Operating conditions:** whether the device is employed only in oxygen-conditioning mode (N₂ gas mixture in the conditioning channel), only in cyclic

strain mode (vacuum pressure in the side actuation chambers) or operated with both stimulations simultaneously.

- **Ambient oxygen level:** whether the environment surrounding the microdevice is normoxic or physoxic. We investigated this parameter in order to evaluate whether the oxygen levels of the surrounding environment influence the hypoxic stimulus provided by the device.

The following operating conditions were therefore investigated:

- **HX/0% Strain:** N₂ gas mixture is applied in the lower fluidic channel and no vacuum is applied to the side chamber

- **HX/8% Strain:** N₂ gas is applied in the lower fluidic channel while the side chambers switch between vacuum pressure (-600 mmHg) and atmospheric pressure

- **8% Strain:** the lower fluidic channel is left open to the ambient atmosphere while the side chambers switch between vacuum pressure (-600 mmHg) and atmospheric pressure

The above operating conditions were modeled by applying specific boundary conditions to the edges represented as bold lines in Figure 3.1. In particular, Table 3.2 shows the boundary conditions applied to model operating conditions and different oxygen levels of the ambient surrounding the device.

		Lower chamber boundaries	Side chambers boundaries	Outer faces boundaries
HX / 0% Strain	NX Ambient	Hypoxia pO ₂ = 2 mmHg	Ambient pO ₂ = 159 mmHg	Ambient pO ₂ = 159 mmHg
	PX Ambient	Hypoxia pO ₂ = 2 mmHg	Ambient pO ₂ = 38 mmHg	Ambient pO ₂ = 38 mmHg
HX / 8% Strain	NX Ambient	Hypoxia pO ₂ = 2 mmHg	Strain pO ₂ = 96 mmHg	Ambient pO ₂ = 159 mmHg
	PX Ambient	Hypoxia pO ₂ = 2 mmHg	Strain pO ₂ = 23 mmHg	Ambient pO ₂ = 38 mmHg
8% Strain	NX Ambient	Ambient pO ₂ = 159 mmHg	Strain pO ₂ = 96 mmHg	Ambient pO ₂ = 159 mmHg
	PX Ambient	Ambient pO ₂ = 38 mmHg	Strain pO ₂ = 23 mmHg	Ambient pO ₂ = 38 mmHg

Table 3.2 – Detailed list of boundary conditions values applied to the three relevant boundaries in order to model three operating conditions of the device and two different ambient oxygen concentrations (normoxic and physoxic).

Where the values were set as follows:

- Ambient pO₂ was set either at 159 mmHg (21% O₂, normoxia) or at 38 mmHg (5% O₂, physoxia)
- Strain pO₂ was set as the average of Ambient pO₂ and the pO₂ at a vacuum pressure of -600mmHg (96mmHg when Ambient pO₂ = 159 mmHg; 23 mmHg when Ambient pO₂ = 38 mmHg). This is to model a square vacuum pressure signal switching between atmospheric pressure and a vacuum pressure of -600mmHg.
- Hypoxia pO₂ was set at 2 mmHg: the experimentally measured oxygen partial pressure in the N₂ gas due to non-ideal gas exchange along the length of tubing connecting the tank and the microdevice

After solving stationary studies, the distribution of oxygen partial pressures was evaluated by means of 2D color maps of the entire cross section or by assessing the

average oxygen partial pressures in a 20 μ m-thick region along the width of the culture membrane (1200 μ m width)

3.2.4 Stimulation system and parameters

Figure 3.3 shows the experimental design of biological experiments performed in the present work. We combined mechanical and dynamic oxygen stimulations and evaluated their relative and synergistic contributions in terms of cell proliferation and collagen production. The importance of different intensity levels of mechanical strain has been previously highlighted in Chapter 2¹¹¹. We employed three mechanical stimulation regimes: a static control (0% strain), 2% strain and 8% strain at 1Hz. In terms of oxygen concentrations, the *in vivo* physoxic level for the myocardium is thought to be around 5%, whereas infarcted areas are considered to reach near-zero oxygen concentrations very quickly (seconds or minutes). We employed the described microdevice to flow a N₂ gas mixture in the conditioning channel, thus providing a hypoxic stimulus to cells. We exploited quick re-oxygenation dynamics to explore reperfusion conditions on culture cells. The microdevice was employed with a base ambient oxygen level corresponding to physoxia (5% O₂) in order to precisely model the oxygen dynamics in healthy and ischemic myocardium. In this way, three oxygen concentration dynamics were reproduced: a static incubation at 5% O₂ (physoxia, PX) for 24h, an abrupt reduction of oxygen concentration to about 1% O₂ that is maintained for 24h (hypoxia, HX), and the same reduction to 1% O₂ that is maintained for 12h and re-oxygenated to 5% O₂ for other 12h (reperfusion, REP).

Mechanical Strain Oxygen dynamics

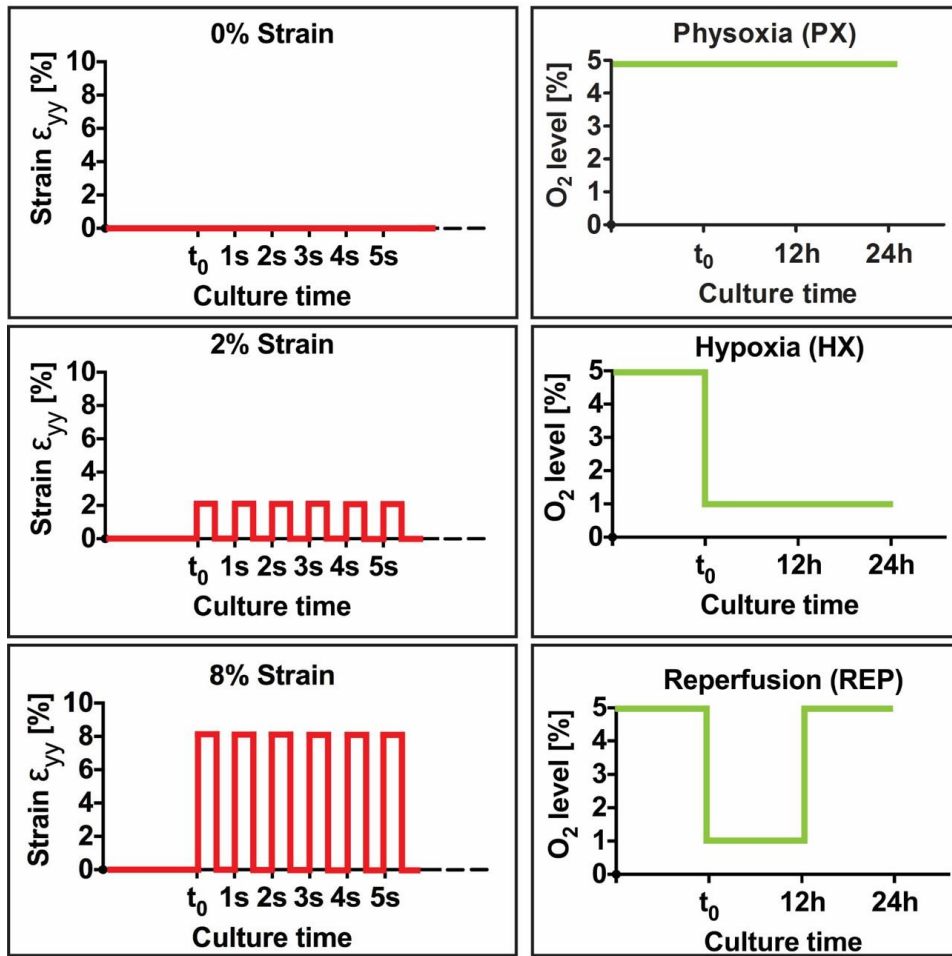


Figure 3.3 – Representative graphs of the stimulation parameters applied in the present work. After a static pre-incubation at physoxic levels to allow for CFs adhesion to the membrane, patterns of mechanical and oxygen stimulations were started at t_0 . Graphs on the left show three different mechanical strain stimulations (red curves): a static control at 0% strain (top), cyclic strain applied at 1Hz and 2% intensity (center) and cyclic strain applied at 1Hz at 8% intensity (bottom). These stimulation parameters were combined with oxygen dynamics represented in the graphs on the right (green curves): a static incubation at myocardium physoxic levels (PX, 5% O₂), an abrupt reduction of O₂ levels at t_0 to about 1% representing acute hypoxia (HX, 1% O₂) and the same hypoxic insult maintained for 12h and followed by a re-oxygenation (reperfusion, REP). All stimulations were stopped at 24h and CFs were fixed for analyses.

Biological data presented in this Chapter refers to all possible combinations of the two stimulations with the exception of the reperfusion condition that was combined with 0% strain and 8% strain only.

Figure 3.4 shows the stimulation system employed in the present work. Microdevices were actuated by a vacuum line and a gas line. Programmable electromechanical valves modulated the vacuum to switch at 1Hz from atmospheric

pressure to the desired vacuum pressure (namely -200mmHg for 2% strain and -600 mmHg for 8% strain). A flowrate of humidified gas mixture (95% N₂ 5% CO₂) was regulated with a flowmeter and delivered to the microdevices through low-permeability gas tubing.

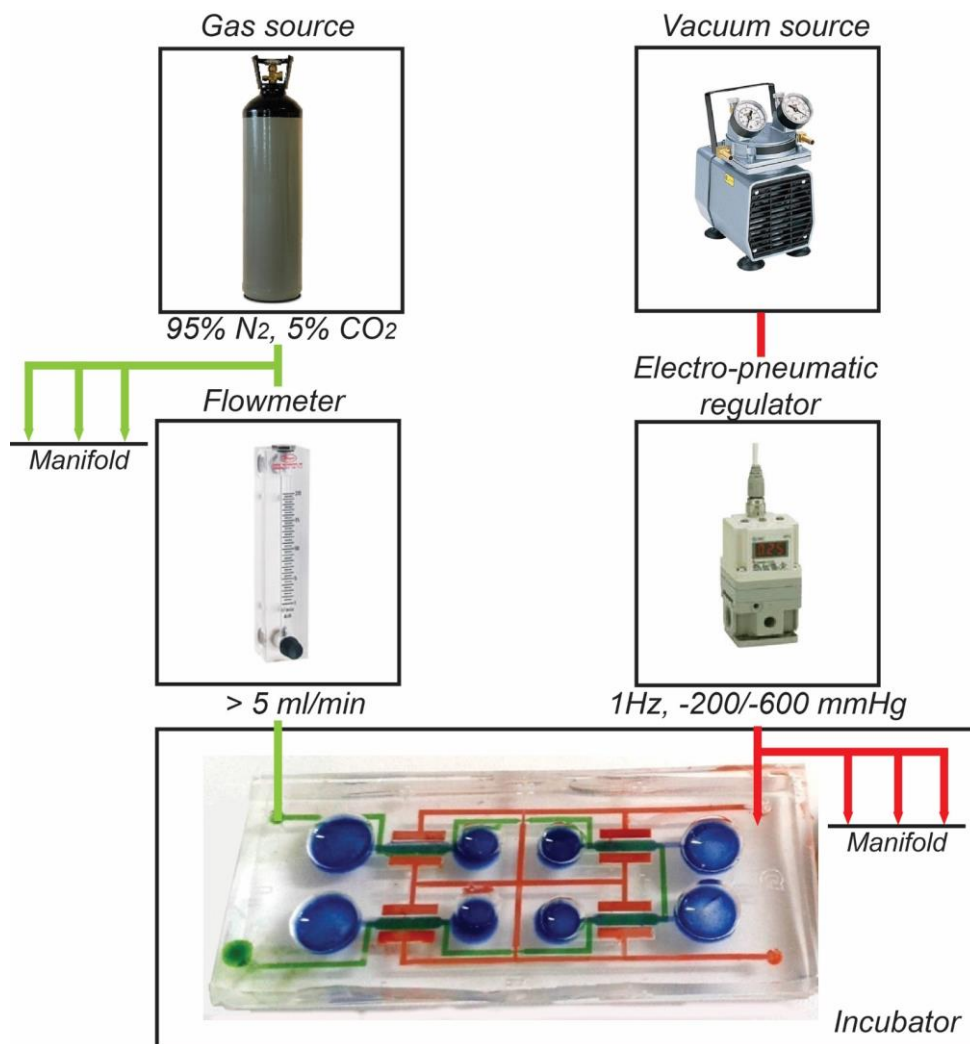


Figure 3.4 – Control system setup employed to operate the multi-stimulus microdevice. Green lines represent oxygen control line: the gas source (95% N₂, 5% CO₂) is connected to flowmeters to regulate the flowrate to the desired value and deliver the gas to the microdevice gas inlet. The lower fluidic channel (green) then flows below all four culture chambers (blue). Red lines represent vacuum actuation line. A vacuum source is connected to an electro-pneumatic regulator that adjusts the vacuum pressure to the desired value (-200 mmHg for 2% strain and -600 mmHg for 8% strain) and switches at 1Hz between vacuum and atmospheric pressure. The vacuum is then connected to one or multiple microdevices at the corresponding vacuum inlet. The actuation circuit (red) delivers vacuum pressure to all four stretching units to generate membrane strain

3.2.5 Cell culture

Normal Human Ventricular Cardiac Fibroblasts were purchased from Lonza (Lonza Bioscience, Singapore). Cells were cultured in FGM-3 medium (Lonza Bioscience, Singapore) and in a humidified incubator at 90% N₂, 5% O₂, 5% CO₂ at all times unless otherwise indicated. Microdevices were autoclave-sterilized, plasma-treated and coated with human fibronectin (Sigma-Aldrich, Singapore) for 30 minutes at room temperature. Cells were seeded for experiments at a passage number of four. After pre-loading each culture chamber of the microdevices with 80µl of medium, 20µl of cell suspension (10⁶ cells/ml) were manually injected, allowing cells to adhere to the culture membrane for 12h. Subsequently – being this initial time point referred to as t₀ – the stimulation was started.

3.2.6 Immunofluorescence

Cells were fixed with 4% paraformaldehyde in PBS for 10 minutes. After 15min of permeabilization with PBS containing 0.5% Triton-X, cells were blocked for 1h at room temperature with 3% bovine serum albumin. Cells were then probed overnight at 4°C with the following primary antibodies: anti-phospho-Histone-H3 (Ser10, rabbit, Santa-Cruz, US), for mitotic cells; anti-Collagen1 (mouse, AbCam, UK), to identify intracellular production of collagen. The following secondary antibodies were used for 2h at room temperature: goat anti-mouse Alexa Fluore 488 and goat anti-rabbit Alexa Fluor 564. Nuclear staining was performed by incubating cells with DAPI. Negative controls were present for all immunofluorescence stainings.

3.2.7 Image processing and analysis

Images were acquired with a Zeiss 710 Confocal microscope. Imaging parameters were not changed during the acquisition of the entire experiments. For quantitative analyses of immunofluorescence markers, three images per culture chamber were taken at 10X magnification, thus sampling roughly half of the total area of the culture membrane. Images were acquired from the central region of the culture membrane. Cell proliferation analyses were performed by manually counting nuclei positive for PHH3 and dividing by the total number of nuclei (automatically counted) to estimate the level of expression. Intracellular collagen I analyses were performed by manually counting cells that exhibited a bright perinuclear staining and dividing by the total number of nuclei (automatically counted) to estimate the level of expression. About 500 cells per replicate were screened for proliferation and collagen I analyses. Both analyses were conducted on a minimum number of 4 experimental replicates.

3.2.8 Statistical analyses

All data are presented as mean \pm SD. Statistical comparisons were performed using GraphPad 5 (Prism) software. Where appropriate, two-way ANOVA tests followed by Bonferroni post-hoc tests were applied in order to determine statistical significance of differences and evaluate synergistic or separate contribution of mechanical strain stimulation and oxygen levels alterations. Two-way ANOVA tests not only determined significance of differences within groups, but also the significant impact of an entire group on the results (e.g. the hypoxic condition generally affects the given marker) and the interaction factor denoting synergy of the two stimuli in affecting the results (e.g. the application of simultaneous stimulation has a greater effect than the two separate stimulations). A p-value lesser than 0.05 was considered significant.

3.3 Results

3.3.1 Numerical simulations

After validation of the numerical model with experimental measurements of oxygen levels present on the culture membrane in a defined standard condition, numerical simulations were employed to predict the distribution of oxygen tension across the 2D geometrical model in three operating conditions of the microdevice and in two different ambient oxygen levels (normoxia and physoxia). Based on these results, an estimate of the oxygen level sensed by cells seeded on the culture membrane was obtained, by assessing the oxygen tension values close to the cell culture membrane and its uniformity along the width of the culture channel.

Figure 3.5 shows 2D color maps of oxygen tension along the cross-section of the microdevice in three operating conditions and two different ambient oxygen tension (21% O₂, 159 mmHg, normoxia; 5% O₂, 38 mmHg, physoxia). Such distributions suggest that the oxygen tension value applied to the lower conditioning chamber represents the major contribution to the oxygen level of the culture membrane. Indeed, with the exception of border effects near the culture chamber walls, the vicinities of the culture membrane exhibit oxygen tension values comparable to the lower conditioning chamber with a good uniformity along the membrane width throughout all the simulated settings: three operating conditions and two ambient oxygen levels.

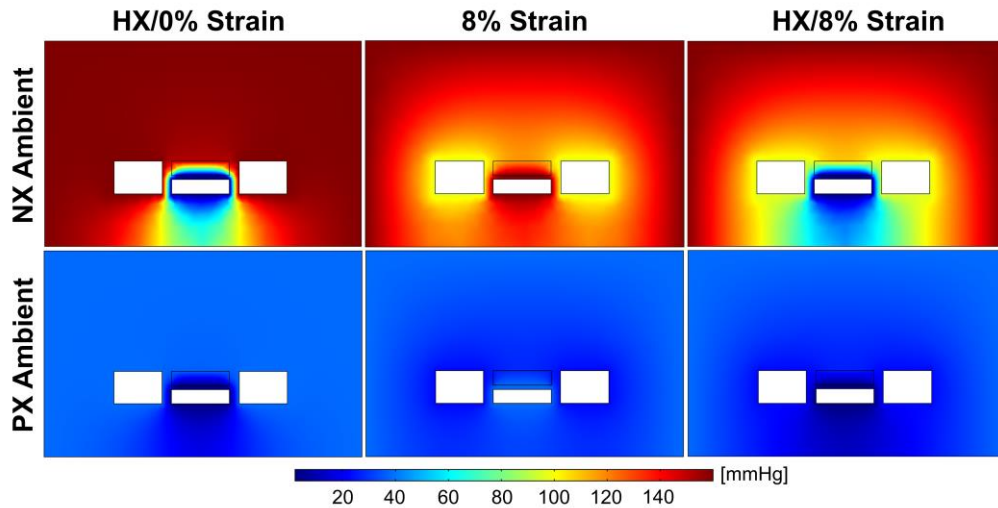


Figure 3.5 – 2D color maps of estimated distributions of oxygen tension in different operating conditions of the microdevice and different ambient oxygen levels. In HX/0% Strain condition (left) the lower fluidic chamber is set at 2 mmHg (Hypoxia pO_2) to simulate a constant flow of N_2 gas and the side channel are set at ambient pO_2 since no vacuum is applied; in 8% Strain condition (center) the lower fluidic chamber is set at Ambient pO_2 as the channel is left open to the surrounding atmosphere and the side channels are set at appropriate average values (Strain pO_2) to simulate cyclic application of vacuum pressure; in HX/8% Strain condition (right) both stimulations are operating: the lower fluidic chamber is set at 2mmHg and the side chambers are set at Strain pO_2 . In the top row a normoxic environment is simulated whereas in the bottom row a physoxic environment is simulated. In all operating conditions and in all ambient environments, the culture membrane is uniformly conditioned by the pO_2 present in the lower conditioning chamber

A more detailed analysis of oxygen tension values achieved in the culture region was conducted by plotting pO_2 values estimated in the vicinities of the membrane along its width (1200 μ m) (Figure 3.6).

pO₂ along membrane width

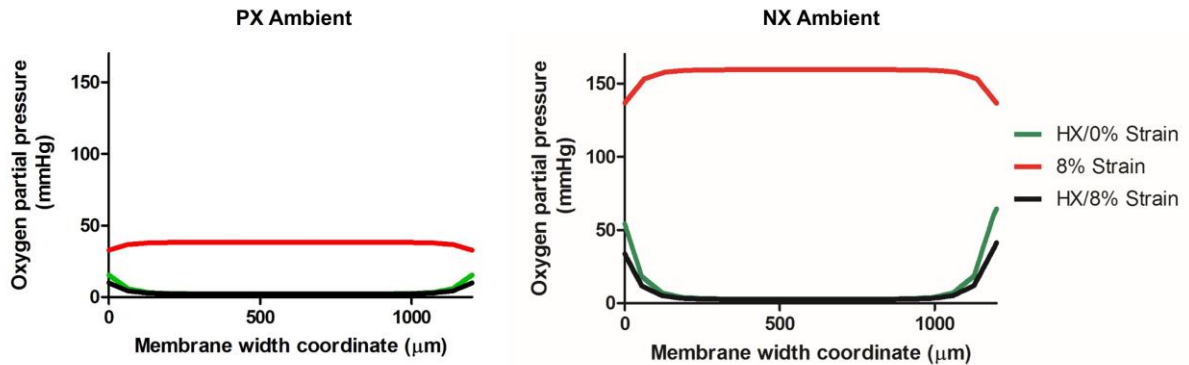


Figure 3.6 – Estimated pO₂ values along culture membrane width in all three microdevice operating conditions and with two different simulated environments: normoxic ambient (21%, 159 mmHg) and physoxic ambient (5%, 38 mmHg). In all cases the culture membrane exhibits uniform pO₂ values comparable to the pO₂ applied in the lower conditioning chamber. Border effects are present near channel walls.

Oxygen tension values on the culture membrane are comparable to the values applied in the conditioning channel: with an applied oxygen tension in the conditioning chamber of 2 mmHg (0,3% O₂), the culture membrane exhibits values of 7±1 mmHg (about 1% O₂) averaged throughout the two hypoxic conditions. On the other hand, when the conditioning channel is left open to the ambient oxygen levels, the oxygen tension values on the culture membrane are identical to the applied oxygen tension in the lower conditioning chamber. In terms of uniformity, despite evident border effects near channel walls, oxygen tension values are, for about 80% of the membrane, within a range of ± 1 mmHg of the plateau value. This defines a uniform stimulation region of about 900μm (out of 1200μm) along the membrane width. This region was taken into account, together with the uniformity requirements dictated by strain field analyses in Chapter 2, when acquiring images of stimulated cells.

Taken together, results obtained from numerical simulations show that the lower fluidic channel may act as a conditioning layer for the above culture membrane. Indeed, estimated pO₂ values on the culture membrane are tightly related to the pO₂ values

imposed in the lower chamber boundaries in all operating conditions of the device and in two different ambient oxygen levels (normoxia and physoxia). This demonstrated that the microdevice can be employed in simultaneous or individual stimulation without affecting the uniformity of the stimulus. In addition, the device can be effectively used at different environmental oxygen levels, enabling experiments with a base oxygen level set at physoxic (5% O₂) or normoxic (21% O₂) levels. A non-negligible border effect is present near the culture chamber walls, however, most of the culture membrane width results within acceptable ranges of the obtained plateau values.

3.3.2 Microdevice characterization

Oxygen concentrations values were experimentally measured by means of a needle-based oxygen sensor in order to demonstrate the functionality of the conditioning channel and characterize equilibrium values and equilibration time-constants. Experimental measurements of steady state O₂ concentrations in the proximity of the culture membrane were recorded considering two varying parameters: increasing N₂ gas mixture flowrate in the conditioning channel (5, 15, 50 ml/min) to investigate the dependency of oxygen levels from gas flowrate; chamber position with respect to N₂ gas flow path to investigate buildup of oxygen in the common conditioning channel and in the four culture chambers of a microdevice. Figure 3.7A shows measured membrane O₂ concentrations versus chamber position at varying flowrates. The lower conditioning channel is able to condition the culture chambers at flowrates as low as 5 ml/min. In fact, little significant difference is reported when increasing flowrates, with average O₂ membrane concentrations values ranging from 1.1% O₂ (at 50 ml/min) to 1.4% O₂ (at 5 ml/min), denoting the dominant contribution of diffusive over convective transport through the thin PDMS membrane. Considering

O₂ membrane concentrations values with respect to the chamber position in the gas flow path, no significant difference is reported between chamber positions at any flowrate.

The application of controlled oxygen dynamics in culture platforms is fundamental in several *in vitro* experimental investigations. In order to explore cellular behaviors under precise temporal changes in oxygen concentrations, we characterized the deoxygenation dynamics occurring when the N₂ gas flowrate is applied in the lower fluidic channel. In addition, while the microdevice is suitable to two different re-oxygenation strategies (flow of a different gas mixture in the lower conditioning channel or interruption of the N₂ gas flowrate), we characterized re-oxygenation occurring after the N₂ gas flowrate in the lower fluidic channel was stopped. Figure 3.7B shows both deoxygenation and re-oxygenation dynamics occurring in four representative culture chambers. With an average time-constant of 8 ± 2 s, flow-induced deoxygenation abruptly switches oxygen levels sensed by cultured cells from normoxia to acute hypoxia. Given the reduced chamber sizes and the PDMS high gas-permeability, re-oxygenation also occurs in short times ($\tau = 4.4 \pm 1.0$ min) making the microdevice a controlled tool for the study of cardiac reperfusion injury or the application of brief hypoxic stimuli for studying cardiac ischemic-preconditioning.

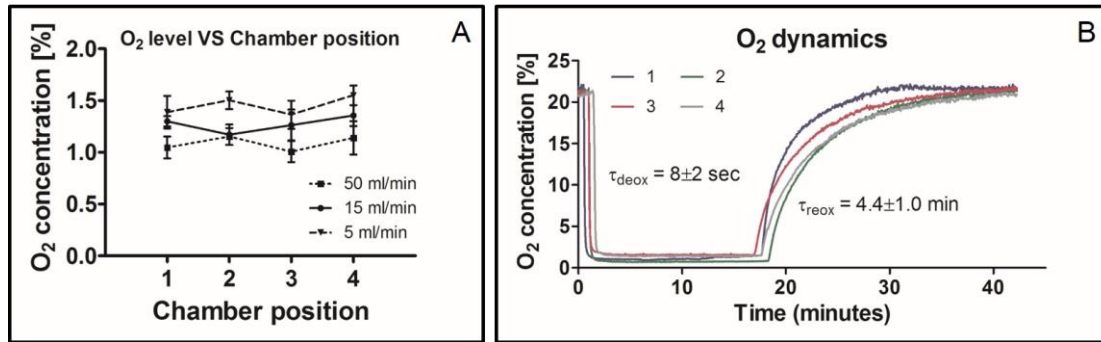


Figure 3.7 – A) O₂ concentration values experimentally measured in all four culture chambers within a group of four different microdevices ($n=4$ in each chamber position) at varying N₂ gas flowrates (5, 15, 50 ml/min). The culture membranes reach values of about 1-1.5% with non-significant impact of chamber position and with little influence of increasing flowrates (average O₂ membrane concentration value at 50 ml/min is significantly different from the average value at 5 ml/min, Kruskal-Wallis test with Dunn's post hoc comparison, $p<0.05$). B) Four representative recordings of O₂ concentrations measured in each chamber position showing the immediate deoxygenation upon application of a N₂ flowrate of 15 ml/min and the rapid re-oxygenation after the N₂ gas flowrate was stopped.

3.3.3 CFs proliferation under combined stimulation

CFs increased proliferation is a key factor in the onset and progression of cardiac fibrotic response after ischemic injury. We previously reported in Chapter 2 the modulation of CFs proliferation under different mechanical strain intensities¹¹¹. We here employed the microdevice to investigate combined effects of O₂ levels alterations and mechanical strain on the proliferative response of CFs. We probed cells with anti-PHH3 immunofluorescent antibodies to highlight cells in the mitotic phase. Figure 3.8 shows the trends of mitotic cells after 12h and 24h of individual or combined stimulations. The statistical analysis was performed with a Two-way ANOVA test and selected significant differences are highlighted in Figure 3.8.

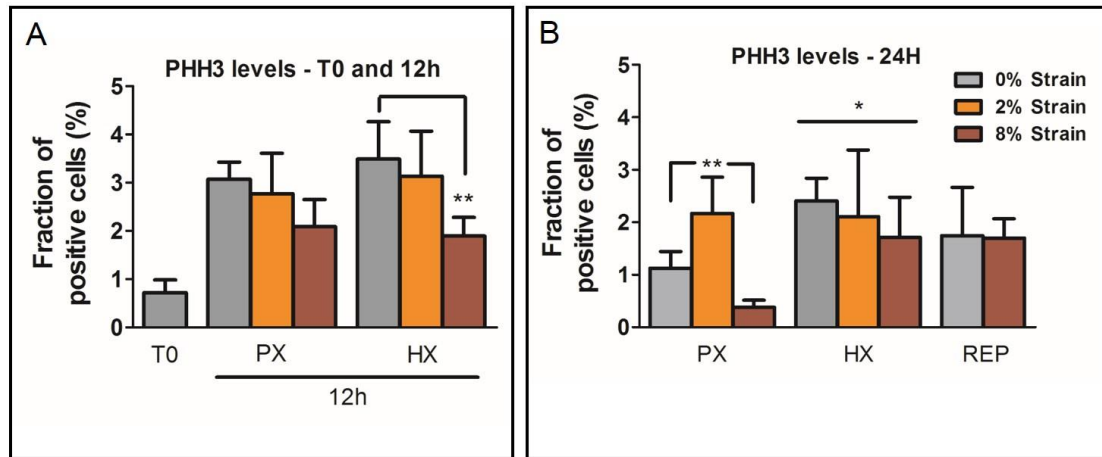


Figure 3.8 – Fraction of cells positive for PHH3 (cell mitosis) at *t0* and after 12h (Panel A) and after 24h (Panel B) of stimulation. Data are grouped by oxygen dynamics and colored bars indicate the mechanical strain condition: grey bars indicate 0% strain condition, orange bars indicate 2% strain condition, red bars indicate 8% strain condition. PX indicates constant incubation at physoxic levels, HX indicates abrupt hypoxic condition and REP indicates reperfusion stimulation. Selected significant differences of Two-way ANOVA tests are highlighted (* = $p < 0.05$; ** = $p < 0.01$). Lines covering an entire group refer to the group significant impact on the results

The effect of hypoxia (1% O₂) on cell proliferation is not significant in the earliest phase of stimulation (12h, Figure 3.8A). The hypoxic stimulus appears as a positive regulator of cell proliferation after 24h of stimulus (Grouped p-value lesser than 0.05, Figure 3.8B). On the other hand, mechanical strain exhibits strain-dependent effects: after 24h of stimulus, only 2% strain significantly increases the number of mitotic cells. In the short term (12h), however, 8% strain induces a negative regulation of mitosis in both hypoxia and physoxia groups. These results are in line with our previous investigation on freshly-isolated human CFs where 2% strain was reported to cause a potent proliferation increase and 8% strain a proliferative response comparable to controls¹¹¹. Cells challenged with a reperfusion stimulus interestingly show upregulated levels of PHH3 at 24h, comparable to those of the hypoxia group. Interaction p-value resulted non-significant, meaning that hypoxia and mechanical strain independently regulate CFs proliferation.

3.3.4 Intracellular collagen I production under combined stimulation

Upon cardiac injury CFs remodel and heal the tissue by forming a collagen-based scar. The distinctive ECM protein involved in this process and secreted by CFs during pathological conditions is type-I collagen. We investigated the effects of combined cyclic mechanical strain and oxygen levels alterations on the intracellular staining for collagen I. When cultured *in vitro*, CFs normally exhibit a faint cytoplasmic collagen I staining. Figure 3.9 shows representative images of CFs stained for collagen I after 24h of combined mechanical stimulation and oxygen dynamics. We report that, under specific stimuli, CFs show a bright perinuclear staining together with dotted cytoplasmic staining (Figure 3.9). This staining is compatible with an accumulation of collagen I or pro-collagen I in the endoplasmic reticulum and in intracellular vesicles¹²⁴. The difference between faint cytoplasmic staining and bright perinuclear staining was sharp enough to perform quantitative analyses by manual counts of collagen I-positive cells.

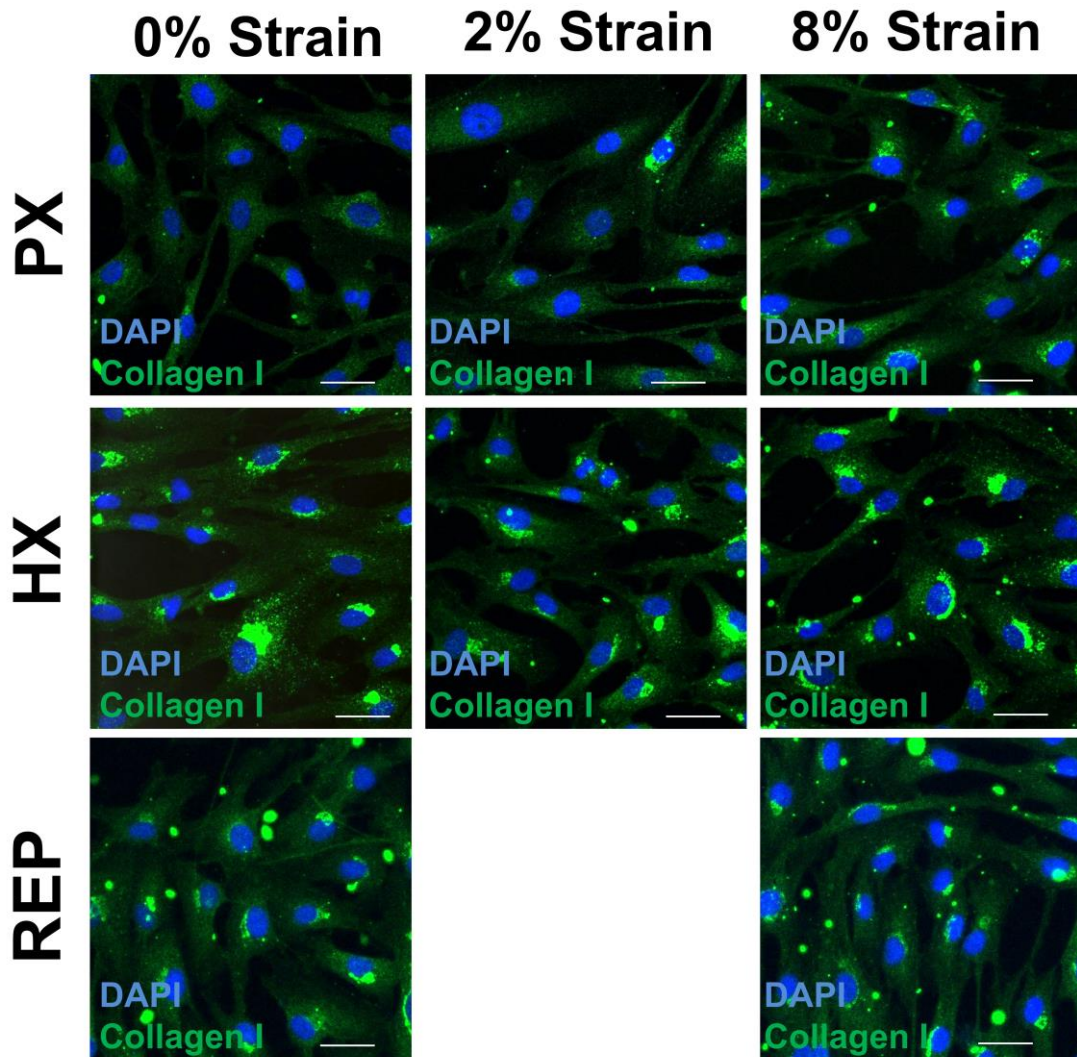


Figure 3.9 – Representative images of CFs fixed after 24h of culture under combined mechanical strain (columns) and oxygen levels alterations (rows) conditions. Nuclei are stained with DAPI (blue) whereas collagen I is labeled in green. CFs cultured at hypoxic conditions (HX, 1% O₂) exhibit a bright perinuclear collagen I staining whereas a faint cytoplasmic staining is present in CFs cultured at physoxia (PX, 5% O₂).

Quantitative analyses showed in Figure 3.10 reveal that hypoxia induces a dramatic intracellular accumulation of collagen I: independently of the time-point (12h or 24h), almost all cultured cells that were exposed to hypoxic conditions exhibited an intracellular accumulation of collagen I, whereas a significantly smaller fraction of cells exhibited this staining at physoxia. Mechanical strain plays a different role into the cellular response: CFs presented a strong collagen I response only after 24h of 8% cyclic strain, whereas no significant changes are generated by a stimulation at a lower

intensity (2% strain). Interestingly, two-way ANOVA analyses report interaction p-values statistically significant at both 12h ($p < 0.05$) and 24h ($p < 0.001$), meaning that the combined stimulation affects the results more than the two individual stimulations. CFs undergoing the reperfusion stimulation also displayed a strong accumulation of intracellular collagen I when cultured under cyclic 8% strain, whereas static CFs cultures undergoing reperfusion exhibited at 24h a much lower fraction of collagen-I-positive cells, suggesting that the hypoxia-induced accumulation of collagen may be reversible once the oxygen conditions are restored.

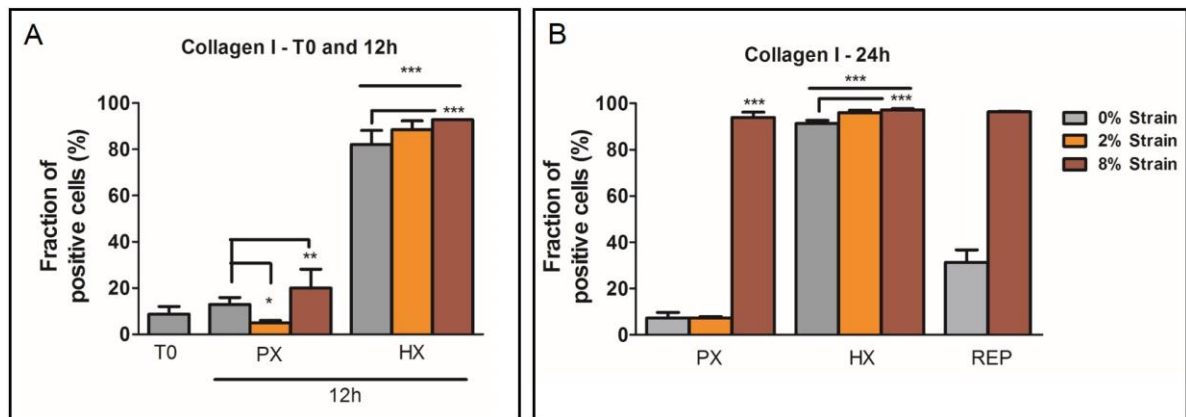


Figure 3.10 – Fraction of cells positive for collagen I perinuclear bright staining (accumulation of intracellular collagen I) at t0 and after 12h (Panel A) and after 24h (Panel B) of stimulation. Data are grouped by oxygen dynamics and colored bars indicate the mechanical strain condition: grey bars indicate 0% strain condition, orange bars indicate 2% strain condition, red bars indicate 8% strain condition. PX indicates constant incubation at physoxic levels, HX indicates abrupt hypoxic condition and REP indicates reperfusion stimulation. Selected significant differences of Two-way ANOVA tests are highlighted (* = $p < 0.05$; ** = $p < 0.01$, *** = $p < 0.001$). Lines covering an entire group refer to the group significant impact on the results.

3.4 Discussion

Microfabricated platforms for cell culture under complex stimulation conditions have recently drawn the attention of researchers as promising tools for unraveling cellular behaviors through the recapitulation of *in vivo* environments. The ability to

perform controlled stimulation with multiple environmental factors is paramount to achieve a high similarity between *in vitro* culture platforms and physiological microenvironments. While several approaches to engineer cardiac environments have been described and a relevant number of studies on cardiac cells subjected to environmental cues (mechanical stimulation, acute hypoxia, electrical stimulation) have been conducted^{48,107,108,111,112,114,117}, current literature lacks studies aimed at combining multiple physico-chemical stimuli to elucidate their relative contributions and attempt an improved mimicking of the *in vivo* environment. Both mechanical stimulation and changes in tissue oxygen concentrations are indeed dominant environmental factors especially in cardiac pathology. Myocardial ischemia occurs upon clogging of coronary arteries causing cardiac cells to sense an abrupt reduction of oxygen concentrations from physoxic (5% O₂) to hypoxic levels (below 1% O₂). Subsequent tissue damage is healed by CFs that activate, differentiate, proliferate and deposit new ECM. Studies of CFs response upon different environmental factors have led to significant advancements both in the understanding of cellular mechanisms related to physiological and pathological remodeling, with the ultimate goal of controlling tissue remodeling and avoiding common adverse remodeling effects occurring after myocardial infarction and ischemia^{47,103}.

In this work, we characterized the use of a microdevice for combined application of cyclic mechanical strain and fine control of oxygen dynamics. In Chapter 2, the design and fabrication of the present microdevice was presented as a platform for applying cyclic uniaxial mechanical strain and conducting studies on CFs behavior under different strain intensities. Employing microfluidics to control oxygen dynamics has recently proved to be a promising approach. Indeed, the reduced sizes, the use of gas-permeable polymers and controlled micro-geometries enable the precise control of

rapid gas exchange phenomena, an ability that is currently not practicable with standard culture systems and standard oxygen incubators. The peculiarities of oxygen control with microfluidics were previously employed to apply complex temporal changes in micron-sized devices in order to model relevant cardiac pathological conditions^{116,125} (e.g., ischemia/reperfusion injury). We here performed preliminary numerical simulations and experimental measurements of oxygen concentration values on the device culture membrane in order to characterize the functioning of a lower fluidic channel flowing below the thin PDMS culture membrane as an oxygen-conditioning compartment. This evaluation demonstrated that the stretching unit layout is suitable to be effectively employed in two simultaneous or independent operating conditions: control of culture membrane oxygen concentration with induction of abrupt hypoxic conditions potentially followed by reperfusion; application of uniform cyclic membrane strain.

Numerical simulations demonstrated the uniformity of the oxygen levels on the culture membrane in different operating conditions and that oxygen alterations can be applied starting from different ambient oxygen levels (physoxic, in oxygen-controlled incubators; normoxic, in standard ambient air incubators). Experimental measurements of oxygen concentrations on the culture membrane defined an equilibrium value of about 1% O₂ in all four culture chambers when N₂ gas was flowed in the lower channel at flowrates as low as 5 ml/min. Time constants of deoxygenation (applied flowrate) and re-oxygenation (stopped flowrate) steps were respectively of the order of seconds and minutes, making the present device a candidate for applying controlled complex oxygen dynamics (eg: abrupt hypoxia, reperfusion, cycles of ischemia/reperfusion) relevant to cardiac injury research. We then performed experiments of combined mechanical stimulation (0% strain, 2% strain and 8% strain) and oxygen levels

alterations (maintained physoxia, PX; abrupt hypoxia, HX; ischemia/reperfusion dynamics, REP) applied to cultures of human CFs. We analysed the response of CFs to this complex patterns of stimuli in terms of cell proliferation (immunofluorescence for PHH3, staining mitotic cells) and intracellular collagen I production and we unraveled the synergistic or independent contributions of the two environmental stimuli.

The hypoxic insult proved to be a positive regulator of cell proliferation, with CFs expressing significantly higher levels of PHH3. On the other hand, mechanical strain plays a complex role in cellular regulation of proliferation. Lower regimes of strain (2% strain) cause a significant proliferation increase in CFs cultured at physoxic levels, whereas higher strain intensities (8% strain) do not induce this response and, in turn, are able to negatively regulate the hypoxia-induced proliferation. The proliferative arrest in mechanically stimulated cells (8% strain) may be correlated to other cellular behaviors, as suggested by analyses of collagen I production. Indeed, an intense intracellular accumulation of collagen I is reported when cells are subject to the hypoxic insult, with mechanical strain playing a minor role into this response. However, after 24h of 8% strain stimulation a similar high accumulation of collagen I is reported. CFs subject to reperfusion dynamics exhibited distinct responses: after experiencing the hypoxic insult and then returning to physoxic levels, CFs were still expressing moderately high levels of PHH3, whereas collagen I levels returned to control values (except when 8% strain stimulation was applied). This suggests that CFs *in vitro* responses to hypoxia may be partially or fully reversible when the environment returns to physoxic levels.

In summary, we interpreted hypoxia as a stronger regulator of CFs behavior if compared to mechanical strain: indeed the hypoxic stimulus was able to simultaneously induce both an up-regulation of proliferation and an accumulation of collagen I in CFs

cytoplasm. When oxygen levels return to physoxia, CFs may realistically readjust to their original expression pattern, demonstrating the dynamic ability of CFs to adapt to environment changes. Mechanical strain seems to induce a complex impact on CFs behavior, possibly denoting a feedback between proliferative responses and production of ECM molecules: 2% strain caused an increased proliferation without accumulation of collagen I, whereas 8% strain caused a high accumulation of collagen I together with low values of proliferation markers. These results pave the way to a broader understanding of CFs behavior in complex microenvironments resembling pathological myocardial conditions and for the first time unravel the contributions of mechanical strain and oxygen changes on the modulation of physiologically relevant CFs behavior.

3.5 Conclusions

We here described a novel microdevice-based strategy to perform cell cultures under simultaneously controlled mechanical strain and oxygen dynamics. Employing a previously described layout, tailored to mechanical strain application, we demonstrated that a lower channel can be effectively used to condition an upper culture chamber with rapid changes in oxygen concentrations. Numerical simulations and experimental characterizations described and assessed the operating conditions of the microdevice, thus yielding a controlled platform for multi-stimulus and multi-chamber cell culture investigations. We explored CFs response to combined or independent mechanical stimulation and oxygen dynamics and we described the effects induced on CFs proliferation and intracellular collagen I accumulation. Multi-stimulus experiments revealed hypoxia as a stronger regulator of CFs proliferation and collagen I production, whereas mechanical strain induced either a significant proliferative increase (under 2% strain intensity) or an intense accumulation of intracellular collagen I (8% strain). We

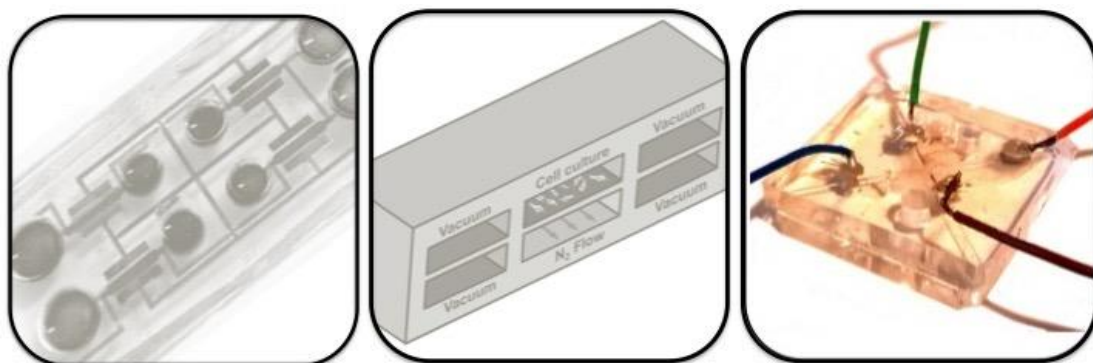
also provided insights into CFs response to reperfusion dynamics: the hypoxia-induced accumulation of collagen I may be reversible once CFs return to physoxia (unless cells are constantly subject to 8% strain) whereas CFs appear to maintain a higher proliferation level upon reperfusion conditions (independently of the mechanical stimulus applied).

4.

A micron-scale model of transport through the blood-brain barrier

Biological experiments described in this chapter were carried out at *Nanomedicine Lab*, Istituto Neurologico Carlo Besta, Milan (ITALY) and at *Dept. of Health Sciences*, University of Milano-Bicocca, Monza (ITALY)

This chapter partially refers to a manuscript in preparation. As such, it contains preliminary data that may be revised for publication.



Rationale

Effective delivery of drug treatments for central nervous system disorders is particularly challenging due to a reduced permeability of brain capillaries to small molecules, a distinctive feature widely known as the blood-brain barrier. As a consequence, pharmaceutical research is in constant search of vectors and drug formulations capable of crossing the blood-brain barrier and effectively target brain diseases. To this aim, study of in vitro models is vital for successful and smart drug development. The advent of microfabricated platforms opened up new prospects and innovative solutions in the field of modeling in vitro physiological barriers. In this chapter, the design and development of a multi-layer microplatform for modeling the blood-brain barrier is described. Required specifications such as possibility of forming an endothelial barrier, analyzing transported and blocked molecules, estimation of barrier electrical resistance are included. Two different layouts are presented and the fabrication of multi-layer devices including an upper PDMS layer for cell culture, a porous polycarbonate membrane and a lower PDMS layer for transported molecules collection is described together with the incorporation of enclosed electrodes for monitoring endothelial layer resistance. Murine endothelial brain cells are then seeded and the platform is validated with a transport assay of 40kDa dextran. Preliminary results here described are showing that effective barrier formation takes place, demonstrating functionality of the device as a BBB model. In addition, electrical resistance measurements shine light on the feasibility of an on-chip electrical detection of barrier formation. These outcomes are encouraging for future optimization of electrodes measuring system and application of this strategy in relevant drug transport studies.

4.1 Introduction

4.1.1 The Blood-Brain Barrier

The Blood Brain Barrier (BBB) is a functional biological structure of the Central Nervous System (CNS) that separates the vascular compartment of the brain from the cerebral parenchyma. Peripheral blood vessels or capillaries normally exchange nutrients and small molecules with the surrounding tissue; however, in the CNS, endothelial cells forming the capillary walls exhibit tighter junctions between each other yielding to an overall reduced permeability to small molecules. This tighter endothelium does not exhibit fenestrations and the transport through the capillary walls is almost completely regulated by intra-cellular transport mechanisms. This peculiar endothelial junctions and the interactions in the outer capillary region with other cell types such as astrocytes and pericytes are unique features of the CNS peripheral vessels and constitute what is referred to as BBB¹²⁶.

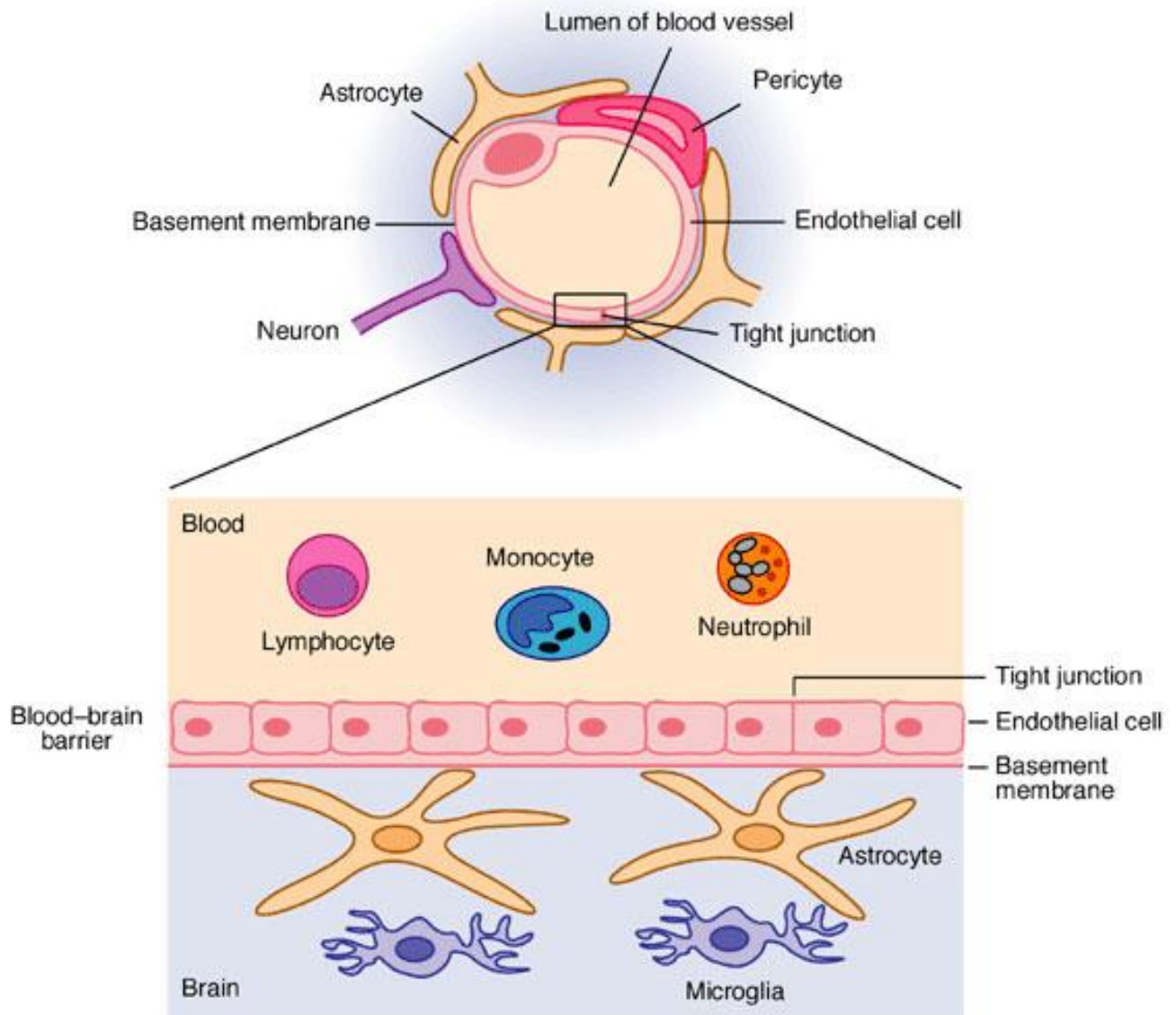


Figure 4.1 – Cross section (top) and lateral view (bottom) of the blood-brain barrier interface in brain vessels. The BBB separates blood flow from brain tissue through a complex interaction of cellular actors (endothelial cells, astrocytes, pericytes) and structural elements (tight junctions, basement membrane)

Figure 4.1 shows a sketch of a cerebral capillary highlighting the main actors involved in the neurovascular unit and responsible for barrier formation and maintenance: endothelial cells (ECs) forming tight junctions; basal lamina constituted by extra-cellular matrix proteins such as laminin and collagen¹²⁷; astrocytes that secrete factors contributing to BBB integrity¹²⁸; pericytes that regulate both cerebral and non-cerebral capillaries.

4.1.2 Current Central Nervous System diseases and treatments

CNS infectious diseases are known to represent a severe threat to the organism mainly due to the limited regenerative potential of brain tissue and the limited immune response therein. The BBB represents an efficient protection from CNS infections: indeed, intra-cellular transport mechanisms are typically able to allow transport of only selected nutrient molecules (such as sugars and basic amino acids), preventing the passage into the brain of complex molecules and potentially harmful organisms.

This barrier function, however, has the drawback of unselectively blocking the transport of small molecules to the brain, which in turns also prevents pharmacological treatments of several CNS pathologies^{129,130}. The two strict requirements for a small molecule to permeate through the BBB are:

- Molecular mass of lower than 500 Da
- High lipophilicity

However, the first requirement seems to be the leading factor, with the impact of lipophilicity decreasing exponentially as the molecular mass increases¹²⁹. As a consequence, most drug molecules are ruled out of these parameters. Data from the Comprehensive Medicinal Chemistry database (CMC) shows that only 5% of the total number of current approved drugs is able to target the CNS¹³¹. In this scenario, the available drugs aimed at the CNS are able to treat only four CNS disorders: depression, schizophrenia, pain and epilepsy. Major CNS disorders such as Parkinson's disease, Alzheimer's disease, Huntington's disease or multiple sclerosis currently lack a pharmacological treatment aimed at the CNS. New generation drugs such as monoclonal antibodies, gene therapies or recombinant proteins also involve large molecules with little hope to cross the BBB.

4.1.3 *In vitro* modeling of the Blood-Brain Barrier

Current research approaching the lack of drug carriers targeting the BBB covers diverse fields from chemical engineering to cell biology. One particular aim of this multi-disciplinary investigation is the development of *in vitro* BBB models as screening tools for candidate drugs and carriers. The standard approach for *in vitro* transport studies through the BBB is the use of Transwell culture platforms: a porous membrane is inserted on top of a standard well plate, and functions as cell culture substrate. This simple design makes it possible to access two culture chambers: the upper well, where cells are seeded, and the lower well, below seeded cells. When cells reach confluence and fully cover the porous membrane, the molecular transport from upper to lower well occurs only by means of trans-cellular transport. At this stage, therefore, studies can be carried out and candidate drugs or carriers can be collected – and their amount evaluated – in the lower well with different techniques (e.g. radioactivity or light absorbance).

This two-chamber model currently represents the standard culture system for BBB transport studies and has the advantage of being easily coupled to standard laboratory culture wells. The main disadvantages of this approach include the relatively high volumes required (hundreds of microliters to more than 1ml depending on the insert size), cost and reduced optical visibility of the cells cultured on the porous membrane. Indeed, a quantitative method to estimate the formation of the barrier is required and studies cannot rely on the visual assessment of cell confluence on the membrane. Hence, the electric resistance offered by the cell monolayer (Trans Endothelial Electric Resistance, TEER) is the most commonly used parameter to estimate the membrane cell coverage. The typical TEER measurement system is composed of a “chopstick” fixed pair of electrodes that fits in both compartments of the Transwell culture system.

The fast rise of microfabrication technology enabled advancements also in the field of *in vitro* BBB models. Indeed, the use of micron-scale geometry has the advantage of reducing amounts of cells, reagents, and candidate drug formulations. In the specific case of candidate drugs transport studies, using micron-scale devices and reduced volumes not only reduces the needed amount of candidate drug, but also increases the solute-to-volume ratio in the detection of transported candidate molecules, thus improving the resolution of the detection process.

To date, a few examples of micron-scale culture systems for BBB studies are present in literature. The main microfluidic strategies to perform drug transport studies are:

- Trapping of cells into vertical micro-holes or posts to enable barrier formation and subsequent evaluation of molecules transported through the holes/posts in a collection channel^{132–134}
- 3D tubular micro-structures resembling native blood vessels^{135,136}.
- Arrangement of porous membranes sandwiched between PDMS channels to perform standard 2D cell cultures and collect transported molecules in a lower collection chamber^{31,137,138}.

This last group of devices has been increasingly employed in recent research because of a higher similarity with standard 2D *in vitro* systems. In this chapter, the development and testing of a microfluidic device as an *in vitro* model of the BBB is described. Design specifics were sketched according to the current needs and limitations of standard *in vitro* BBB models. Subsequently, two geometries were drawn and fabricated with standard microfabrication procedures. After characterizing the

functional elements, the devices were tested with brain endothelial murine cells to assess barrier formation in the *in vitro* microsystem.

4.2 Materials and Methods

4.2.1 Design requirements

The main design requirements of an *in vitro* model of BBB are:

1. Ability to assess molecules transport through the BBB
2. Reduced size to minimize amounts of cells and reagents
3. TEER measurement capability, through biocompatible electrodes to estimate barrier formation in real-time

With regard to point 1, we aimed at designing a multi-layer device due to its suitability for molecular transport studies: we opted for including a porous membrane within two PDMS layers, defining upper and bottom chambers. Due to technical challenges in fabricating microporous PDMS membranes, a commercial polycarbonate (PC) membrane was chosen due to its limited cost and ease of use. To this aim we implemented a non-standard bonding technique to assemble PC membrane with PDMS layers.

As regards to point 2, a target device working volume of 30 μ l was chosen, roughly one order of magnitude lower than the smallest Transwell system.

As for the TEER monitoring, a four-point measurement system was designed (point 3), consisting in two pairs of electrodes. The electrode material was chosen according to the electrode function. The pair of electrodes devoted to carry electrical current are required to be highly polarizable so that no charge is actually transferred across solution and electrodes; platinum (Pt) was chosen as material for perfectly

polarizable current electrodes. On the other hand, voltage measuring electrodes are required to be non-polarizable and allow free charge movement between electrode and solution in order to maintain a near-zero potential. Silver/Silver chloride (Ag/AgCl) electrodes were employed for voltage measuring electrodes. Both Pt and Ag/AgCl electrodes are known to be highly biocompatible. We opted for designing a four-point measurement system in order to easily connect the electrodes to a commercial voltohmmeter routinely used to monitor TEER in standard cell cultures.

4.2.2 Microdevice design

Two separate device geometries were conceived: one where the membrane is sandwiched between two parallel channels and one where the membrane is sandwiched between two orthogonal channels. Both device configurations (orthogonal and parallel) comprised a top and bottom PDMS layer. An annotated top view of the two device geometries is shown in Figure 4.2 where top (red) and bottom (blue) layers are overlapped. The green area represents the porous PC membrane. A list of geometric parameters is shown in Table 4.1.

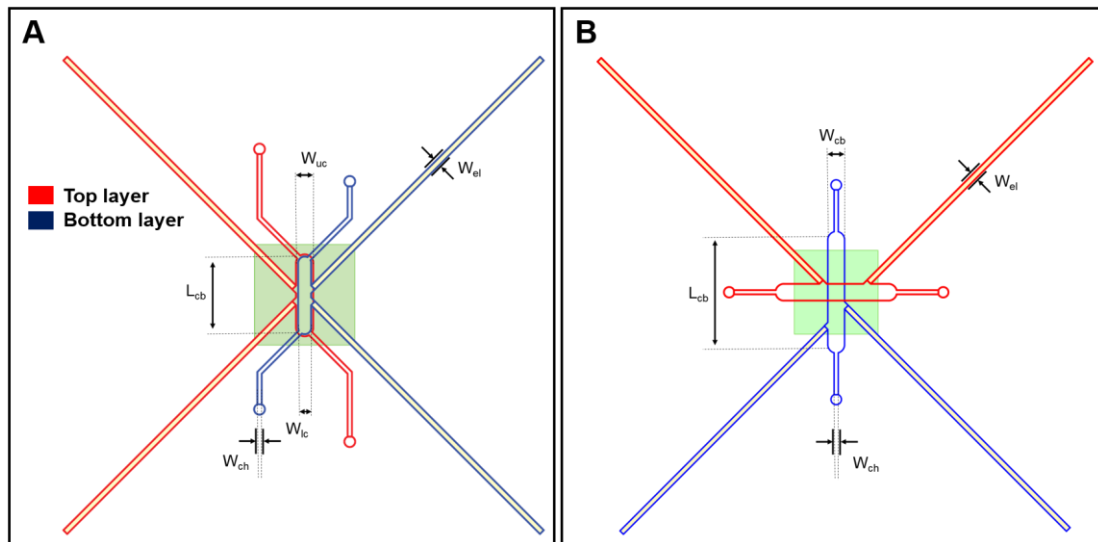


Figure 4.2 – Top views of parallel-chambers (A) and orthogonal-chambers (B) geometries. Top (red) and bottom (blue) layers are overlapped to show final device configuration. PC membrane is represented in green. Relevant geometric parameters are annotated and listed in Table 4.1

	Orthogonal geometry	Parallel geometry
W_{ch} (inlet/outlet channel width)	200 μ m	200 μ m
W_{cb} (Chamber width)	800 μ m	
W_{uc} (Upper chamber width)		800 μ m
W_{lc} (Lower chamber width)		600 μ m
W_{el} (Electrode channel width)	270 μ m	270 μ m
H_{ch} (Chamber and channels height)	150 μ m	150 μ m
H_{el} (Electrode channels height)	270 μ m	270 μ m
L_{cb} (Chamber length)	5mm	3mm

Table 4.1 – List of relevant geometric parameters of inlet/outlet channels, chambers and electrode channels for both microdevice geometries (orthogonal chamber arrangement and parallel chamber arrangement)

In both geometries, dedicated channels to host electrodes of 250 μ m diameter were included. In particular, one current carrying electrode was positioned in the upper layer and another in the lower layer to apply direct current through the culture membrane; voltage sensing electrodes were positioned analogously. Each layer therefore contained one voltage electrode and one current electrode. In the culture

region, distances between voltage sensing electrodes were reduced to minimize undesirable electric resistances of culture medium contained in the microchannels. The height of the culture chamber (150 μm) was kept smaller than that of electrode channels (270 μm); this choice guarantees the electrodes to abut on a well-defined confinement spot, while still allowing their contact with the culture medium to ensure conductivity.

In the parallel geometry, the width of the upper chamber is slightly larger than the width of the lower chamber. This is to avoid transport in a region where cell monolayer border effects may occur (e.g.: non-integrity near the walls that may cause leaky monolayers). The parallel configuration features a transport region of about 1.8 mm^2 , while the orthogonal one a sensibly smaller transport region of about 0.6 mm^2 located at the crossing between the two chambers.

Four layer geometries were subsequently drawn through CAD software (AutoCAD, AutoDesk Inc.) and printed at high-resolution (32000dpi) in order to be used as photomasks in the master mold fabrication steps. In order to fabricate devices with different heights, two masks were printed per each layer one including features to be printed with a height of 150 μm and one including features with 270 μm height

4.2.3 Master molds fabrication

Master molds fabrication was performed through standard soft-lithography techniques: a layer of SU-8 pre-polymer was spin-coated on a clean silicon wafer to obtain a height of 150 μm . After soft-baking, the first mask was aligned and the wafer was exposed to UV light. After hard-baking, another layer of SU-8 pre-polymer was spin-coated on top of the previous layer in order to reach a total height of 270 μm . After soft-baking, the second mask was carefully aligned with the previous layer and the wafer was exposed to UV light. After a final hard-baking step the wafer was developed leaving the designed features in relief.

4.2.4 PDMS layers fabrication

Top and bottom layers of the microdevices were realized through PDMS replica molding on the corresponding molds. PDMS was mixed at a 10:1 polymer to curing agent ratio and poured on the silicon wafers used as molds. After curing for 2h at 65°C, layers were peeled off the molds and the upper layer was punched to create channel inlet and outlet wells. An inlet/outlet well diameter of 4mm was used for both devices geometries. The upper layer was also punched in correspondence of all four electrodes channels in order to create connections with external instrumentation for TEER measurement. To this aim, wells with a diameter of 2mm were created at a distance of about 1cm from the culture chamber. Porous PC membranes with a pore size of 3µm and 10µm thickness were purchased from Sigma (Whatman Cyclopore, Sigma-Aldrich, Milan, Italy). In order to fit the microdevices chambers, the membranes were cut into small squares of about 5mm².

4.2.5 Electrodes fabrication

Silver and platinum wires with a diameter of 250µm were purchased from Sigma (Sigma-Aldrich, Milan, Italy). Platinum electrodes were fabricated by manually cutting the wire into short rods of about 1mm length. Ag/AgCl electrodes were fabricated by cutting silver rods of about 1cm length and depositing a thin layer of silver-chloride by means of an electrodeposition technique. Briefly, silver wires were immersed in a 1M HCl bath and connected to the positive end of a power source. A platinum counter electrode of same diameter and length was also immersed in the same bath and connected to the negative end of the power source. A constant current density of 1 µA/cm² was applied to the system for 15 minutes to obtain a uniform coating of AgCl on the silver wires.

4.2.6 Microdevice assembly

The microdevices consisted of four functional components: an upper PDMS layer; a porous PC membrane; Pt and Ag/AgCl electrodes; a lower PDMS layer. The device assembly was performed via toluene-PDMS stamp-and-stick bonding. This bonding technique employs a thin PDMS film as glue to stamp the upper and lower microdevice layers when the glue is still liquid. Once the layers are stamped in the glue, they are brought into contact and the glue is allowed to polymerize in order to stick the layer together. To obtain the glue film, PDMS was spin-coated on a flat silicon wafer at high speed; toluene was also employed as an organic solvent to dilute PDMS, thus obtaining very thin glue layers that did not alter the channels geometries during stamping¹³⁹.

Device assembly was therefore performed as follows: curing agent, base PDMS and toluene (Sigma-Aldrich, Milan, Italy) were mixed in a 1:10:15 ratio and spin-coated onto a clean silicon wafer to obtain a glue thickness of about 3 μ m. Layers were stamped with glue for 30s and then lifted off. At this stage, the electrodes were manually inserted into the electrodes channels matching the connection wells. The PC membrane was gently pressed on the top stamped layer until completely adhered to the PDMS. The lower layer was then carefully aligned under a stereomicroscope and brought into contact with the upper layer and PC membrane complex. The assembled microdevices were incubated at room temperature overnight to allow glue curing and then baked at 120°C for 2h to allow complete evaporation of toluene. Electrodes were then connected to electrical colored wires by means of a conductive epoxy resin (RS Components, Milan, Italy) poured in the connection wells.

4.2.7 Cell culture

Microdevices were sterilized in ethanol overnight and coated with human fibronectin prior to cell seeding (25 µg/ml, 30 minutes incubation). Br-Bend5 murine endothelial brain cells were used at a cell suspension density of 5×10^6 cells/ml. After pre-loading both upper and lower layers with 30µl of warm culture medium (10% FBS in DMEM), 10µl of cell suspension were injected in the upper channel to perform cell seeding. Cells were allowed to adhere to the membrane for 4h before adding additional 100µl of culture medium. Control conditions were kept as devices filled only by culture medium and without cells. Culture medium was refreshed every 24h. TEER values were recorded every 24h by connecting the four electrodes to an EVOM voltohmmeter (WPI Instruments, Germany) via a custom-made RJ-10 connector.

4.2.8 Dextran permeability assay

After 5 days of culture, the transport of fluorescent dextran through the monolayer was evaluated. Medium was aspirated from all four inlet/outlet wells of the device. FITC-labeled 40kDa dextran was diluted to a concentration of 1 mg/ml in culture medium. 30µl of FITC-Dextran solution were injected in the upper layer whereas 30µl of culture medium alone were injected in the lower layer. Fluorescent images were taken at 10 minutes and 60 minutes after injection under an epi-fluorescence microscope. Only devices with orthogonal geometries were employed for this analyses since lower and upper chambers are not completely overlapped and dextran fluorescence could be easily attributed to the upper or lower layer.

4.2.9 Immunofluorescence

After 5 days of culture cells were fixed with 4% paraformaldehyde and immunofluorescence was performed to assess endothelial tight-junction markers expression. After blocking and permeabilization for 1h with 0.2% Triton-X in 3% BSA in PBS, cells were probed with appropriate primary/secondary antibodies solutions against Claudin and V-Cadherin.

4.3 Results and Discussion

4.3.1 Microfabrication

The optimized fabrication protocol yielded functional and robust microdevices. No leaking between layers was observed despite the non-standard bonding technique, including the embedding of thick electrodes and a PC membrane. Previously described multi-layer microdevices for modeling BBB formation included complex electrodes fabrication steps such as sputtering of silver on glass substrates¹³⁷. The electrical recording system here described is fabricated by means of physical rod-shaped electrodes easily included in the multi-layer structure during assembly. Unlike previously described microdevices¹³⁸, both geometries allow the insertion and use of electrodes without impeding membrane observation (i.e. without placing electrodes directly on top of the region of interest). With contrast to standard *in vitro* BBB models, the microdevices here developed require limited amounts of medium, cells and reagents volumes. The total channel volumes are about 2 μ l, while the device filling volume (including reservoir wells) is about 30 μ l.

4.3.2 Permeability assay

Figure 4.3 shows representative fluorescence images taken after 10 minutes and 60 minutes of injection of FITC-labeled 40kDa-Dextran into control devices and devices seeded with Br-Bend5 murine endothelial brain cells. Control devices allow free diffusion of dextran molecules into the lower chamber, as evidenced by the increase of green fluorescence intensity in the bottom orthogonal channel. On the other hand, no fluorescence intensity in the lower channels is observed in devices seeded with Br-Bend5 cells. This outcome confirms the formation of a monolayer that hinders molecular transport from upper layer to lower layer and the working condition of the microdevice here developed.

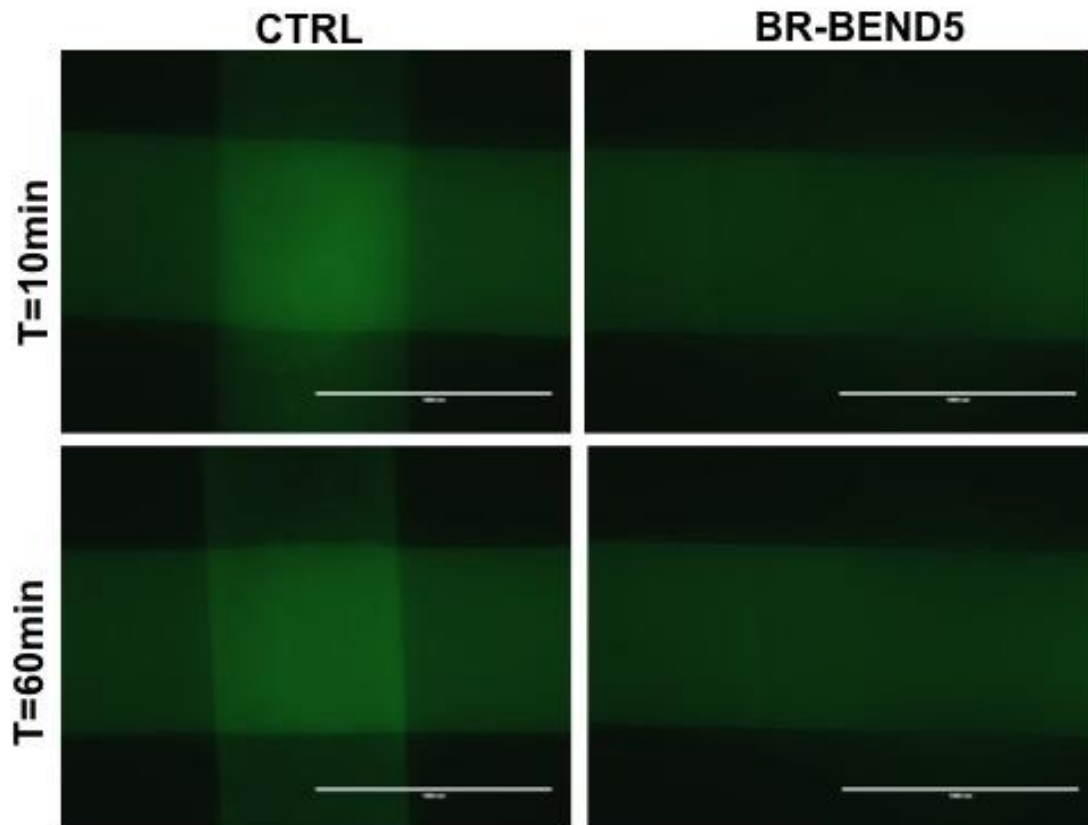


Figure 4.3 – FITC-40kDa-Dextran-based permeability assay. Images show the fluorescence signal of dextran injected in the orthogonal-chambers microdevices after 10 or 60 minutes both in 5 days control devices and in devices cultured for 5 days with Br-Bend5 cells. Absence of fluorescence signal in the lower chambers of microdevices seeded with cells demonstrate the formation of a tight monolayer and the functionality of the microdevices as barrier model

4.3.3 TEER recordings

Figure 4.4 shows TEER values obtained during a 4 days culture experiments. While no evidences of electrode damage or electrode cytotoxicity appeared during the experiments, demonstrating feasibility of the approach, TEER recordings show two main issues: the data resulted highly variable and an increase in TEER values due to the cell monolayer with respect to control devices is only slightly noticeable; several over-range values were recorded during the experiments (when the voltage values recorded by the voltohmmeter exceeds the maximum) that were not reported in the dataset. While the former could be considered a disadvantage present also in standard *in vitro* TEER recordings inside Transwell systems, the latter probably demonstrates the unsuitability of commercial voltohmmeters (specifically tailored to Transwell

systems) to micron-scale devices where narrow channels increase electrical resistances seen by the electrodes.

This is in line with recent communications underlining the difficulties of translating the TEER measurement system from macro-scale to micro-scale platforms

140

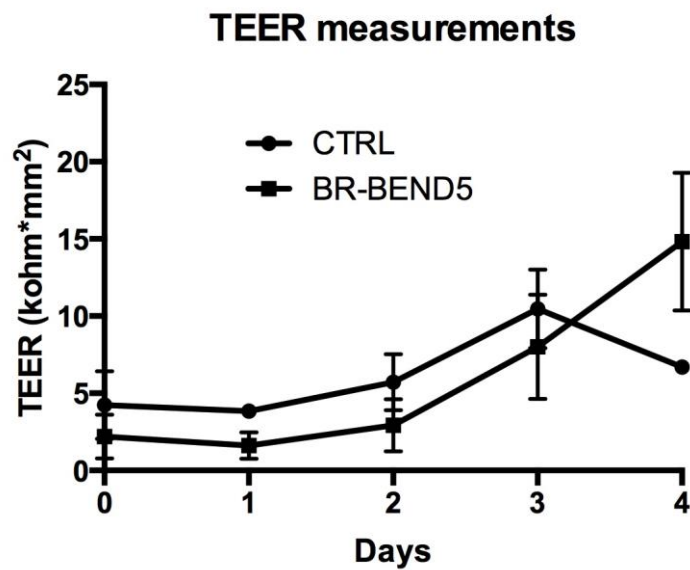


Figure 4.4 – Plot of TEER values against culture time in control devices and in device seeded with Br-Bend5 cells. Despite high deviations, an increasing trend is found in seeded devices. Values represent mean±SD; n=3 except single replicate values due to over/range recordings.

4.3.4 Immunofluorescence

Cells cultured for 5 days in the microdevices were probed for immunofluorescent markers of endothelial tight junction formation. V-Cadherins regulate cell-cell adhesion and formation of junctions with reduced permeability, whereas Claudin has been more closely related to tight-junction formation in the BBB. Cells resulted positive for a uniform distribution of Claudin and V-Cadherin, with a specific membrane location in V-Cadherin stainings (Figure 4.5). This further demonstrates the ability of cells to produce tight monolayers in the microdevice.

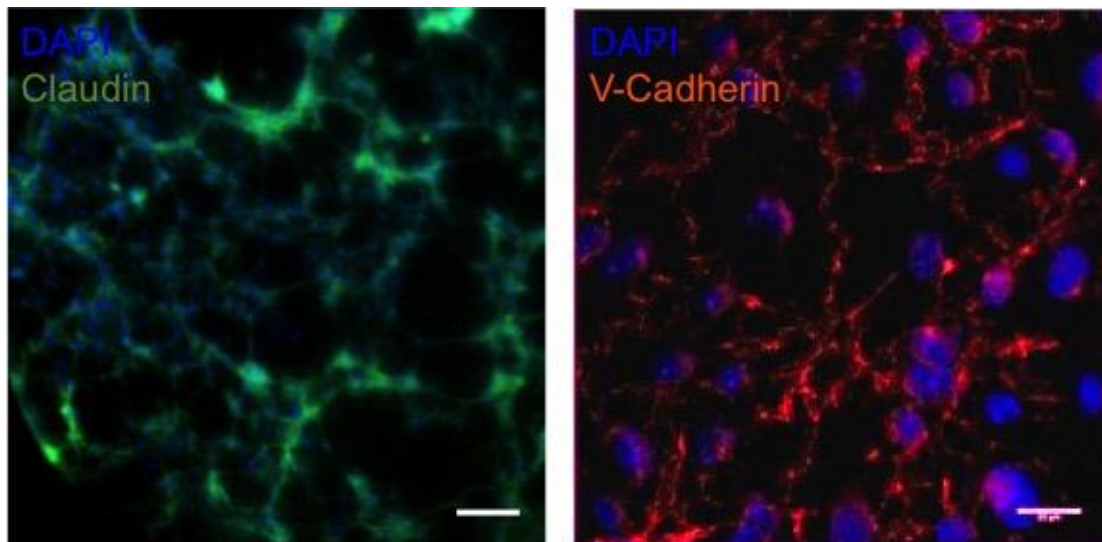


Figure 4.5 – Immunofluorescent images of Br-Bend5 after 5 days of culture in microdevices. Left panel shows Claudin (green, tight-junctions) and DAPI (blue, nuclei) stainings. Scale bar=100 μ m. Right panel shows V-Cadherin (red, cell-cell junctions) and DAPI (blue, nuclei) stainings. Scale bar=50 μ m. Expression of both V-Cadherin and Claudin demonstrate the presence of molecular machinery involved in tight-junction and barrier formation.

4.4 Conclusions

This chapter described the design, development and preliminary validation of a microdevice for the *in vitro* modeling of the BBB. The device design was dictated by requirements such as small volumes and ability to perform transport studies and monitor TEER. By employing multi-layer PDMS microfabrication it was possible to assemble a layout with upper culture chamber, porous culture membrane, lower collection chamber and side electrodes. The functionality of two alternative geometries was then tested by seeding murine brain endothelial cells. The devices resulted highly biocompatible with viable cells cultured up to 5 days. Cells were also able to form tight monolayers as showed by the expression of V-Cadherin and Claudin. Functionality of the microdevice layout was demonstrated by performing permeability assays that demonstrated that the barrier function is optimally modeled in the microdevices. In terms of TEER monitoring, the technical solution envisioned to include side electrodes

resulted functional and biocompatible. An optimization of electrical resistance recordings is however necessary to obtain a clear electrical monitoring of cells monolayer formation. These preliminary results serve as a crucial basis for further studies aimed at performing in-depth permeability assays with biologically relevant drug carrier formulations.

General conclusions and achievements of the thesis

The emergence of organs-on-chips and the optimization of microfabrication technologies to biomedical and biological frameworks has recently set new ambitious goals and research lines aimed at improving our knowledge and handling of biological materials (particularly at the cellular scale) *ex vivo*. Following the increasing exploitation of *in vitro* research for speeding up clinical, pharmaceutical and basic research screenings, organs-on-chips entered this scenario by proving capable of recapitulating organ- and tissue-level functions in specifically tailored cell culture microenvironments. This novel family of microdevices accomplished an important milestone in the last decade: organs-on-chip research proved that cell culture experiments can be carried out in controlled microplatforms where physical and chemical stimuli are precisely coordinated to replicate *in vivo* conditions and that these novel tools generated data, results and knowledge that was not otherwise attainable.

With the increasing number of publications, dedicated journals, successful stories covered by non-specialized media, government funding and laboratories adopting the technology, the use of organs-on-chips seem to be approaching a peak of expectations. Failure to cope with these often inflated expectations is a common development of an innovation life cycle and sliding into disillusionment, media disinterest and lack of funding is a potential outcome of technological research. In order to become a widespread reality, transferred to standard pharmaceutical and biological research, organs-on-chips need to face the main issues that limit the translation to a product. Indeed commercial viability of organs-on-chips is still to be proven.

Ease of use and accessibility of protocols by non-specialized operators is one of the key aspect and major limitation that has to be taken into account: fabrication of organs-on-chips still requires technical skills and machinery that dramatically hinder

both the in-house manufacture by biological end-user and the automation of the fabrication processes; in addition, organs-on-chip itself are often coupled and operated with the use of non-standard laboratory techniques (syringes for injection, pumps for constant perfusion, etc.).

Microfabricated platforms are also currently limited by a reduced biological readout potential: thanks to the optical transparency of PDMS, most of the biological analyses carried out on organs-on-chips are imaging-based leaving behind gene and protein expression analyses due to the reduced amounts of cultured cells.

The present PhD thesis described the design, development, characterization and application of three microdevice-based approaches to mimic tissue-level environments in physiology and pathology. With the common technical motif of being multi-layer microdevices, assembled by stacking multiple layers of microstructured PDMS, these newly characterized organs-on-chips were developed by taking into account current limitations.

The microplatform described in Chapter 2 and 3 is based on a design first proposed by a pivotal work in microfluidics. By simply increasing channel sizes, the platform here proposed can be employed by non-specialized users with standard laboratory pipettes and a standard laboratory vacuum line, rather than with syringe pumps for loading and culture procedures. This solution, together with a higher throughput due to the multi-chamber design and a high control on the amount of strain applied makes the cell stretching microdevice much more appealing to biologists. While still being limited by a low number of cells for gene and protein expression analyses, the microdevice made it possible to perform quick screenings on multiple experimental conditions in a significant number of replicates and to thoroughly describe the responses of human cardiac fibroblasts to increasing strain intensities, with

implications in current knowledge of cardiac fibroblast physiological and pathological behavior under stimulation. For the first time, a cellular control of proliferation that acts according to the amount of sensed mechanical strain was elucidated and described in a recent publication on *Biotechnology and Bioengineering* thanks to the described microdevice.

In Chapter 3, this platform was upgraded to a multi-stimulus configuration and thanks to its versatile and high-throughput nature, it was possible to elucidate the synergistic or independent contributions of combined mechanical stimulation and oxygen deprivation in the early events occurring to cardiac fibroblasts upon myocardial ischemia. From a technical standpoint, the combination of oxygen control and mechanical strain in a dedicated microdevice is a significant advancement. In addition, biological insights were provided into cellular responses (proliferation and collagen production) elicited under combination of stimuli relevant to cardiac pathology. Although not included in the Chapter, on-going work is currently focused on the analyses of supernatants collected from cells, to investigate secreted inflammatory and signaling factors. This further broadens the range of application of the microplatform, adding another relevant biological assay to the readout potential of the microdevice.

Finally, preliminary data described in Chapter 4 demonstrate another opportunity to broaden the application range of organs-on-chips: recreating barrier functions in a multi-layer microdevice allowed transport studies through an endothelial barrier, a relevant readout for potential applications in drug development and pharmaceutical research.

In summary, the multi-disciplinary approach of the present PhD thesis has described new bioengineering approaches aimed at the evaluation of cellular behavior in physiology and pathology.. Foreseen advancements of the new approaches here

presented definitely include a greater biological exploitation of the platforms. The unique capability of, for instance, easily performing highly-controlled multi-stimulus experiments opens up a broad range of biological applications aimed at unraveling the physiology and pathology of cardiac cells (e.g. multi-stimulus investigation of contractile cardiac myocytes response, pharmacological analyses of anti-fibrotic drugs effect on cells experiencing infarct-like conditions, etc). In terms of technological advancements, the current limitations of organs-on-chips have to be kept in mind in order to address further research work towards broadening the readout potential and the appeal of micron-scale cell cultures on organs-on-chips while constantly taking care of the simplicity and scalability of microdevices. Only after achieving these milestones the synergy between micro-engineering and biology will be complete and will effectively lead to a new generation of *in vitro* cell cultures.

References

- 1 M. Matfield, *Nat. Rev. Drug Discov.*, 2002, **1**, 149–152.
- 2 Kshitiz, J. Park, P. Kim, W. Helen, A. J. Engler, A. Levchenko and D.-H. Kim, *Integr. Biol. (Camb)*., 2012, **4**, 1008–18.
- 3 H. Geckil, F. Xu, X. Zhang, S. Moon and U. Demirci, *Nanomedicine (Lond)*., 2010, **5**, 469–484.
- 4 M. W. Tibbitt and K. S. Anseth, *Biotechnol. Bioeng.*, 2009, **103**, 655–663.
- 5 D. E. Discher, P. Janmey and Y.-L. Wang, *Science*, 2005, **310**, 1139–43.
- 6 C. M. Kraning-Rush and C. A. Reinhart-King, *Cell Adh. Migr.*, 2012, **6**, 274–9.
- 7 S. Halldorsson, E. Lucumi, R. Gómez-Sjöberg and R. M. T. Fleming, *Biosens. Bioelectron.*, 2015, **63**, 218–231.
- 8 N. L. Jeon, S. K. W. Dertinger, D. T. Chiu, I. S. Choi, A. D. Stroock and G. M. Whitesides, *Langmuir*, 2000, **16**, 8311–8316.
- 9 S. Chanet and A. C. Martin, *Mechanical force sensing in tissues*, 2014, vol. 126.
- 10 T. Mammoto and D. E. Ingber, *Development*, 2010, **137**, 1407–1420.
- 11 M. Benjamin and B. Hillen, *Eur. J. Morphol.*, 2003, **41**, 3–7.
- 12 J. W. Bjork and R. T. Tranquillo, *Biotechnol. Bioeng.*, 2009, **104**, 1197–206.
- 13 I. Martin, D. Wendt and M. Heberer, *Trends Biotechnol.*, 2004, **22**, 80–6.
- 14 K. Bilodeau and D. Mantovani, *Tissue Eng.*, 2006, **12**, 2367–2383.
- 15 V. Barron, E. Lyons, C. Stenson-Cox, P. E. McHugh and a. Pandit, *Ann. Biomed. Eng.*, 2003, **31**, 1017–1030.
- 16 A. B. Yeatts and J. P. Fisher, *Bone*, 2011, **48**, 171–181.
- 17 Y. Xia and G. M. Whitesides, *Annu. Rev. Mater. Sci.*, 1998, **28**, 153–184.
- 18 G. M. Whitesides, *Nature*, 2006, **442**, 368–373.
- 19 D. Qin, Y. Xia and G. M. Whitesides, *Nat Protoc*, 2010, **5**, 491–502.
- 20 J. C. McDonald and G. M. Whitesides, *Acc. Chem. Res.*, 2002, **35**, 491–499.

- 21 M. a Unger, H. P. Chou, T. Thorsen, a Scherer and S. R. Quake, *Science*, 2000, **288**, 113–116.
- 22 M. Rasponi, F. Piraino, N. Sadr, M. Laganà, A. Redaelli and M. Moretti, *Microfluid. Nanofluidics*, 2011, **10**, 1097–1107.
- 23 A. Pavesi, F. Piraino, G. B. Fiore, K. M. Farino, M. Moretti and M. Rasponi, *Lab Chip*, 2011, **11**, 1593–1595.
- 24 S. N. Bhatia and D. E. Ingber, *Nat. Biotechnol.*, 2014, **32**, 760–772.
- 25 P. J. Lee, P. J. Hung and L. P. Lee, *Biotechnol. Bioeng.*, 2007, **97**, 1340–6.
- 26 P. Occhetta, M. Centola, B. Tonnarelli, A. Redaelli, I. Martin and M. Rasponi, *Sci. Rep.*, 2015, **5**, 10288.
- 27 J. S. Jeon, S. Bersini, M. Gilardi, G. Dubini, J. L. Charest, M. Moretti and R. D. Kamm, *Proc. Natl. Acad. Sci. U. S. A.*, 2015, **112**, 214–9.
- 28 A. M. Taylor, M. Blurton-Jones, S. W. Rhee, D. H. Cribbs, C. W. Cotman and N. L. Jeon, *Nat. Methods*, 2005, **2**, 599–605.
- 29 D. Huh, B. D. Matthews, A. Mammoto, M. Montoya-Zavala, H. Y. Hsin and D. E. Ingber, *Science*, 2010, **328**, 1662–1668.
- 30 H. J. Kim, D. Huh, G. Hamilton and D. E. Ingber, *Lab Chip*, 2012, **12**, 2165–2174.
- 31 Y. Kim, M. E. Lobatto, T. Kawahara, B. Lee Chung, A. J. Mieszawska, B. L. Sanchez-Gaytan, F. Fay, M. L. Senders, C. Calcagno, J. Becraft, M. Tun Saung, R. E. Gordon, E. S. G. Stroes, M. Ma, O. C. Farokhzad, Z. a Fayad, W. J. M. Mulder and R. Langer, *Proc. Natl. Acad. Sci. U. S. A.*, 2014, **111**, 1078–83.
- 32 A. Grosberg, P. W. Alford, M. L. McCain and K. K. Parker, *Lab Chip*, 2011, **11**, 4165–4173.
- 33 A. Pavesi, G. Adriani, M. Rasponi, I. Zervantonakis, G. Fiore and R. Kamm, *Sci. Rep.*, 2015.
- 34 A. Marsano, C. Conficconi, M. Lemme, P. Occhetta, E. Gaudiello, E. Votta, G. Cerino, A. Redaelli and M. Rasponi, *Lab Chip*, 2016, **16**, 599–610.
- 35 T. Yamazaki, I. Komuro and Y. Yazaki, *J. Mol. Cell. Cardiol.*, 1995, **27**, 133–140.

- 36 C. Ruwhof and A. Van Der Laarse, *Cardiovasc. Res.*, 2000, 47, 23–37.
- 37 J. Sadoshima and S. Izumo, *Annu. Rev. Physiol.*, 1997, **59**, 551–571.
- 38 K.-G. Shyu, *Clin. Sci. (Lond)*, 2009, **116**, 377–89.
- 39 M. W. Curtis and B. Russell, *Pflugers Arch. Eur. J. Physiol.*, 2011, 462, 105–117.
- 40 C. A. Souders, S. L. K. Bowers and T. A. Baudino, *Circ. Res.*, 2009, 105, 1164–1176.
- 41 M. Eghbali, *Basic Res. Cardiol.*, 1992, **87 Suppl 2**, 183–189.
- 42 E. M. Zeisberg and R. Kalluri, *Circ. Res.*, 2010, **107**, 1304–1312.
- 43 S. Cosentino, L. Castiglioni, F. Colazzo, E. Nobili, E. Tremoli, P. Rosa, M. P. Abbracchio, L. Sironi and M. Pesce, *J. Cell. Mol. Med.*, 2014.
- 44 K. E. Porter and N. A. Turner, *Pharmacol. Ther.*, 2009, 123, 255–278.
- 45 B. C. Berk, K. Fujiwara and S. Lehoux, *J. Clin. Invest.*, 2007, 117, 568–575.
- 46 G. Krenning, E. M. Zeisberg and R. Kalluri, *J. Cell. Physiol.*, 2010, 225, 631–637.
- 47 D. Fan, A. Takawale, J. Lee and Z. Kassiri, *Fibrogenesis Tissue Repair*, 2012, 5, 15.
- 48 A. K. Schroer and W. D. Merryman, *J. Cell Sci.*, 2015, **128**, 1865–1875.
- 49 J. J. Tomasek, G. Gabbiani, B. Hinz, C. Chaponnier and R. A. Brown, *Nat. Rev. Mol. Cell Biol.*, 2002, **3**, 349–363.
- 50 J. A. Lucas, Y. Zhang, P. Li, K. Gong, A. P. Miller, E. Hassan, F. Hage, D. Xing, B. Wells, S. Oparil and Y.-F. Chen, *Am. J. Physiol. Heart Circ. Physiol.*, 2010, **298**, H424–H432.
- 51 T. Moore-Morris, N. Guimarães-Camboa, I. Banerjee, A. C. Zambon, T. Kisseleva, A. Velayoudon, W. B. Stallcup, Y. Gu, N. D. Dalton, M. Cedenilla, R. Gomez-Amaro, B. Zhou, D. A. Brenner, K. L. Peterson, J. Chen and S. M. Evans, *J. Clin. Invest.*, 2014, **124**, 2921–2934.
- 52 C. J. Watson, D. Phelan, M. Xu, P. Collier, R. Neary, A. Smolenski, M. Ledwidge, K. McDonald and J. Baugh, *Fibrogenesis Tissue Repair*, 2012, 5, 9.
- 53 C. J. Watson, D. Phelan, P. Collier, S. Horgan, N. Glezeva, G. Cooke, M. Xu, M. Ledwidge, K. McDonald and J. A. Baugh, *Connect. Tissue Res.*, 2014, **55**, 248–256.
- 54 A. A. Lee, T. Delhaas, A. D. McCulloch and F. J. Villarreal, *J. Mol. Cell. Cardiol.*,

- 1999, **31**, 1833–43.
- 55 W. Carver, M. L. Nagpal, M. Nachtigal, T. K. Borg and L. Terracio, *Circ. Res.*, 1991, **69**, 116–122.
- 56 G. E. Lindahl, R. C. Chambers, J. Papakrivopoulou, S. J. Dawson, M. C. Jacobsen, J. E. Bishop and G. J. Laurent, *J. Biol. Chem.*, 2002, **277**, 6153–6161.
- 57 V. Gupta and K. J. Grande-Allen, *Cardiovasc. Res.*, 2006, **72**, 375–83.
- 58 D. Mackenna, S. R. Summerour and F. J. Villarreal, 2000, **46**, 257–263.
- 59 C. Ruwhof, A. E. van Wamel, J. M. Egas and A. van der Laarse, *Mol. Cell. Biochem.*, 2000, **208**, 89–98.
- 60 B. Husse, W. Briest, L. Homagk, G. Isenberg and M. Gekle, *Am. J. Physiol. Regul. Integr. Comp. Physiol.*, 2007, **293**, R1898–R1907.
- 61 R. P. Butt and J. E. Bishop, *J. Mol. Cell. Cardiol.*, 1997, **29**, 1141–1151.
- 62 X. D. Liao, X. H. Wang, H. J. Jin, L. Y. Chen and Q. Chen, *Cell Res.*, 2004, **14**, 16–26.
- 63 J. Atance, M. J. Yost and W. Carver, *J. Cell. Physiol.*, 2004, **200**, 377–386.
- 64 A. P. Dalla Costa, C. F. M. Z. Clemente, H. F. Carvalho, J. B. Carvalheira, W. Nadruz and K. G. Franchini, *Cardiovasc. Res.*, 2010, **86**, 421–431.
- 65 J. Garot, D. A. Bluemke, N. F. Osman, C. E. Rochitte, E. R. McVeigh, E. A. Zerhouni, J. L. Prince and J. A. Lima, *Circulation*, 2000, **101**, 981–988.
- 66 J. Gorcsan and H. Tanaka, *J. Am. Coll. Cardiol.*, 2011, **58**, 1401–1413.
- 67 D. Wang, Y. Xie, B. Yuan, J. Xu, P. Gong and X. Jiang, *Integr. Biol. (Camb)*, 2010, **2**, 288–293.
- 68 J. Kreutzer, L. Ikonen, J. Hirvonen, M. Pekkanen-Mattila, K. Aalto-Setälä and P. Kallio, *Med. Eng. Phys.*, 2014, **36**, 496–501.
- 69 J. P. Vande Geest, E. S. Di Martino and D. A. Vorp, *J. Biomech.*, 2004, **37**, 1923–1928.
- 70 A. Colombo, P. A. Cahill and C. Lally, *Proc. Inst. Mech. Eng. H.*, 2008, **222**, 1235–1245.

- 71 Y. Shao, X. Tan, R. Novitski, M. Muqaddam, P. List, L. Williamson, J. Fu and A. P. Liu, *Rev. Sci. Instrum.*, 2013, **84**.
- 72 A. Gerstmair, G. Fois, S. Innerbichler, P. Dietl and E. Felder, *J. Appl. Physiol.*, 2009, **107**, 613–620.
- 73 M. J. Yost, D. Simpson, K. Wrona, S. Ridley, H. J. Ploehn, T. K. Borg and L. Terracio, *Am. J. Physiol. Heart Circ. Physiol.*, 2000, **279**, H3124–H3130.
- 74 L. Huang, P. S. Mathieu and B. P. Helmke, *Ann. Biomed. Eng.*, 2010, **38**, 1728–1740.
- 75 K. Shimizu, A. Shunori, K. Morimoto, M. Hashida and S. Konishi, *Sensors Actuators, B Chem.*, 2011, **156**, 486–493.
- 76 Q. Wang, X. Zhang and Y. Zhao, *J. Micromechanics Microengineering*, 2013, **23**, 015002.
- 77 C. S. Simmons, J. Y. Sim, P. Baechtold, A. Gonzalez, C. Chung, N. Borghi and B. L. Pruitt, *J. Micromechanics Microengineering*, 2011, 21, 054016.
- 78 M. Ao, B. M. Brewer, L. Yang, O. E. Franco Coronel, S. W. Hayward, D. J. Webb and D. Li, *Sci. Rep.*, 2015, **5**.
- 79 Y. Huang, N.-T. Nguyen, K. S. Lok, P. P. F. Lee, M. Su, M. Wu, L. Kocgozlu and B. Ladoux, *Nanomedicine (Lond.)*, 2013, **8**, 543–53.
- 80 D. Tremblay, S. Chagnon-Lessard, M. Mirzaei, A. E. Pelling and M. Godin, *Biotechnol. Lett.*, 2014, **36**, 657–665.
- 81 J. B. Papizan and E. N. Olson, *Circ. Res.*, 2014, 115, 332–334.
- 82 T. Heallen, M. Zhang, J. Wang, M. Bonilla-Claudio, E. Klysik, R. L. Johnson and J. F. Martin, *Science*, 2011, **332**, 458–461.
- 83 M. Xin, Y. Kim, L. B. Sutherland, M. Murakami, X. Qi, J. McAnally, E. R. Porrello, A. I. Mahmoud, W. Tan, J. M. Shelton, J. a Richardson, H. a Sadek, R. Bassel-Duby and E. N. Olson, *Proc. Natl. Acad. Sci. U. S. A.*, 2013, **110**, 13839–44.
- 84 D. Mosqueira, S. Pagliari, K. Uto, M. Ebara, S. Romanazzo, C. Escobedo-Lucea, J. Nakanishi, A. Taniguchi, O. Franzese, P. Di Nardo, M. J. Goumans, E. Traversa, P. Pinto-Do-Ó, T. Aoyagi and G. Forte, *ACS Nano*, 2014, **8**, 2033–2047.

- 85 S. Dupont, L. Morsut, M. Aragona, E. Enzo, S. Giulitti, M. Cordenonsi, F. Zanconato, J. Le Digabel, M. Forcato, S. Bicciato, N. Elvassore and S. Piccolo, *Nature*, 2011, **474**, 179–183.
- 86 M. Aragona, T. Panciera, A. Manfrin, S. Giulitti, F. Michielin, N. Elvassore, S. Dupont and S. Piccolo, *Cell*, 2013, **154**, 1047–1059.
- 87 A. E. Agocha and M. Eghbali-Webb, *Mol. Cell. Biochem.*, 1997, **172**, 195–198.
- 88 M. Neuss, V. Regitz-Zagrosek, A. Hildebrandt and E. Fleck, *Cell Tissue Res*, 1996, **286**, 145–153.
- 89 A. Rossini, A. Zacheo, D. Mocini, P. Totta, A. Facchiano, R. Castoldi, P. Sordini, G. Pompilio, D. Abeni, M. C. Capogrossi and A. Germani, *J. Mol. Cell. Cardiol.*, 2008, **44**, 683–693.
- 90 E. Gambini, G. Pompilio, A. Biondi, F. Alamanni, M. C. Capogrossi, M. Agrifoglio and M. Pesce, *Cardiovasc. Res.*, 2011, **89**, 362–373.
- 91 L. Terracio, B. Miller and T. K. Borg, *In Vitro Cell. Dev. Biol.*, 1988, **24**, 53–58.
- 92 V. Codelia, G. Sun and K. Irvine, *Curr. Biol.*, 2013, 2012–2017.
- 93 V. M. Almaas, K. H. Haugaa, E. H. Strøm, H. Scott, H.-J. Smith, C. P. Dahl, O. R. Geiran, K. Endresen, S. Aakhus, J. P. Amlie and T. Edvardsen, *Heart*, 2014, **100**, 631–8.
- 94 S. Donekal, B. A. Venkatesh, Y. C. Liu, C. Y. Liu, K. Yoneyama, C. O. Wu, M. Nacif, A. S. Gomes, W. G. Hundley, D. A. Bluemke and J. A. C. Lima, *Circ. Cardiovasc. Imaging*, 2014, **7**, 292–302.
- 95 C. Neidlinger-Wilke, E. Grood, L. Claes and R. Brand, *J. Orthop. Res.*, 2002, **20**, 953–956.
- 96 O. Dewald, G. Ren, G. D. Duerr, M. Zoerlein, C. Klemm, C. Gersch, S. Tincey, L. H. Michael, M. L. Entman and N. G. Frangogiannis, *Am. J. Pathol.*, 2004, **164**, 665–677.
- 97 R. G. Thakar, Q. Cheng, S. Patel, J. Chu, M. Nasir, D. Liepmann, K. Komvopoulos and S. Li, *Biophys. J.*, 2009, **96**, 3423–3432.
- 98 P. Roca-Cusachs, J. Alcaraz, R. Sunyer, J. Samitier, R. Farré and D. Navajas, *Biophys.*

- J.*, 2008, **94**, 4984–4995.
- 99 M. Versaevel, T. Grevesse and S. Gabriele, *Nat. Commun.*, 2012, **3**, 671.
- 100 N. G. Frangogiannis, *Nat. Rev. Cardiol.*, 2014, **11**, 255–65.
- 101 G. Heusch, P. Libby, B. Gersh, D. Yellon, M. Böhm, G. Lopaschuk and L. Opie, *Lancet*, 2014, **383**, 1933–43.
- 102 G. Kania, P. Blyszczuk and U. Eriksson, *Trends Cardiovasc. Med.*, 2009, **19**, 247–252.
- 103 F. Roubille, D. Busseuil, N. Merlet, E. Kritikou, E. Rhéaume and J.-C. Tardif, *Expert Rev. Cardiovasc. Ther.*, 2013, **12**, 111–125.
- 104 A. Leask, *Circ. Res.*, 2010, **106**, 1675–1680.
- 105 A. V Shinde and N. G. Frangogiannis, *J. Mol. Cell. Cardiol.*, 2014, **70**, 74–82.
- 106 A. J. Edgley, H. Krum and D. J. Kelly, *Cardiovasc. Ther.*, 2012, **30**, 30–40.
- 107 P. J. Lijnen, V. V Petrov and R. H. Fagard, *Mol. Genet. Metab.*, 2000, **71**, 418–35.
- 108 V. V Petrov, R. H. Fagard and P. J. Lijnen, *Hypertension*, 2002, **39**, 258–263.
- 109 M. Tamamori, H. Ito, M. Hiroe, F. Marumo and R. I. Hata, *Cell Biol. Int.*, 1997, **21**, 175–180.
- 110 R. M. Clancy, P. Zheng, M. O’Mahony, P. Izmirly, J. Zavadil, L. Gardner and J. P. Buyon, *Arthritis Rheum.*, 2007, **56**, 4120–4131.
- 111 G. S. Ugolini, M. Rasponi, A. Pavesi, R. Santoro, R. Kamm, G. B. Fiore, M. Pesce and M. Soncini, *Biotechnol. Bioeng.*, 2015, n/a–n/a.
- 112 A. A. Lee, T. Delhaas, A. D. McCulloch and F. J. Villarreal, *J. Mol. Cell. Cardiol.*, 1999, **31**, 1833–1843.
- 113 C. K. Sen and S. Roy, *J. Invest. Dermatol.*, 2010, **130**, 2701–3.
- 114 S. Roy, S. Khanna, A. A. Bickerstaff, S. V Subramanian, M. Atalay, M. Bierl, S. Pendyala, D. Levy, N. Sharma, M. Venojarvi, A. Strauch, C. G. Orosz and C. K. Sen, *Circ. Res.*, 2003, **92**, 264–271.
- 115 C. B. Allen, B. K. Schneider and C. W. White, *Am. J. Physiol. Lung Cell. Mol. Physiol.*, 2001, **281**, L1021–L1027.

- 116 S. Martewicz, F. Michielin, E. Serena, a Zambon, M. Mongillo and N. Elvassore, *Integr. Biol. (Camb)*., 2012, **4**, 153–64.
- 117 C. K. Sen, S. Khanna and S. Roy, *Cardiovasc. Res.*, 2006, **71**, 280–288.
- 118 R. Vivar, C. Humeres, P. Ayala, I. Olmedo, M. Catalán, L. García, S. Lavandero and G. Díaz-Araya, *Biochim. Biophys. Acta - Mol. Basis Dis.*, 2013, **1832**, 754–762.
- 119 R. J. Diaz and G. J. Wilson, *Cardiovasc. Res.*, 2006, **70**, 286–296.
- 120 E. K. Iliodromitis, A. Lazou and D. T. Kremastinos, *Vasc. Health Risk Manag.*, 2007, **3**, 629–637.
- 121 S. T. Hsiao, R. J. Dilley, G. J. Dusting and S. Y. Lim, *Pharmacol. Ther.*, 2014, **142**, 141–53.
- 122 A. Grosberg, P. W. Alford, M. L. McCain and K. K. Parker, *Lab Chip*, 2011, **11**, 4165.
- 123 M. D. Brennan, M. L. Rexius-Hall, L. J. Elgass and D. T. Eddington, *Lab Chip*, 2014, **14**, 4305–18.
- 124 L. Van Duyn Graham, M. T. Sweetwyne, M. a. Pallero and J. E. Murphy-Ullrich, *J. Biol. Chem.*, 2010, **285**, 7067–7078.
- 125 G. Khanal, K. Chung, X. Solis-Wever, B. Johnson and D. Pappas, *Analyst*, 2011, **136**, 3519–3526.
- 126 N. Weiss, F. Miller, S. Cazaubon and P.-O. Couraud, *Biochim. Biophys. Acta*, 2009, **1788**, 842–57.
- 127 H. Wolburg and A. Lippoldt, *Vascul. Pharmacol.*, 2002, **38**, 323–337.
- 128 R. C. Janzer and M. C. Raff, *Nature*, 1987, **325**, 253–257.
- 129 W. M. Pardridge, *NeuroRx*, 2005, **2**, 3–14.
- 130 W. M. Pardridge, *J. Cereb. Blood Flow Metab.*, 2012, **32**, 1959–1972.
- 131 A. K. Ghose, V. N. Viswanadhan and J. J. Wendoloski, *J. Comb. Chem.*, 1999, **1**, 55–68.
- 132 J. H. Yeon, D. Na, K. Choi, S. W. Ryu, C. Choi and J. K. Park, *Biomed. Microdevices*, 2012, **14**, 1141–1148.

- 133 B. Prabhakarpanthian, M.-C. Shen, J. B. Nichols, I. R. Mills, M. Sidoryk-Wegrzynowicz, M. Aschner and K. Pant, *Lab Chip*, 2013, **13**, 1093–101.
- 134 S. P. Deosarkar, B. Prabhakarpanthian, B. Wang, J. B. Sheffield, B. Krynska and M. F. Kiani, *PLoS One*, 2015, **10**, e0142725.
- 135 H. Cho, J. H. Seo, K. H. K. Wong, Y. Terasaki, J. Park, K. Bong, K. Arai, E. H. Lo and D. Irimia, *Sci. Rep.*, 2015, **5**, 15222.
- 136 D. J. Alcendor, F. E. Block III, D. E. Cliffler, J. S. Daniels, K. L. Ellacott, C. R. Goodwin, L. H. Hofmeister, D. Li, D. A. Markov, J. C. May, L. J. McCawley, B. McLaughlin, J. A. McLean, K. D. Niswender, V. Pensabene, K. T. Seale, S. D. Sherrod, H.-J. Sung, D. L. Tabb, D. J. Webb and J. P. Wikswo, *Stem Cell Res. Ther.*, 2013, **4**, 1–5.
- 137 R. Booth and H. Kim, *Lab Chip*, 2012, **12**, 1784–1792.
- 138 L. M. Griep, F. Wolbers, B. De Wagenaar, P. M. Ter Braak, B. B. Weksler, I. a. Romero, P. O. Couraud, I. Vermes, a. D. Van Der Meer and a. Van Den Berg, *Biomed. Microdevices*, 2013, **15**, 145–150.
- 139 B. H. Chueh, D. Huh, C. R. Kyrtos, T. Houssin, N. Futai and S. Takayama, *Anal. Chem.*, 2007, **79**, 3504–3508.
- 140 M. Odijk, A. D. van der Meer, D. Levner, H. J. Kim, M. W. van der Helm, L. I. Segerink, J.-P. Frimat, G. A. Hamilton, D. E. Ingber and A. van den Berg, *Lab Chip*, 2015, **15**, 745–52.